Manipulating the motion of neutral polar molecules with microwave fields

Dissertation

eingereicht von Simon Merz

am Fachbereich Physik der Freien Universität Berlin

Die Experimente wurden aufgebaut und durchgeführt am

Fritz-Haber-Institut der Max-Planck-Gesellschaft, Berlin

und am

Max-Planck-Institut für Struktur und Dynamik der Materie
am Center for Free-Electron Laser Science, Hamburg

mpsd

CFEL
SCIENCE

Hamburg & Berlin, März 2015

Erstgutachter:	Prof. Dr. Gerard J.M. Meijer Radboud University Nijmegen Fritz-Haber-Institut der Max-Planck-Gesellschaft Freie Universität Berlin
Zweitgutachterin:	Priv.-Doz. Dr. Melanie Schnell Max-Planck-Institut für Struktur und Dynamik der Materie Leibniz Universität Hannover
Disputation:	7. Mai 2015

Simon Merz

Manipulating the motion of neutral polar molecules with microwave fields

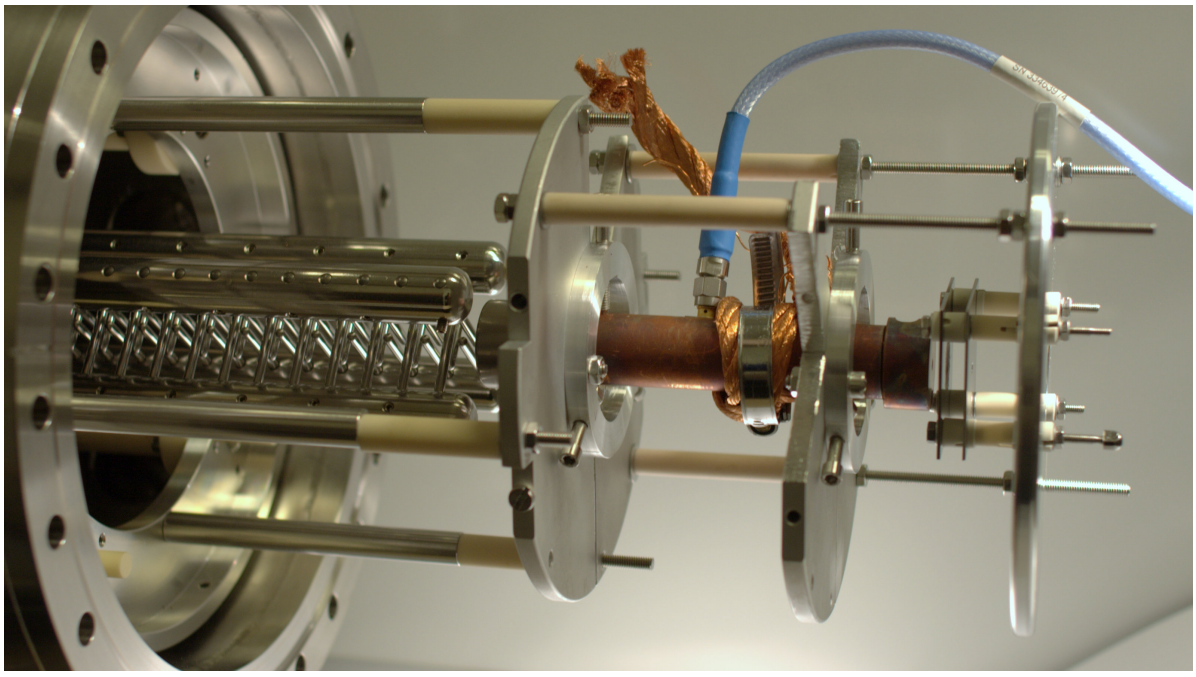

The front page shows a photograph of the closed microwave decelerator in between the Stark decelerator and the time-of-flight mass spectrometer. The braided copper wires are for cooling purposes and the blue coaxial cable is the microwave feed. Further details can be found in Chapter 4.

Zusammenfassung

Kalte Moleküle eignen sich hervorragend für einen weiten Bereich an neuartigen Experimenten, wie zum Beispiel Stoßexperimente mit sehr niedrigen Stoßenergien und hochauflösender Spektroskopie. Eine Herausforderung in diesem Zusammenhang ist die Entwicklung einer allgemein anwendbaren Methode zur Manipulation der Bewegung neutraler, polarer Moleküle in hochfeldsuchenden Zuständen. Dies schließt insbesondere molekulare Grundzustände mit ein, aber auch Zustände in großen, mehratomigen Molekülen.
Für die Manipulation von Molekülen in hochfeldsuchenden Zuständen sind stabile dreidimensionale Feldmaxima notwendig — eine intrinsische Eigenschaft elektromagnetischer Wellen. Die Experimente, die in der vorliegenden Dissertation beschrieben sind, untersuchen die Wechselwirkung zwischen polaren Molekülen mit Mikrowellenfeldern nahe einer molekularen Resonanz in offenen Fabry-Pérot-Resonatoren und geschlossenen, zylindersymmetrischen Hohlraumresonatoren.
Als Testmolekül wurde Ammoniak ($^{14}NH_3$) ausgewählt, das mithilfe der Starkabbremsung quantenzustandsselektiv in einzelnen, wohldefinierten Paketen mit abstimmbarer Geschwindigkeit generiert werden kann. Insbesondere der Grundzustand des para-Ammoniak zeigt eine intensive Wechselwirkung mit Mikrowellenstrahlung im Bereich von 23,7 GHz, entsprechend einer Wellenlänge von 12,7 mm.
Zunächst wurde eine Mikrowellenlinse in Form eines geschlossenen zylindersymmetrischen Hohlraumresonators entwickelt, mit der Ammoniakmolekülpakete mit mittleren Geschwindigkeiten von 20 m/s bis 50 m/s transversal fokussiert werden konnten. Dafür wurde eine Resonatormode verwendet, die ein elektrisches Feldmaximum auf der Resonatorachse aufweist, die mit der Molekularstrahlachse überlagert ist. Um zusätzlich auch die longitudinale Bewegungsrichtung der Moleküle zu beeinflussen, muss zum einen eine Resonatormode verwendet werden, die mehrere elektrische Feldmaxima in Molekularstrahlrichtung aufweist. Zum anderen muss das Mikrowellenfeld präzise und schnell geschaltet werden können. Das erste derartige Experiment mit vollständiger Kontrolle über den longitudinalen Phasenraum wurde in einem modifizierten geschlossenen Hohlraumresonator mit zwölf elektrischen Feldmaxima auf der Resonatorachse und Molekülpaketen mit mittleren Geschwindigkeiten von 12 bis 25 m/s durchgeführt. Mit dem gleichen Aufbau konnten auch erste Mikrowellenabbrems- und -beschleunigungsexperimente erfolgreich durchgeführt werden, bei denen den Molekülen bis zu 30% der anfänglichen kinetischen Energie entzogen bzw. bis zu 60% hinzugefügt werden konnte.
Der besondere Vorteil der Mikrowellenmanipulationsmethode ist ihre Anwendbarkeit auf große mehratomige Moleküle. Da große und schwere Moleküle eine deutlich höhere kinetische Energie besitzen, als beispielsweise das leichte Ammoniak, wird abschließend beschrieben, wie die Mikrowellenabbremser, die im Rahmen dieser Arbeit entwickelt und charakterisiert wurden, verbessert werden können, um die Bewegung großer, mehratomiger Moleküle effektiv zu manipulieren.

Summary

Cold molecules are unique samples that can be exploited for a broad set of novel experiments, such as cold collision studies and precision spectroscopy. An important remaining challenge in this field is a widely applicable method to manipulate the motion of neutral polar molecules in high-field-seeking states, i.e., the molecular ground state and states of more complex medium-sized and large molecules.

For molecules in these states, true three-dimensional field maxima in free space are required, which are an inherent property of electromagnetic waves. The experiments presented in this thesis exploit the interaction of polar molecules with near-resonant microwave fields in open Fabry–Pérot type resonators and in closed cylindrically symmetric resonators.

Ammonia ($^{14}NH_3$) was chosen as a prototypical test molecule for these microwave manipulation experiments because well-controlled ammonia packets can be generated using Stark deceleration in single quantum states. These packets are ideal starting points for developing and characterizing novel motion manipulation techniques. In particular, the rovibronic ground state of para-ammonia has a strong interaction with microwave radiation close to 23.7 GHz corresponding to a wavelength of 12.7 mm. In a first set of experiments, transverse focusing of packets of ammonia molecules with mean forward velocities ranging from 20 m/s to 50 m/s was demonstrated in a closed cylindrically symmetric resonator. The resonator mode used for these experiments features an electric field maximum on the resonator axis that coincides with the molecular beam axis. In order to also manipulate the forward motion of the molecular packets, several consecutive electric field maxima on the molecular beam axis are required and the microwave field has to be rapidly switched at the appropriate times. In a modified closed cylindrically symmetric resonator with twelve consecutive electric field maxima on the axis, the first microwave guiding with full phase-space control was demonstrated for packets of ammonia molecules with a mean forward velocity ranging from 12 m/s to 25 m/s. With the same setup, also the first microwave acceleration and deceleration were accomplished with an extraction of as much as 30% of the initial kinetic energy and a gain by up to 60%.

The main advantage of the microwave manipulation technique is its applicability to larger molecules that cannot be manipulated with conventional methods, such as Stark-deceleration. Successful deceleration is complicated for a number of reasons. For example, these larger molecules generally carry much higher kinetic energy. Furthermore, a precise theoretical calculation of the interaction with microwave fields becomes much more challenging. In the last part of this thesis, methods are proposed to increase the performance of the microwave decelerator, developed and characterized in this thesis, to eventually provide slow samples of medium-sized molecules, such as aminobenzonitrile, and trap ammonia.

Contents

1 Cold molecules

The research of cold or even ultra-cold gases is a recent and fruitful field in atomic and molecular physics that enables high-precision measurement and manipulation of individual quantum systems [1–7]. A famous achievement obtained in this research field is quantum degeneracy in a cold and dense sample. At very low temperatures, bosons undergo a phase transition into a collective ground state, whose wave function extends over the full ensemble. This makes it possible to observe quantum phenomena on a macroscopic scale. A similar degree of control is desirable for molecules; however, molecules have a more complex energy level structure due to the motions of the composing atoms: the rotations and the vibrations. These make it much more difficult to exert similar degrees of control on molecular samples than on atoms. On the other hand, the additional complexity offers new prospects, for example, for precision tests of fundamental theories. Rovibrational spectra show a large sensitivity to nuclear effects and are thus promising probes for parity violation effects [8, 9]. In addition polar molecules exhibit long-range dipole-dipole interactions that can be precisely tuned with external fields. This is attractive for quantum information experiments because it enables reliable upscaling of quantum logic gates [10].

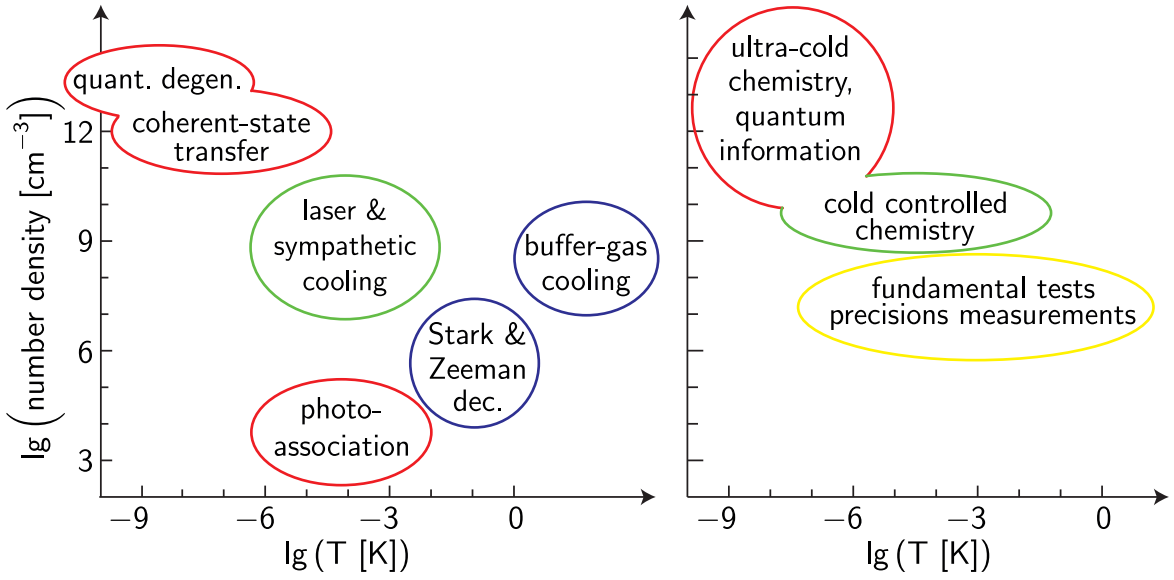

Figure 1.1: Overview of the temperatures and number densities that can be achieved with different cooling techniques on the left side and the anticipated conditions required for studying certain phenomena using atomic and molecular samples on the right side.

An overview over a selection of techniques to manipulate and control molecules is given in Figure 1.1. The temperatures and particle number densities that can be achieved with

the respective method are given on the left side. The right side shows the conditions required to observe certain phenomena in and with molecules.

In order to study the properties of atoms and molecules, the simplest conceivable experiment is the investigation in the gas phase. Gas-phase experiments establish an environment in which the sample is uninfluenced by interactions with a solvent or an adhesive. It is again most straightforward to realize such an experiment at room temperature. However, under normal conditions (k_BT at room temperature is $4 \cdot 10^{-21}\,\mathrm{J} \approx h \times 6\,\mathrm{THz}$), the relative velocities of the sample particles are very high and in the case of molecules, typically many rotational and vibrational levels are populated. The typical spacing of rotational levels is 10^9–$10^{11}\,\mathrm{Hz}$ and spacing of the vibrational levels is 10^{13}–$10^{14}\,\mathrm{Hz}$ compared to the larger spacing of electronic levels typically on the order of 10^{14}–$10^{15}\,\mathrm{Hz}$.

An environment in which collisions are prevented is ideal to study isolated atoms or molecules. These conditions are met by atomic and molecular beams. Beams are directed particle streams, diluted such that no collisions occur on the time scale of an experiment. These beams are typically fast, i.e., they have a large forward velocity, but with comparably small relative velocities. In addition, these techniques are advantageous to cool molecular samples to low temperatures so that only few states of the internal degrees of freedom are populated.

1.1 Temperature

Temperature relates to the energy distribution in a particle sample. The energy E is connected to the temperature T via $E \propto e^{-k_BT}$ with the Boltzmann constant $k_B = 1.38 \cdot 10^{-23}\,\mathrm{JK}^{-1}$. In the context of atomic and molecular samples, the term *cold* is commonly used for temperatures below 1 K and *ultra-cold* refers to the temperature regime below 1 mK.

A molecule that is composed of N atoms has $3N$ degrees of freedom, that are distributed over translation, vibration and rotation according to Table 1.1.

Table 1.1: Number of degrees of freedom of an N-atomic molecule.

degree of freedom	linear	non-linear
translational	3	3
rotational	2	3
vibrational	$3N-5$	$3N-6$

In thermal equilibrium, the average energy in a particle sample is equally distributed over all degrees of freedom. Then the temperature is related to the particle speeds by the three-dimensional Maxwell–Boltzmann distribution. The speed is the absolute value of the molecule's velocity, $v = \sqrt{v_x^2 + v_y^2 + v_z^2}$, and the probability of finding a molecule with the speed v reads as

$$p(v) = 4\pi v^2 \left(\frac{m}{2\pi k_B T}\right)^{3/2} e^{-mv^2/(2k_BT)}. \tag{1.1}$$

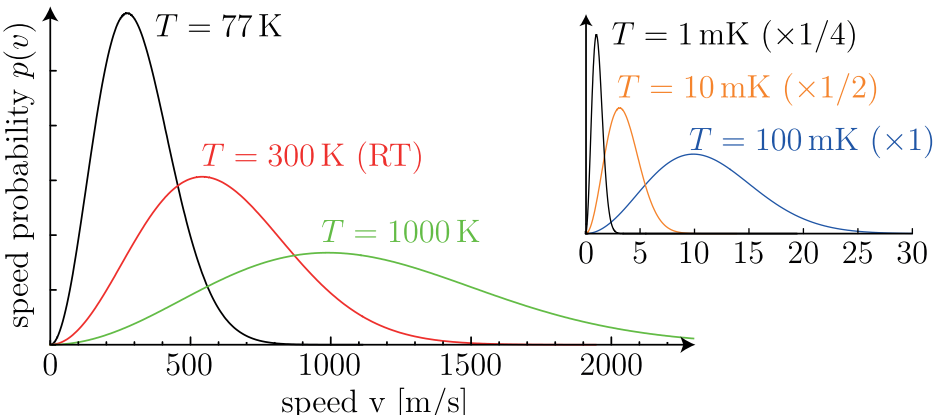

Figure 1.2: Speed distributions for atoms and molecules with a mass of 17 u at temperatures ranging from 1000 K to 1 mK (in the right inset) according to Equation 1.1. The traces for 1 mK and 10 mK are scaled by 1/4 and 1/2, respectively.

The speed distribution of molecules with mass 17 u such as ammonia ($^{14}NH_3$) or the hydroxyl radical (OH) according to Equation 1.1 is depicted in Figure 1.2. The distribution becomes narrower and its maximum shifts towards lower velocities with decreasing temperature. At room temperature, for example, the speed distribution of a sample of ammonia molecules has a maximum close to 540 m/s with a full width at half maximum (FWHM) of 625 m/s. At 1 mK, both values are reduced to approximately 1 m/s. Hence, cold molecules are slow molecules, with small relative velocity components.

Similarly, the energy in a particle sample is distributed over the internal degrees of freedom. This is illustrated in Figure 1.3 where the populations of the rotational states of benzonitrile are shown at temperatures ranging from approximately room temperature down to 1.5 K. With decreasing temperature, the population shifts to states with lower energies, fewer states are populated and consequently the population of these states increases significantly.

Strictly speaking, a temperature only applies to particle samples (atoms or molecules) that are in thermal equilibrium, which is not necessarily the case in cold and ultra-cold gas-phase samples. Nonetheless, the term *temperature* is used as a measure of the energy in particular degrees of freedom such as the translation ($E_{\mathrm{trans.}} \sim k_B T$).

Precise control of molecules on the quantum level requires samples in well-defined quantum states and with well-defined translational properties. It has thus proven useful to cool the molecules. In this respect, two different production pathways can be distinguished: *direct* methods that start with molecules in a gas-phase sample that are then cooled down and the *indirect* techniques that start with samples of cold and ultra-cold atoms that are subsequently assembled into simple molecules.

Cold and ultra-cold atomic samples can be generated in high densities using laser cooling, which is summarized in the following.

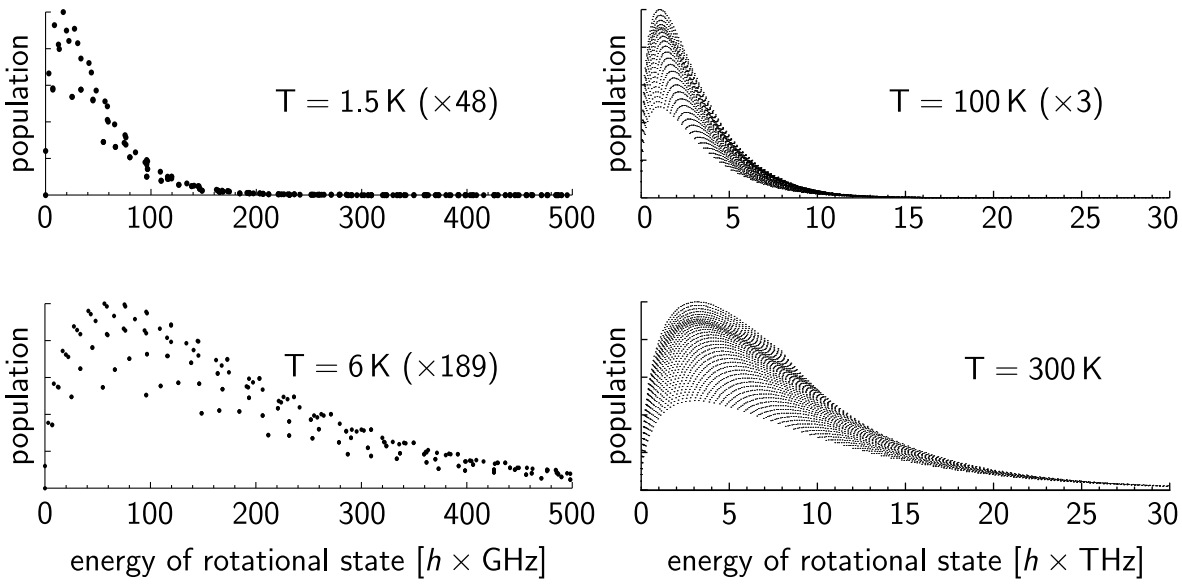

Figure 1.3: Population of the rotational states of benzonitrile depending on the temperature ranging from 300 K (≈ RT) down to 1.5 K. The rotational state is given by its energy as determined by PGOPHER [11]. For 1.5 K and 6 K, rotational states with energies up to $h \times 500\,\mathrm{GHz}$ are shown. For 100 K and 300 K states with energies up to $h \times 30\,\mathrm{THz}$ had to be included. The different plots are scaled for clarity.

1.2 Laser cooling

Laser cooling harnesses the recoil due to scattered photons [12]. This is possible because a photon carries a small momentum $p = E_P/c$ with the speed of light c and the photon energy $E_P = \hbar\omega_P$. Scattering requires absorption, which is most probable if the photon energy matches a resonance in the atom or molecule, and subsequent spontaneous emission of a photon. If the absorbed photons come from the same direction, momentum can be transferred, whereas the spontaneous emission alway occurs in a random direction and thus does not transfer momentum. Many photons ($\sim 10^4$) have to be absorbed to slow an atom or molecule with an initial velocity of several hundred m/s down to standstill. A large scattering rate requires a short lifetime of the excited state as well as a decay that leads back to the initial state with a probability near unity. This last feature is summarized by the term *closed transition cycle* and cannot be found in every atom. In particular alkali and earth-alkali atoms are good candidates for laser cooling. It has been proven difficult to apply the powerful method of laser cooling to molecules because of their much richer internal structure. The vibrational levels lead to many different decay channels of an electronically excited state. This generally prevents the required closed transition cycles. Exceptions to this rule are the diatomic molecules SrF [13], CaF [14] and YO [15] for which still many loss channels occur, however strict selection rules and favorable Franck–Condon factors allow efficient re-pumping into the main cooling transition cycle with a reasonable number of additional lasers.

One of the important obstacles in the beginning of laser cooling was the compensation of the Doppler shift. In the reference frame of the atoms, the frequency of the laser light

changes as they are slowed down. One option of compensating for the Doppler shift is by applying an external magnetic field that shifts the energy levels depending on their position in the deceleration process. This device became famous as the optical Zeeman slower developed by William D. Philips and coworkers [16]. The lower limit for laser cooling is on the order of the recoil energy of a photon, $\sim \mu$K. In 1997, Steven Chu, Claude Cohen-Tannoudji and William D. Philips received the Nobel Prize in physics for the development of laser cooling that was first experimentally demonstrated on trapped magnesium ions in 1978 [17].

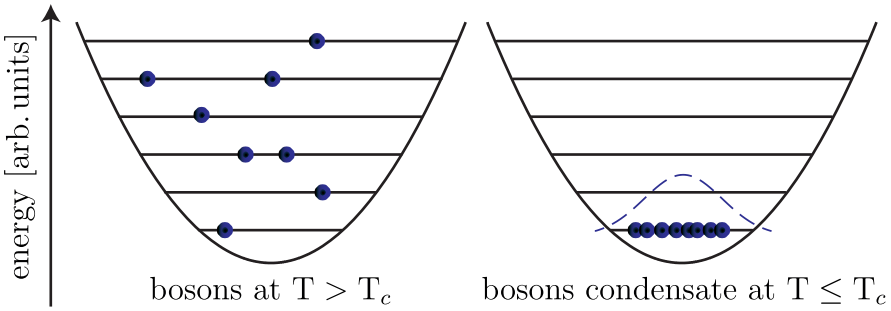

Figure 1.4: Schematic of quantum degeneracy in a sample of trapped bosons. The left side shows how the bosons populate many different states at high temperatures. As the sample is cooled down below the critical temperature T_c, they condense into the trap ground state. The state of this Bose–Einstein condensate (BEC) is described by a single collective wave function.

Laser cooling was an ideal starting point for achieving quantum degeneracy in an atomic sample. That means, the wavelength associated with the atom, the so-called thermal de Broglie wavelength $\Lambda = h/\sqrt{2\pi m k_B T}$, becomes much larger than the interatomic distance. At the critical temperature T_c, which is typically in the nanokelvin regime, atoms experience an overlap of the wave functions, and bosonic atoms (integer total quantum number) experience a phase transition into a collective state, the so-called Bose–Einstein condensate that was predicted already in 1924 by Satyendranath Bose and Albert Einstein [18] and first experimentally demonstrated with rubidium atoms by Eric Cornell and Carl Wieman in 1995 [19] and independently by the group of Wolfgang Ketterle. The latter three received the Nobel Prize in physics for this discovery [20, 21]. A similar situation occurs when bosons in a trapping potential are cooled down. Below the critical temperature, the bosons condensate into the trap ground state where they again become part of a single collective wave function, as depicted in Figure 1.4.

The indirect methods that allow the assembly of simple molecules from laser-cooled atoms are presented in the next section.

1.3 Assembly of molecules from atoms

Atoms can be controlled and confined exceptionally well, for example with external fields, and by using so-called Feshbach resonances [22] between the bare atom states and the bound molecular state AB, the formation of molecules can be triggered. This

process has to conserve energy and momentum which prevents the molecule formation from a simple two-body collision. Typically, a third collision partner, another atom or a photon for example, is required to form a molecule.

If this reaction is mediated by an additional photon $A+B+h\nu \rightarrow (AB)^* \rightarrow (AB)+h\nu'$ it is called photo-association [23–25]. It is also possible to utilize an external magnetic field to *magneto-associate* the atoms [26–28]. This can be achieved using a constant magnetic field, which brings the Zeeman levels of the unbound atoms and the bound molecule very close together, thereby strongly increasing the three-body recombination rate. Alternatively, the external magnetic field can be swept adiabatically over the Feshbach resonance, directly converting the two atoms into a molecule. In any case, the new molecule has a translational temperature comparable to the parent atoms; however, it is usually in a highly vibrationally excited state. By spontaneous emission it can decay into the ground state. This process is, however, fairly inefficient. The yield of ground-state molecules can be enhanced to almost unity by employing elaborate population transfer methods such as STIRAP (stimulated Raman adiabatic passage) [7, 29–32].

So far, ultra-cold ground state molecules of KRb, SrF, LiCs and RbCs have been produced by indirect cooling techniques. Since these methods rely on laser cooling of atoms, which is mostly limited to alkali and earth alkali related species. Only dimers and sometimes trimers can be made, which offer an interesting playground for novel molecular physics experiments such as molecular Bose–Einstein condensates that were first realized with alkali dimers [33–35]. Polar molecules exhibit stronger long-range interactions, if compared to atoms, which promises new phenomena in quantum many body systems [36]. The limitation to alkali dimers and trimers, however, excludes almost all typical molecular matter that has an impact on chemistry and biology. For these molecules direct cooling methods have to be applied.

1.4 Direct cooling of molecules

For more complex molecules and molecules made of atoms that are not exclusively in the first two groups of the periodic table, direct cooling techniques have to be applied. The two major contestants are supersonic expansion from a high pressure container through an aperture into a vacuum chamber and buffer-gas cooling in a cryogenic cell. The following two subsections are dedicated to these techniques. With supersonic expansion, internally cold but fast molecules are generated which makes it a good starting point for further beam manipulation techniques, such as deceleration.

1.4.1 Supersonic expansion

A versatile method to produce internally cold molecular beams is the supersonic expansion. It relies on a pressure difference between a container ($\sim 1\,\mathrm{bar}$), filled with the substance to be cooled, and a vacuum region ($p \ll 10^{-5}\,\mathrm{mbar}$). The gas is adiabatically expanded into the vacuum through a controlled leak (valve) as depicted in Figure 1.5.

If the orifice diameter is small with respect to the mean free path of the particles in the high-pressure container, occasionally a particle escapes. Consequently, the beam has a similar velocity distribution as the thermalized gas in the container. There, the

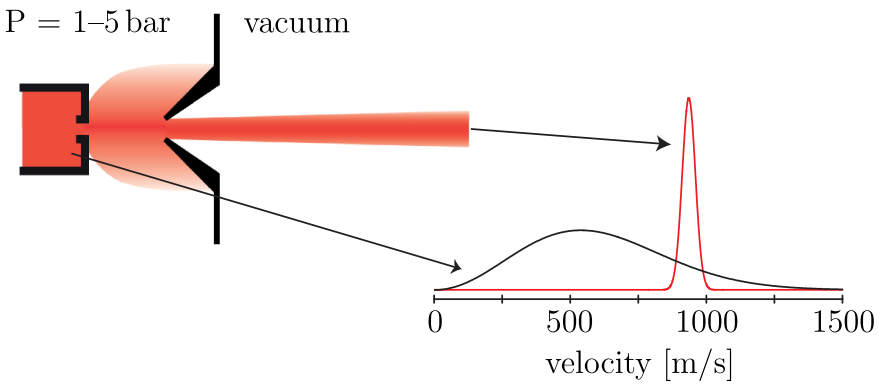

Figure 1.5: Schematic of the production of a skimmed supersonic molecular beam. The molecules from a high-pressure container (left) are expanded into a region with much lower pressure (vacuum chamber). The plots show the velocity distributions of pure ammonia samples (mass 17 u) following a Maxwell–Boltzmann distribution in the cell (black trace) and the narrow, shifted Gaussian distribution in the supersonic beam (red trace).

probability $p(v)$ of finding a particle with the velocity $v = |\vec{v}|$ is described by the Maxwell–Boltzmann distribution, Equation 1.1, and the beam is said to be *effusive*.

A different situation occurs if the leak diameter is much larger than the mean free path of the particles in the container. Then the molecules collide with one another while moving through the nozzle. The large number of collisions results in an energy exchange between the particles. The internal degrees of freedom of the molecules are cooled by energy conversion into the forward kinetic energy of the beam. The forward velocity distribution (z-direction) of this beam is best described by a Gaussian distribution (1D Maxwell–Boltzmann distribution) shifted by the mean forward velocity of the beam, $\bar{v}_0$:

$$p(v_z) = \left(\frac{m}{2\pi k_B T}\right)^{3/2} e^{-\frac{m(v_z-\bar{v}_0)^2}{2k_B T}}. \tag{1.2}$$

Packets of molecules produced via supersonic expansion are thus cold in the sense that the relative velocities of the molecules are very small, i.e. their velocity distribution is narrow, whereas the collective forward velocity of the particles within the laboratory frame is very high. A decelerator for molecules can be used to decelerate such a packet of molecules producing a translationally cold molecule sample. The term supersonic expansion was coined because the particle speed in such a beam can easily exceed the speed of sound in the gas [37].

A limiting factor of cooling by supersonic expansion is the limited number of collisions that provides a minimum achievable temperature of typically a Kelvin. At this temperature regime cluster formation of the particles involved can be significant. The released binding energy after the expansion heats up the particles. To reduce the effect of cluster formation, rare gases are usually used as seed gas, since the binding energies of molecules with rare gas atoms are very small. A seed gas has an additional important implication: the mean forward beam velocity $\bar{v}_0$ of a seeded beam, i.e., consisting of a few % sample molecules in an atomic rare gas, is governed by the mass of the seed atoms (simply

because of energy conservation and $E_{\mathrm{kin}} = mv^2/2$). The heavier the seed atoms are, the lower the final beam velocity but the larger the polarizability and thus the tendency for cluster formation. In the case of a supersonic expansion of heavy xenon atoms (131.29 u) from a room temperature reservoir, the mean forward beam velocity is $\bar{v}_0 \approx 320\,\mathrm{m/s}$. For the light helium (4.00 u), on the other hand, it amounts to $\bar{v}_0 \approx 1800\,\mathrm{m/s}$.

Supersonic expansion allows for the generation of cold beams of a variety of molecules. The only requirement is that the molecule can be brought into the gas phase. Gaseous species under normal conditions can be mixed with the seed gas in the high-pressure container. Volatile species that are liquid or even solid at normal conditions can be brought into the gas phase by heating. For more complex molecules that are not volatile at room temperature and disintegrate upon heating before reaching a significant vapor pressure, more sophisticated methods are required. Possible options include the use of short laser pulses (typically ns to ps) to ablate or desorb a solid sample directly into the collision zone right behind the nozzle.

Another approach to reduce the large mean velocity of a supersonic jet by mechanical means was developed in 1999. In this experiment, the valve was mounted on a counter-rotating rotor [38, 39]. Technology allows for rotation speeds of several hundred Hz. Typically, a rotation speed of about 250 Hz is used which corresponds to a speed on the order of 300 m/s on a 20 cm long rotor tip. In 2013, such a counter-rotating nozzle was used in a microwave focusing experiment to obtain slow acetonitrile molecules from a supersonic expansion [40]. These counter-rotating nozzles are, however, difficult to maintain.

1.4.2 Buffer-gas cooling

An alternative method to produce beams of cold molecules with low forward velocities is buffer-gas cooling pioneered by the groups of Frank De Lucia and John Doyle [41, 42], see also Section 6.2. Here, the sample molecules thermalize in a cryogenic cell filled with a noble gas, such as Ne, ^{4}He or ^{3}He at typical number densities of $n = 10^{14}$–$10^{17}\,\mathrm{cm}^{-3}$. The noble-gas density is precisely tuned to ensure enough collisions to thermalize the molecules on the typical length scale of the cryogenic cell ($\sim$ cm) while preventing cluster formation due to three body collisions.

The cryogenic cell can be cooled by liquid helium evaporation or a closed-cycle pulse tube cooler. The final temperature of the sample molecules, however, depends on the evaporation pressure of the buffer gas. When too low, the buffer-gas atoms will stick to the walls of the cryogenic cell and there will not be enough collisions to thermalize the sample molecules. With ^{4}He approximately 1 K can be reached and a few hundred millikelvin are the limit in case the rare and thus expensive ^{3}He is used. The sample molecules are introduced at 300 K up to a few 1000 K with similar methods as described in Section 1.4.1.

This method is a general approach towards cooling since the only requirement is a non-zero elastic scattering cross section which means that many different species can be cooled in a buffer gas cell. So far, the largest molecule that was cooled in a buffer-gas cell is Nile red ($C_{20}H_{18}N_2O_2$) which is comprised of 42 atoms [43].

Combining a buffer-gas cell with the spherical magnetic quadrupole field formed by coils in anti-Helmholtz configuration allowed trapping of para-magnetic species, such as

CaH [44], PbO [45], CrH, MnH [46] molecules and NH radicals [47].

With an aperture in the cell wall towards a high-vacuum region, a beam of the buffer gas with the sample species can be produced [45, 48, 49]. This method started with producing beams of heavy diatomic molecules but also beams of larger polyatomic species can be generated, such as benzonitrile (Sec. 6.2) in a 5 K cell. Buffer-gas cells are typically operated in between the effusive and the supersonic regime with some hydrodynamic enhancement. In contrast to supersonic jets, that employ backing pressures of several bar and consequently require very large vacuum pumps or a pulsed operation mode to ensure a sufficiently good vacuum for the beam formation, buffer-gas cells are typically operated in continuous mode. The forward velocity of the molecules can be reduced even further by using a second cell with much lower buffer-gas density. There, a few additional collisions slow down the molecules at the cost of an overall flux reduction [50].

Beams from buffer-gas sources usually feature higher intensities (by up to three orders of magnitude) of the sample molecules and a lower beam velocity than supersonic jets. On the other hand, the temperatures of the molecular beams are typically higher ($\sim$ 3–8 K) than in a supersonically expanded beam ($\sim$ 1 K), see also Figure 1.1.

1.5 Beam manipulation

Over the past century numerous methods have been developed to control and manipulate molecular beams. Excellent reviews that present the historical development and the details of the various methods that are employed can be found in References [5, 51, 52]. It all started with a proposal by Kallmann and Reiche in 1921 to study molecular dipole moments [53], followed in 1922 by Stern and Gerlach who demonstrated space quantization by deflection of silver atoms using an inhomogeneous magnetic field [54]. This was explained by a quantized magnetic moment of the silver atom [55] that was initially thought to be caused by the orbital angular momentum. A couple of years later, after the discovery of an intrinsic angular momentum of the electron, the spin, that can only take the two discrete values $\pm\hbar/2$, it became clear that the quantization is actually caused by the spin of the 5s electron, since the total orbital angular momentum of the silver atom in its ground state is zero.

1.5.1 with magnetic fields

The interaction of atoms and molecules with magnetic fields has proven to be fruitful for many different kinds of experiments such as spectroscopy on nuclear spin states using the nuclear magnetic resonance technique. Modern health care strongly relies on the magnetic-resonance-imaging technology to get detailed multi-dimensional information about the soft tissue in the human body.

The influence of an external magnetic field on atoms and molecules is named after the Dutch physicist Pieter Zeeman who received the Nobel Prize in physics together with Hendrik A. Lorentz in 1902 for the discovery [56] and the description of the Zeeman effect. In the Hamiltonian, the interaction of a magnetic field $\vec{B}$ with the magnetic

moment $\vec{\mu}_{\text{magn.}}$ of an atom or a molecule takes the very general form $H = H_0 + H_Z$, with the Hamiltonian of the unperturbed particle H_0 and the interaction $H_Z = -\vec{\mu}_{\text{magn.}} \cdot \vec{B}$.

In atomic and molecular physics, strong magnetic fields can be used as a tool to manipulate the motion of paramagnetic atoms and molecules, not only transversely but also longitudinally. The so-called Zeeman decelerator employs strong magnetic fields on the order of a few Tesla and large magnetic field gradients on the molecular beam axis. Paramagnetic species have magnetic dipole moments on the order of $1\mu_B = 9.27 \cdot 10^{-24}\text{JT}^{-1}$, the Bohr magneton. Consequently the Zeeman shift is on the order of $h \times 10\,\text{GHz}$. The first experimental realization of a multi-stage Zeeman decelerator was accomplished by Nicolas Vanhaecke *et al.* in 2007 using six sequential solenoids. By switching the solenoids on and off, kinetic energy was extracted from ground state hydrogen atoms [57, 58]. Since then, Zeeman deceleration was applied to various other species, such as deuterium atoms [59], O_2 molecules [60, 61] and methyl radicals [62].

The experimental challenges for Zeeman decelerators include the control of large currents of hundreds of Amperes in very short time scales of preferentially sub-μs.

1.5.2 with electric fields

The remainder of the discussion will focus on applying electric fields $\vec{E}$ to manipulate the motion of neutral polar molecules. Many molecules have a permanent electric dipole moment $\vec{\mu}_{\text{perm}}$, as the result of a charge separation between the positively charged nuclei and the negatively charged electrons. Exceptions to this rule are homonuclear linear molecules, for example N_2, as well as highly symmetric species like benzene. A permanent dipole moment is an ideal starting point for a strong interaction with external electric fields. This interaction is known as the Stark effect and is described in more detail in Section 3.3.

An important consequence of the interaction of an electric dipole with an inhomogeneous electric field can be understood using the classical picture, as depicted in Figure 1.6. If a dipole is placed into the electric field of a capacitor with non-parallel plates, the dipole will experience a torque that leads to an alignment of the dipole moment with electric field lines. Hence, two equilibrium configurations are possible, the parallel orientation on the left side and the anti-parallel orientation on the right side of Figure 1.6. Depending on this orientation, the dipole experiences a force towards parts of higher electric fields or towards parts of weaker electric fields, as indicated by the arrows on the dipoles. Rotating polar molecules in an external electric field are not quite identical to the classical picture, however they show similar behavior in an inhomogeneous electric field: Depending on their quantum state, a polar molecule will experience a negative Stark shift with increasing electric field strength which corresponds to the left classical dipole, which is referred to as a high-field-seeking state, or a positive Stark shift, which is similar to the classical dipole on the right side and referred to as a low-field-seeking state, or an almost zero Stark shift.

Deflection & focusing

In 1927, Erwin Wrede performed first experiments on a molecular beam to investigate the properties of the molecule's electric dipole moment by measuring their deflection in

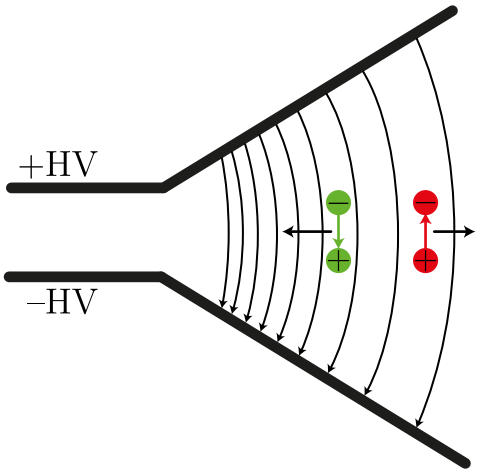

Figure 1.6: Electric dipole in an inhomogeneous electric field: the dipole moment $\vec{\mu} = \sum q_i \vec{r}_i$ points towards the negative charge. Without additional forces, the effective force points towards regions with stronger electric field in the parallel case, indicated on the left, and towards regions with weaker electric fields in case of the anti-parallel oriented dipole on the right side.

an inhomogeneous electric field. It took more than two decades to extend the motion control into two dimensions. In 1954, Charles Townes and coworkers developed a device that employed the electric field in an electrostatic quadrupole to state-selectively focus ammonia molecules into a microwave resonator, as shown in Figure 1.7. This method allowed for very accurate measurements of the inversion splitting in several ammonia inversion doublets [63]. This way, the first population inversion was achieved, since most of the molecules that arrive in the microwave resonator are in the upper, low-field-seeking inversion doublet component (excited state). Resonant microwave radiation will thus be amplified by stimulated emission from the molecule sample [64]. The MASER (Microwave Amplification by Stimulated Emission of Radiation), predecessor of the even more famous LASER (Light Amplification by Stimulated Emission of Radiation), was born. In the same year, Bennewitz and coworkers used a similar electrostatic quadrupole to transversely focus a beam of neutral KBr and KF molecules [65].

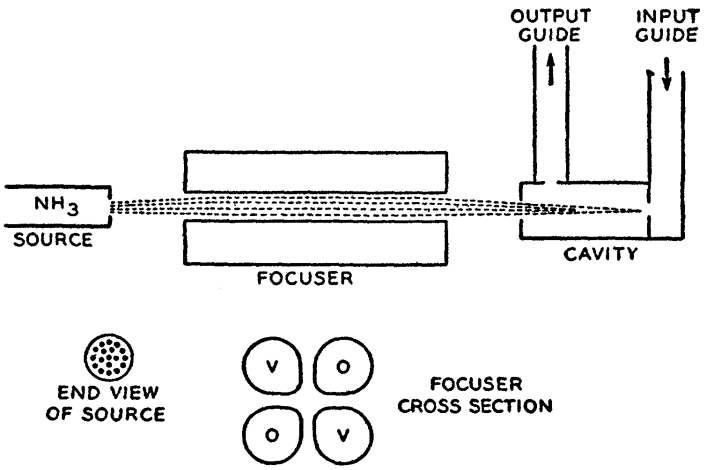

Figure 1.7: Schematic of the molecular beam apparatus used by Townes and coworkers, that later became known as the MASER [63, 64]. The quadrupole focuser selectively focuses ammonia molecules in the low-field-seeking, upper inversion doublet component into the microwave cavity, so that population inversion is achieved.

In 1966, the focusing technique was extended to molecules in high-field-seeking states by the development of the Alternating-Gradient (AG) method by Auerbach *et al.* [66]. The problem with manipulating molecules in high-field-seeking states with static electric fields is that the electric field maxima are always on the electrode surfaces, i.e. no three-dimensional (3D) static electric field maxima exist in free space. This is a consequence of Maxwell's equations and was formulated already in 1842 by Samuel Earnshaw, hence it is also known as Earnshaw's theorem [67]. In an alternating-gradient focuser, one makes use of saddle-point like electric field distributions in the transverse directions. These fields focus molecules in high-field-seeking states in one of the two transverse directions, say x, and defocus them in y. Either by switching between two different saddle-point configurations or by consecutive elements rotated by 90°, an overall focusing effect can be achieved.

To date, AG guiding is used to select specific rotational states of medium-sized and larger polyatomic molecules, for example benzonitrile (C_6H_4CN) [68, 69]. This method can be used, for example, for rotational-state specific spectroscopy [70].

Deceleration & acceleration

Manipulation of motion in three dimensions, e.g. apart from transverse focusing also deceleration and acceleration for molecules in low-field-seeking states, was first proposed in the 1960s as well, however these early projects were deemed unsuccessful and consequently abandoned. It took another 30 years until Stark deceleration, see also Section 4.1, was first demonstrated in the group of Gerard Meijer at the Radboud University Nijmegen [71]. In a first experiment, meta-stable CO molecules could be decelerated from 275 to 200 m/s in an array of 63 sequential 3 mm diameter high-voltage electrode pairs. In a Stark decelerator, a molecule experiences an increasing electric field as it approaches a pair of high-voltage electrodes. Thus, a polar molecule in a low-field-seeking state has to climb a potential hill, due to the DC-Stark effect. The required potential (Stark) energy is extracted from the kinetic energy and the molecule slows down. Energy conservation dictates that this process reverses as the molecule passes the electric field maximum between the high-voltage electrodes and leaves it behind. In this case the net effect on the kinetic energy and hence the velocity would be zero. However, by fast switching the high-voltage electrodes to ground before the molecule passes the electric field maximum, the extraction of kinetic energy is permanent and the molecule has experienced a net deceleration. The Stark decelerator uses many of these electrode pairs, also referred to as stages, so that the process can be repeated many times.

Until today, Stark deceleration has been applied to many, mostly small, molecules in low-field-seeking states: ND_3 [72, 73], NH_3 [74], OH [75–79], metastable NH [80, 81], OD [82], H_2CO [83], SO_2 [84], LiH [85], CaF [86], YbF [87], SrF [88] and NO [89].

The combination of AG-focusing with Stark-deceleration was experimentally demonstrated for CO [90], YbF [91], OH [92] and benzonitrile [93]. AG-deceleration makes use of consecutive two-pole AG-focusing units. The polar molecules can be accelerated and decelerated in the fringe fields of these electrode pairs. By switching the fields on and off at the appropriate time, an imbalance in acceleration and deceleration can be generated. The transverse stability is achieved by rotating the subsequent two-pole units by 90° which switches between two saddle-point like electric field distributions in the transverse

directions.

Stark deceleration as well as AG-deceleration is typically applied to molecular beams generated by supersonic expansions, which have typical translational temperatures on the order of a Kelvin. These decelerators usually have a phase-space acceptance smaller than the phase space of a supersonic expansion. Consequently, such a decelerator cuts out part of the initial phase space of the molecular beam. Many molecular samples can be decelerated to standstill and their typical translational temperatures are then on the order of 10–100 mK and thus ideally suited for trapping.

Trapping

In general, a trap needs to provide a potential Φ with a 3D minimum at the trap center. As the molecule diverges from the trap center a restoring force $-\vec{\nabla}\Phi$ brings it back to the center. First traps for molecules were proposed already in 1980 [94], but without feasible methods to generates slow molecules, trapping is difficult. This changed with the development of buffer-gas cooling (Sec. 1.4.2) and the Stark deceleration technique (Sec. 1.5.2).

A common trap design for polar molecules mimics the electrostatic field of an electric multipole field (quadrupole, hexapole) [94, 95]. These setups allow trap depths on the order of 1 K. The trapping time for molecules in low-field-seeking states in such a trap can be optimized by overlaying it with a constant electric field such that the field minimum in the trap center is non-zero (Ioffe-Pritchard trap [96]). This is beneficial to minimize losses due to non-adiabatic transitions between a low-field-seeking $M \neq 0$ state and an $M = 0$ state that has no first-order Stark effect. The field offset in the trap center allows to increase the energy difference between these different states due to the Stark-shifted low-field-seeking states [97].

Traps allow for long interaction times of the trapped molecules with external probes. Trap losses provide insight into decay processes of the trapped quantum states. Possible loss channels are inelastic collisions, which are state-changing and thus lead to states that are not trapped anymore, but also spontaneous decay into a non-trappable state can occur. When the trapped state has a lifetime shorter than the trapping time, this lifetime can be accurately measured [47, 98]. Last but not least, trapped molecules, similar to experiments with atoms, are an important pre-requisite for further cooling to ultra-cold temperatures.

Many different cooling options have been discussed so far such as sympathetic cooling, i.e., mixing a cloud of trapped molecules with ultra-cold laser-cooled atoms [99]. Then the molecules should thermalize via collisions with the ultra-cold atoms, a promising route towards ultra-cold atoms that so far was applied only to atomic and ionic species [100–102].

A promising method for cooling polyatomic molecules to the μK regime is Sisyphus cooling in an electrostatic micro-structured trap that, so far, has been applied to cool CH_3F molecules from 390 mK to 29 mK [103, 104].

Evaporation cooling is commonly applied to cool optically trapped atoms from the μK regime to the nK regime. The process, however, requires collisions between the particles to exchange energy. This is particularly difficult with molecules in low-field-seeking states, because those are never ground-state molecules. As a result, the transition into

the high-field-seeking ground state (spontaneous or induced by a collision) would remove the molecule from the trap. Consequently, a trap for molecules in high-field seeking states is desired for such experiments.

The combination of an inhomogeneous electric multipole field and a homogeneous electric field can also be adapted to trap molecules in high-field-seeking states. With such a setup, the overall electric field can be shaped into saddle-point like structures. By suitable switching between these configurations, molecules in high-field-seeking states can be trapped similar to the alternating-gradient method in an AG focuser or AG decelerator. The trap depth is, however, substantially lower ($\sim$ 1–10 mK) than in a trap for molecules in low-field-seeking states. This was first demonstrated in 2005 for $^{15}ND_3$ [105] and a cylindrical trap and later also for other electrode geometries [106, 107].

1.5.3 with optical fields

As an alternative to static electric fields, electromagnetic fields can be used. These have the advantage that true 3D electric field maxima can be generated in free space.

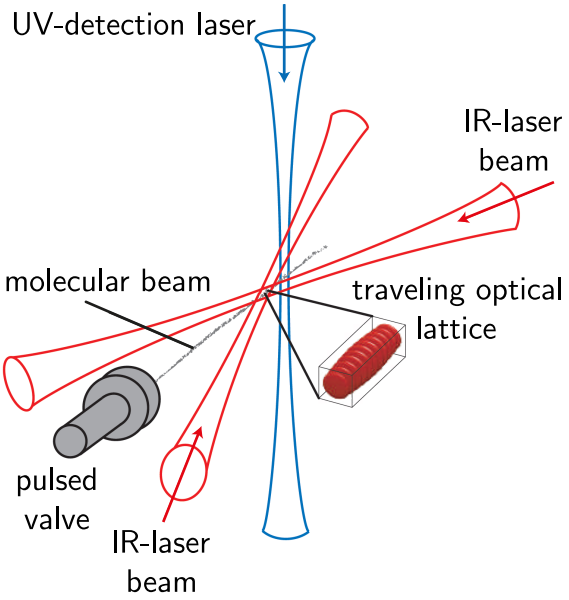

Figure 1.8: Schematic of the optical decelerator that employs a moving lattice generated by two infrared laser beams [108].

Laser beams, if focused down to a few μm, provide extremely high electric-field gradients which are ideal for the motion manipulation of neutral molecules with large polarizability. Then a permanent dipole moment is not required, since the external electric field will induce a dipole moment proportional to the electric field. To a good approximation, one finds

$$\vec{\mu}_{\text{ind.}} \approx \alpha \vec{E}, \tag{1.3}$$

with the proportionality factor α being the polarizability of the particle. As a rule of thumb, the polarizability of a particle increases with its size. The Stark shift $-\vec{\mu}_{\text{ind.}} \cdot \vec{E}$, of such a molecule (or atom) is thus proportional to $|\vec{E}|^2$ and referred to as *second-order* Stark shift. The force due to this induced Stark shift is often referred to as optical dipole force.

In 1997, the first experimental demonstration of applying the optical dipole force to manipulate a molecular beam was performed by Henrik Stapelfeldt *et al.* [109]. They

deflected CS_2 molecules from a jet at 450 m/s (seeded expansion) and 800 m/s (pure expansion) using a 14 ns long Nd:YAG pulse.

In 2004, a single-stage optical decelerator was demonstrated on the non-polar benzene molecule using a focused 15 ns long laser pulse also from a Nd:YAG. The laser pulse with an intensity of approximately $1.6 \cdot 10^{12}\,\mathrm{W/cm^2}$ is aligned perpendicularly to the molecular beam. This way, a packet of benzene molecules was slowed by 25 m/s from the initial velocity of 320 m/s [110].

Already in 2002, the same group proposed a more sophisticated laser beam setup to achieve a larger overall deceleration that is depicted in Figure 1.8. By using two counter-propagating laser beams, a moving 1D optical lattice can be formed. These moving potential wells are true 3D traps for molecules [111]. This experiment obviously requires careful spatial and temporal laser alignment. The speed of the molecule traps in the laboratory frame is $v_{\mathrm{trap}} = \Delta\omega\lambda/(4\pi)\sin(\phi/2)$ with the difference of the laser frequencies $\Delta\omega$, the mean laser wavelength λ and the angle between the two laser beams ϕ. In 2006, this setup was used to decelerate NO molecules from a pulsed supersonic jet from an initial forward velocity of 400 m/s to 270 m/s [108, 112].

The number of slow molecules that can be produced with optical deceleration, however, is small because the trap volume that is given by the size of the focused laser beam is very small ($\sim \mu\mathrm{m}^3$). Increasing the laser power to achieve stronger deceleration was not possible due to the increasing ionization probability.

The concept of moving traps, however, was adapted to guide and decelerate molecules in low-field-seeking states with electric and magnetic fields. Such an experiment was first realized using electric fields on a micro-structured electrode array with metastable CO molecules [113, 114] and later on in full three dimensions with a decelerator made of ring electrodes [115, 116]. Soon thereafter, trapping molecules from a supersonic expansion was demonstrated using magnetic fields [117]. Recently, a moving trap decelerator was also proposed for microwave fields [118].

1.5.4 with microwave fields

Microwave fields share the capability of generating true 3D field maxima in free space with optical fields. Additionally much larger manipulation volumes are possible due to the larger wavelength that better fit the dimensions of molecular packets typically produced by supersonic expansion and thus better suited for spectroscopy experiments.

In 1975, Hill and Gallagher experimentally demonstrated the deflection of polar CsF molecules in the microwave field of a rectangular resonator at approximately 11 GHz [119]. 14 years later, in 1989, the trapping of atoms using a microwave field in a resonator was proposed [120]. Since atoms do not have a permanent dipole moment and the effect of the polarizability is very small at the small field strength generated with typical microwave fields, Agosta *et al.* planned to exploit the Zeeman interaction of the atom's magnetic moment $\mu_{\mathrm{magn.}}$ with the magnetic component of the microwave field. In 1994, Spreeuw *et al.* demonstrated trapping of laser-cooled Cs atoms (μK) in the magnetic field of the $TE_{1,1,1}$ mode of a spherical resonator with up to 83 W of microwave power [121].

In the 2000s, the advances in manipulating the motion of polar molecules and the increasing possibilities of decelerating molecular packets led to a variety of trap designs

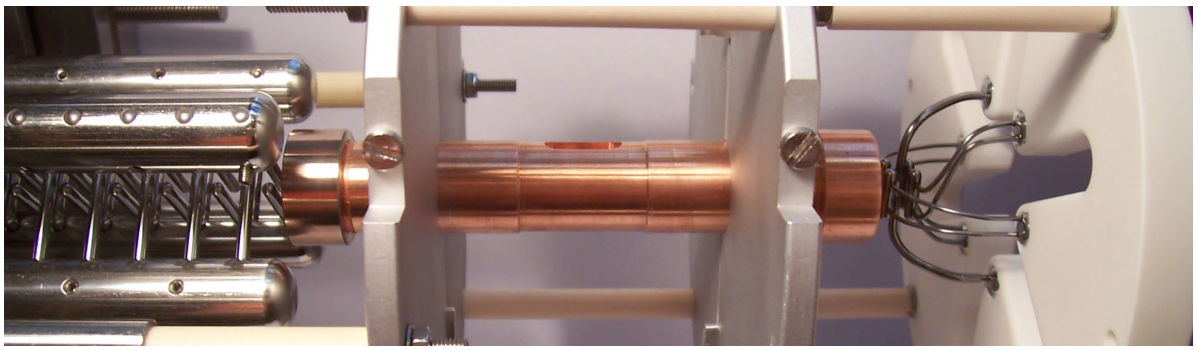

Figure 1.9: First microwave-lens setup to demonstrate focusing of slow ammonia molecules by cavity-enhanced microwave fields utilized by Odashima *et al.* [124]. On the left, a part of the Stark decelerator is shown that is used to pre-decelerate the ammonia molecules.

for polar molecules [95, 105, 106, 122], which provided longer interaction times with probing radiation and new studies measuring the decay of certain trapped states by measuring the trap losses [82, 98].

In 2004, a microwave trap for polar molecules in high-field-seeking states was proposed by David DeMille and coworkers [122]. The suggested setup consisted of an open Fabry–Pérot resonator with 2 kW of input power. In 2005, Enomoto and Momose proposed a microwave decelerator based on a similar resonator design [123]. For deceleration, switching of the field or amplitude modulation is required to extract kinetic energy from the molecules.

The scope of the experiments described in this thesis is to explore and rejuvenate the method pioneered by Hill and Gallagher in 1975 [119]: the application of resonator-enhanced microwave fields to manipulate the motion of polar molecules from typical molecular-beam sources. The advantage of microwave fields are a manipulation volume on the order of the wavelength of the microwave radiation, thus 100–1000s of cubic millimeters, and the true 3D field maxima are an important prerequisite for manipulating molecules in high-field-seeking states. The typical electric field gradients are, however, much smaller than in a focused laser beam, so that first-order Stark shifts are necessary to achieve significant dipole forces. This limits the species that can be manipulated to polar molecules, preferably with a favorable dipole moment-to-mass ratio, such as ammonia ($^{14}NH_3$, $\mu = 1.47\,\mathrm{D}$ and $\mathrm{m} = 17\,\mathrm{u}$). The interaction, the AC-Stark effect that is covered in greater detail in Section 3.4, is particularly strong if near-resonant radiation is applied. This makes this technique applicable to medium-sized and large molecules because their rotational constants and thus the rotational transitions are typically in the microwave region.

A first step was the development of a microwave lens, successfully demonstrated in 2010 using a closed cylindrically-symmetric microwave resonator and Stark pre-decelerated ammonia molecules [124]. A photograph of this first microwave lens is shown in Figure 1.9. In this thesis, the details of that work, more recent advances and experimental results for motion manipulation of polar molecules in their high-field-seeking states using resonator-enhanced microwaves are presented. In this context, also the most

important basics are summarized: the analytic solutions of the electromagnetic fields in closed cylindrically symmetric waveguides and resonators, the open Fabry–Pérot resonator and the interactions of para-ammonia molecules ($^{14}NH_3$) in the rovibronic ground state with electric fields. The experimental results for microwave manipulation in two and three dimensions are presented and discussed. That is

- focusing, with the transverse electric $TE_{1,1,p}$ mode ($p = 1, 2$) [124, 125], and
- guiding, acceleration and deceleration using the $TEM_{0,0,6}$ mode in an open resonator as well as the $TE_{1,1,12}$ mode in a closed resonator [125, 126].

Another part of this thesis suggests improved resonator setups to extend microwave deceleration to a) also trapping of ammonia molecules and b) the deceleration of larger and more complex molecular species. For this, an alternative source for cold molecules, the buffer-gas cell, is investigated and experimental results from a measurement of the velocity distribution of a buffer-gas cooled beam of benzonitrile are shown.

Other research groups worldwide are also investigating microwave fields for motion manipulation of neutral polar molecules: In 2012, Katsunari Enomoto *et al.* proposed a superconducting cavity similar to the closed microwave decelerator described in this thesis. They mounted the resonator that is coated on the inside with a lead-tin alloy onto a cryostat and achieved a quality factor of about 10^6 at 4 K [127]. Experimental results of this device have not been published to date. In 2013, the same group experimentally demonstrated microwave focusing of the $J = 0$ ground state of acetonitrile CH_3N molecules in the $TM_{0,1,p}$ mode microwave field of a closed cylindrically symmetric microwave resonator. In order to reduce the initial velocity of the supersonically expanded molecular beam, they employed a counter-rotating nozzle [40]. In addition they cooled the resonator to circa 77 K using liquid nitrogen and achieved a loaded quality factor of more than 10 000.

In 2014, Hu *et al.* proposed decelerating polar molecules in moving microwave lattices in a cylindrically symmetric waveguide. The moving lattices are generated by coupling two microwave sources to the waveguide. By tuning the relative phase of both inputs, the speed of the moving lattices can be changed. In this proposal, the loss in field strength, due to the fact that no resonator is used, should be compensated by several kilowatts of input power [118].

Another setup using microwaves for trapping polar molecules in their ground states was proposed in 2014 by the group of Michael Tarbutt [128]. They plan to employ the $TEM_{0,0,3}$ mode according to their nomenclature (which corresponds to the $TEM_{0,0,2}$ mode according to the nomenclature used in this thesis, Section 2.9,) in a Fabry–Pérot type resonator at a resonance frequency of circa 14.5 GHz and with 1.5 kW of input power. This way a maximum electric field of 39 kV/cm can be generated and consequently a trap depth of 400 mK for the ground state of the diatomic CaF molecule.

1.6 What are they good for?

Cold molecules are a key ingredient in a variety of experiments from collision studies to quantum chemistry and high-resolution spectroscopy experiments, see also Figure 1.1.

They can be prepared in single quantum states (internal degree of freedom) and with a well-defined velocity (external degree of freedom). In addition, they allow insight into a new quantum world due to the more complex internal structure if compared to atoms. In the ultra-cold regime this has interesting implications because of the long-range dipole-dipole interactions between polar molecules, for example, that are not present in ultra-cold atomic samples.

Slow and cold molecules are particularly interesting for high-resolution spectroscopy experiments. The precision that can be achieved with a monochromatic spectroscopic measurement is ultimately limited by the interaction time Δt of the particle with the probing radiation, as illustrated in Figure 1.10.

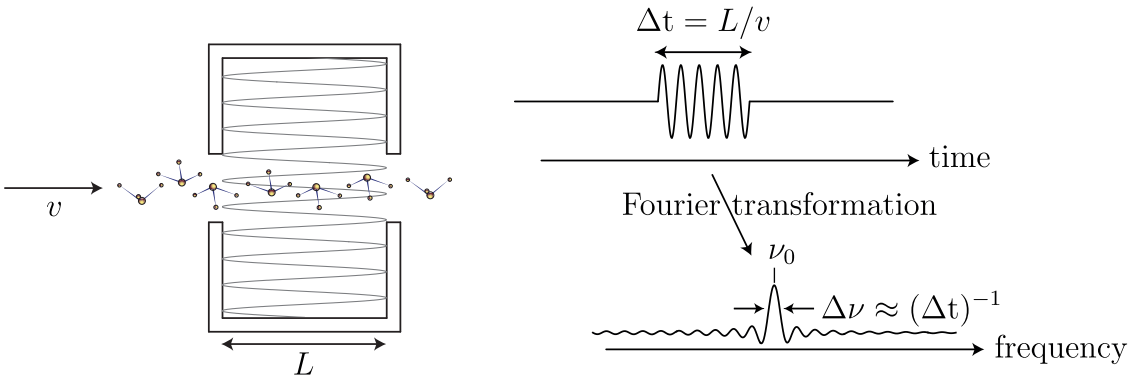

Figure 1.10: Illustration of transit-time broadening. Adapted from Reference [129]

Assuming an interaction region of about one meter and mean particle velocities of several hundred meters per second, which are typical values for room temperature molecular samples, the interaction time is on the order of milliseconds. Even if the probing radiation is spectrally pure with frequency ν_0, the molecules will see a broadened frequency spectrum $\Delta\nu$ due to the limited transit time. This so-called transit-time broadening is inversely proportional to the transit time:

$$\Delta\nu \propto (\Delta t)^{-1}. \tag{1.4}$$

That means for room temperature molecules, the lower resolution limit amounts to kHz. If higher precision is required, the interaction time has to be increased, either by enlarging the interaction zone or by slowing down the sample particles.

In alternative experiments coherence is temporary induced in a molecular ensemble, the spectrum is obtained by recording and Fourier transforming the free-induction decay, such as chirped-pulse Fourier-transform microwave spectroscopy or nuclear magnetic resonance. In microwave spectroscopy, the resolution is limited by the duration that the free-induction decay can be recorded, which can be increased by using slow molecules.

In the following, a selection of experiments will be discussed that would benefit from increased transit times and hence slow molecules.

1.6.1 The search for an eEDM

One of the many experiments that require high-precision and thus could benefit from slow polar molecules is the search for a non-zero electric dipole moment of the electron

(eEDM, d_e). Its actual measurement or at least an improved upper limit of the eEDM can have interesting consequences for physical models. The Standard model of particle physics predicts a value of $10^{-38}\,\mathrm{e\,cm}$, which is much smaller than the precision of the currently most advanced experiments: the most recent experiment by the ACME collaboration gives an upper limit of $|d_e| < 8.7 \cdot 10^{-29}\,\mathrm{e\,cm}$ [130]. However, models beyond the Standard model — string theory, super symmetry and others — usually predict larger values for the eEDM that are coming in reach of the currently achievable experimental precision. A non-zero EDM has further implication such as the breaking of time-reversal (T) symmetry as well as the breaking of parity (P) symmetry. The violation of charge-conjugation and parity (CP) has already been observed in the decay of certain fundamental particles. CP violation could be a reason for the imbalance of matter versus anti-matter. Here, the Standard model prediction is too small to account for the imbalance actually observed in the universe. CP violation due to the eEDM could be an additional source of this imbalance and might contribute to answer the question why our universe exists the way it does and is not only filled with light from massive matter-antimatter annihilation.

The experiments in search for a non-zero eEDM measure an energy difference of the form $\Delta E = \vec{d_e} \cdot \vec{E}$ which requires the strongest possible, homogeneous electric fields. It has proven to be most promising to use certain states of atoms or molecules with heavy nuclei, such as thallium [131], YbF [132, 133] and ThO [130]. Electrons close to heavy nuclei are typically very fast and thus relativistic effects become important. A consequence is a strong field enhancement by many orders of magnitude if the atom or molecule is put into an external field. This field enhancement is particularly strong in polar molecules.

Currently, the most advanced experiments use or plan to use buffer-gas sources to produce slow beams of heavy molecules. These beams could in principle benefit from a beam manipulation technique that is applicable to molecules in high-field-seeking states, such as microwave deceleration, to further decrease the forward speed of the molecules or to confine them.

1.6.2 The search for drifting constants

Another application of cold, slow molecules in high-resolution spectroscopy regards natural constants and the question whether these vary over time. Especially changes of the dimensionless constants would have strange implications on the universe and the physical laws. One possibility to address this question is to compare spectra that depend on the proton-to-electron mass ratio ($m_p/m_e = 1836.15267245(75)$) from laboratory measurements with astrophysical data obtained from galaxies very far away. The information from these galaxies can be billions of years old so that already small deviations in the natural constant per year are in principle detectable.

The inversion transition of ammonia, which is commonly found in interstellar space, is a sensitive probe for the proton-to-electron mass ratio because the inversion transition depends strongly on the reduced mass of the molecule. This can be seen from the large difference in the inversion splitting of 1.59 GHz in $^{14}ND_3$ versus 23.7 GHz in $^{14}NH_3$. Other molecules than ammonia [134] that have been used for this kind of measurement include molecular hydrogen [135] and methanol CH_3OH [136]. So far the results are

inconclusive, i.e., consistent with zero deviation of the proton-to-electron mass ratio. The light from distant galaxies or quasars is substantially red-shifted and it is not quite clear what effects might tamper with the light on its way to earth or whether temporal drifts in the early ages of the universe would still be occurring today. Consequently earth-bound experiments are underway to measure temporal drifts on much shorter time scales (years rather than billions of years). Naturally, these experiments require a very high spectral precision [137, 138].

1.6.3 Cold collisions and cold chemistry

Another research field that makes use of the properties of cold molecules is the study of (cold) molecular collisions to gain insight into the quantum dynamics of chemical reactions and intermolecular interactions [2, 3].

A collision of a small molecule with an atom or a second molecule poses a mathematical problem (three-body or many-body problem) that is too complex to be solved analytically. In order to reduce the complexity of such a collision, it is imperative to control the ingoing and outgoing internal and external degrees of freedom. The input parameters can be carefully prepared using the molecular beam techniques mentioned above [139]. Then the molecules are prepared in a single quantum state with a well-defined velocity and a small velocity spread. Sophisticated detection techniques, using high-resolution lasers for laser induced fluorescence detection (LIF, see also Sec. 6.2) or resonant multi-photon ionization (REMPI, see also Sec. 4.5) allow for precise state-selective detection. With photo-resonant detection schemes, velocity-map imaging [140, 141] can be used, which allows the measurement of the kinetic energies of the ionized species by projecting their Newton sphere onto a two-dimensional detector, for example a phosphor screen. A mathematical transformation, the reverse Abel transformation, then gives access to the 3D Newton sphere of the initially ionized particle.

Here, *cold* is again used as synonym for collisions at very low energies, below 1 K, as can be obtained for example from decelerated molecular beams [79]. Alternatively, collisions within a trap or collisions of trapped particles with a molecular beam can be employed [142, 143]. In a recent experiment, conformer-selected 3-aminophenol molecules in cis or trans configuration were scattered off a laser-cooled Ca^+ Coulomb crystal. The reaction rates could be monitored by observing the removal of the Ca^+ ions from the crystal. The rate constant for the reaction of the calcium cation with the cis-conformer compared to the trans-conformer is enhanced by a factor of two [144].

Another pathway makes use of the small relative velocities in a molecular beam. By crossing fast molecular beams in the laboratory frame, low energy collisions can also be obtained by choosing small crossing angles [145–147].

Very low collision energies are particularly interesting because quantum effects such as tunneling and so-called scattering resonances play an increasingly important role in the collision process. A scattering resonance describes the process when the collision energy becomes resonant with a bound state of the complex made from the collision partners. These resonances have, for example, a strong influence on the collision cross sections, thus they provide benchmark systems for quantum scattering calculations [79, 145, 148, 149].

1.7 This Thesis

As mentioned in Section 1.5.4, it is the scope of the research presented in this thesis to manipulate the motion of neutral polar molecules in high-field-seeking states using microwave fields which opens the door towards applications with ground-state molecules and larger species. For this, resonator-enhanced microwave fields are applied. In Chapter 2, analytic solutions for cylindrically symmetric microwave resonators are derived. The solutions include electric and magnetic fields and the resonance frequencies for the relevant modes in closed resonators as well as an open Fabry–Pérot type resonator. Furthermore, losses in the resonator are discussed and the quality factor is derived. Chapter 3 is a review of the properties of ammonia, in particular the interaction of the para-ammonia ground state with electric fields. An overview of the experimental setup and the experimental details regarding the motion manipulation of neutral polar molecules and the detection of ground-state ammonia molecules are explained in detail in Chapter 4. In Chapter 5, the experimental results for microwave focusing are presented, followed by the results from the microwave deceleration experiments. First, using the open resonator and second, more successfully, in a closed microwave decelerator. With this setup, guiding, acceleration, and deceleration were achieved with kinetic energy changes of up to 60%. This is followed by a feasibility study of a new design with two consecutive microwave resonators. The possible benefits are presented by comparing simulated results from the dual-resonator setup with the closed-$TE_{1,1,12}$ mode microwave decelerator. Chapter 6 is dedicated to motion manipulation of medium-sized and larger molecules using microwave fields. An experiment to determine the velocity distribution of a beam of benzonitrile molecules from a buffer-gas cell is presented as well as a proposed experimental setup for focusing a supersonic beam of aminobenzonitrile molecules. In the last section of this chapter, an approach to simplified AC-Stark-shift calculations using the dressed-state model, is shown for these larger and more complex molecules. Chapter 7 concludes this thesis.

2 Microwave resonators

In the following chapter, the basics for calculating the fields in resonators will be summarized with emphasize on open and closed cylindrically symmetric resonators. The chapter is based on References [150–152].

First, Maxwell's equations are introduced and from this, the wave equation is derived. The wave equation is reduced to two dimensions, considering an electromagnetic wave propagating along a particular spatial direction. By including the influence of a surrounding conductor, the propagation of the electromagnetic wave in a waveguide is discussed. From this, the independent sets of solutions that are the transverse electric (TE), transverse magnetic (TM) and transverse electromagnetic (TEM) modes are explained and the solutions for the electric and magnetic fields in a cylindrically symmetric waveguide are derived. By closing the waveguide on both ends, a closed cylindrically symmetric resonator is formed and additional boundary conditions are introduced. In the next section, the electric and magnetic fields for both the TE and TM modes in a closed cylindrically symmetric resonator are derived and the resonance frequency is introduced. A specific example with solutions for all six electric and magnetic field components is derived for the $\mathrm{TE}_{1,1,p}$ mode. In the next section, the loss mechanisms in a resonator are investigated. Based on the losses in the cavity, the ring-down time of the electric field and the electric field strength are calculated. A brief intermezzo describes an alternative, open resonator design. This chapter closes by showing how to apply these different resonators to motion-manipulation experiments for polar molecules and by discussing the influence of the conductivity of the resonator material and how to improve it.

2.1 Maxwell's equations and symmetry

Maxwell's equations are an important part of the foundation of classical electrodynamics. Gauss' law,

$$\vec{\nabla} \cdot \vec{E} = \frac{\rho}{\epsilon_0},$$

describes how an electric field, $\vec{E}$, is generated by an electric charge density, ρ. The constant $\epsilon_0 = 8.852 \cdot 10^{-12}\ \frac{\mathrm{As}}{\mathrm{Vm}}$ is the permittivity of vacuum. Gauss' law for magnetism,

$$\vec{\nabla} \cdot \vec{B} = 0,$$

states that the divergence of the magnetic field, $\vec{B}$, is zero. In other words: Magnetic fields are a solenoidal vector field. Faraday's law of induction,

$$\vec{\nabla} \times \vec{E} = -\frac{\partial \vec{B}}{\partial t},$$

says that an electric field will be induced by a time-dependent magnetic field. Finally, Ampere's law,

$$\vec{\nabla} \times \vec{B} = \mu_0 \left(\vec{J} + \epsilon_0 \frac{\partial \vec{E}}{\partial t} \right),$$

states that the magnetic field can be generated by moving charges (current), $\vec{J}$, or time-dependent electric fields. The constant $\mu_0 = 4\pi \cdot 10^{-7} \frac{\mathrm{Am}}{\mathrm{Vs}}$ is the permeability of vacuum.

Assuming an electromagnetic wave propagating along the +z-axis of a Cartesian coordinate system with time dependence $e^{-i\omega t}$, then the transverse field components can be separated from the longitudinal field component:

$$\vec{E}\,(x, y, z, t) = \vec{E}\,(x, y)\, e^{-ikz - i\omega t},$$
$$\vec{B}\,(x, y, z, t) = \vec{B}\,(x, y)\, e^{-ikz - i\omega t}.$$

Furthermore, let us assume a hollow and ideally conducting metal cylinder along z, uniformly filled with a dielectric medium of permeability $\mu = \mu_r \mu_0$ and permittivity $\epsilon = \epsilon_r \epsilon_0$. The index 0 indicates constants in vacuum and the index r the relative value of the dielectric medium with respect to vacuum. Maxwell's equations then take the following form:

$$\vec{\nabla} \times \vec{E} = i\omega \vec{B}, \tag{2.1}$$
$$\vec{\nabla} \times \vec{B} = -i\mu\epsilon\omega \vec{E}, \tag{2.2}$$
$$\vec{\nabla} \cdot \vec{B} = 0, \tag{2.3}$$
$$\vec{\nabla} \cdot \vec{E} = 0. \tag{2.4}$$

Maxwell's equations satisfy the wave equation, $\frac{\partial^2}{\partial t^2}\psi = c^2 \vec{\nabla}^2 \psi$, which can be written as:

$$\left(\vec{\nabla}^2 + \mu\epsilon\omega^2 \right) \vec{E} = 0, \text{ and} \tag{2.5}$$
$$\left(\vec{\nabla}^2 + \mu\epsilon\omega^2 \right) \vec{B} = 0, \tag{2.6}$$

The explicit z-dependence (e^{-ikz}) together with $\vec{\nabla}_t^2 = \vec{\nabla}^2 - \partial^2/\partial z^2$ can be used to simplify these wave equations to

$$\left(\vec{\nabla}_t^2 + \underbrace{\left(\mu\epsilon\omega^2 - k^2 \right)}_{=\gamma^2} \right) \cdot \begin{pmatrix} \vec{E} \\ \vec{B} \end{pmatrix} = 0. \tag{2.7}$$

The propagation direction along the z-axis makes it useful to separate the fields into components parallel and orthogonal to $\vec{z}$:

$$\vec{E} = \vec{E}_t + \hat{z} E_z \text{ and } \vec{B} = \vec{B}_t + \hat{z} B_z. \tag{2.8}$$

Here, $\hat{z} = \vec{z}/|\vec{z}|$ is the unit vector in z-direction. Then we find from the first two of Maxwell's equations (Eq. 2.1 and 2.2):

$$\vec{E}_t = \frac{1}{\mu\epsilon\omega^2 - k^2} \left(\vec{\nabla}_t \frac{\partial E_z}{\partial z} - i\omega\, \hat{z} \times \vec{\nabla}_t B_z \right) \tag{2.9}$$

and

$$\vec{B}_t = \frac{1}{\mu\epsilon\omega^2 - k^2}\left(\vec{\nabla}_t \frac{\partial B_z}{\partial z} + i\mu\epsilon\omega\ \hat{z} \times \vec{\nabla}_t E_z\right). \tag{2.10}$$

These two equations show that the transverse field components $\vec{E}_t$, $\vec{B}_t$, respectively, can be calculated from the longitudinal components E_z, B_z. That means that solving the wave equation (Eq. 2.7) can be reduced to finding a solution for the longitudinal electric and magnetic field components. Then, the transverse field components can simply be calculated from Equations 2.9 and 2.10.

2.2 Waveguides

So far only the symmetry aspects of an electromagnetic wave traveling in the z-direction have been considered. Since we are interested in waveguides and waveguide-like resonators it is necessary to include the effects of the surrounding conductor. As a first approximation it is considered to be a perfect conductor, which means the electric and magnetic fields have to satisfy the boundary conditions at its surface:

$$\hat{n} \times \vec{E} = 0 \text{ and} \tag{2.11}$$

$$\hat{n} \cdot \vec{B} = 0. \tag{2.12}$$

Here, $\hat{n}$ is the unitary normal vector on the conducting surface of the waveguide, S. Splitting the electric and magnetic fields into their transverse and longitudinal components (Equations 2.8), the boundary conditions in the waveguide can be simplified to

$$E_z|_S = 0, \tag{2.13}$$

i.e., the electric field component along the longitudinal direction has to vanish at the conductor's surface (S) of the waveguide and

$$\left.\frac{\partial B_z}{\partial n}\right|_S = 0. \tag{2.14}$$

The lines of constant magnetic field are perpendicular to the conductor at its surface. The wave equation, Equation 2.7, and the boundary conditions, Equations 2.13 and 2.14, form an initial value problem. Due to the fact that the boundary conditions to $\vec{E}_z$ and $\vec{B}_z$ cannot both be satisfied everywhere, the solutions of the initial value problem are to be separated into three independent categories:

- The so-called transverse magnetic (TM) modes with $B_z = 0$ everywhere.
- The so-called transverse electric (TE) modes with $E_z = 0$ everywhere.
- The so-called transverse electromagnetic (TEM) modes with $E_z = B_z = 0$ everywhere.

The last set of solutions gives only the trivial result $\vec{E} = \vec{B} = 0$ in a cylindrically symmetric waveguide. However, these solutions are important in coaxial cables and the open spherical resonator that is discussed in Section 2.9.

2.3 Cylindrically symmetric waveguides

Let us assume the propagation of an electromagnetic wave in a cylindrical and hollow waveguide with a constant cross section. The z-dependence from above (e^{-ikz}) ensures a propagation of the electromagnetic wave in $+z$-direction. Then Equations 2.9 and 2.10 can be simplified further. In the case of TE modes ($\vec{E}_z = 0$), we find

$$\vec{E}_t = -\frac{i\omega}{\gamma^2}\, \hat{z} \times \vec{B}_t, \tag{2.15}$$

$$\vec{B}_t = -\frac{ik}{\gamma^2}\, \vec{\nabla}_t B_z. \tag{2.16}$$

$\gamma^2 = \mu\epsilon\omega^2 - k^2$ is known from the previous section. For TM modes ($\vec{B}_z = 0$), one finds

$$\vec{E}_t = -\frac{ik}{\gamma^2}\, \vec{\nabla}_t E_z, \tag{2.17}$$

$$\vec{B}_t = -\frac{\mu\epsilon\omega}{k}\, \hat{z} \times \vec{E}_t. \tag{2.18}$$

Here, it can be seen how in the case of TE (TM) modes every non-zero field component can be calculated from E_z B_z). Hence, $\psi = E_z$ (B_z) is a solution to the two-dimensional wave equation (Eq. 2.7 in Cartesian coordinates and Eq. 2.19 in cylindrical coordinates) and is called the scalar wavefunction.

$$\frac{1}{\rho}\frac{\partial}{\partial\rho}\left(\rho\frac{\partial\psi}{\partial\rho}\right) + \frac{1}{\rho^2}\frac{\partial^2\psi}{\partial\phi^2} + \gamma^2 = 0. \tag{2.19}$$

The constant γ^2 has to be positive, so that the boundary conditions (Eq. 2.13 and 2.14) can be fulfilled in a non-trivial way. A useful definition is the cut-off frequency of a waveguide, ω_c,

$$\omega_c = \frac{\gamma}{\sqrt{\mu\epsilon}}, \tag{2.20}$$

that marks the border between transmission ($\omega > \omega_c$, thus $\gamma^2 > 0$) and attenuation ($\omega < \omega_c$, thus $\gamma^2 < 0$) of an electromagnetic wave in the waveguide.

For the solution to the wave equation (Equation 2.19) in cylindrical coordinates with $\vec{z}$ along the symmetry axis of the cylinder, we choose the Ansatz $\psi(\rho, \phi) = R(\rho)\Phi(\phi)$. Then,

$$\psi(\rho, \phi) = J_m(\gamma_{mn}\rho)\cos(m\phi) \tag{2.21}$$

solves the differential equation. The J_m are the Bessel functions of the first kind and the mth order. These solutions have to fulfill the boundary conditions (Eq. 2.13 and 2.14), which can be translated into the terms of the scalar wavefunction:

$$\left.\frac{\partial\psi}{\partial n}\right|_S = 0 \text{ for TE modes and} \tag{2.22}$$

$$\psi|_S = 0 \text{ for TM modes.} \tag{2.23}$$

Consequently, for the radial term in the case of TE modes, we find

$$\left.\frac{\partial}{\partial\rho} J_m(\gamma_{m,n}\rho)\right|_{\rho=R} = 0$$

The derivative of the Bessel function of the first kind and mth order has an infinite number of roots. The notation $x'_{m,n}$ stands for the nth root of the first derivative of the mth-order Bessel function. Thus, the solution for the constant γ for TE modes can be found according to

$$\gamma_{m,n} = \frac{x'_{m,n}}{R}. \tag{2.24}$$

For TM modes, the boundary condition (Eq. 2.23) in Equation 2.21 requires

$$\gamma_{m,n} = \frac{x_{m,n}}{R}. \tag{2.25}$$

The $x_{m,n}$ is the nth root of the mth order Bessel function J_m. The first three roots of J_m and their first derivatives J'_m can be found in Table 2.1. The lowest value is found for $x'_{1,1}$, that means the lowest mode in a cylindrically symmetric waveguide is always the $TE_{1,1}$ mode.

Table 2.1: The nth roots of the Bessel functions J_m and its derivative J'_m. Note that the lowest value is obtained for $x'_{1,1} = 1.841$ which means that the $TE_{1,1}$ mode is the fundamental mode in a cylindrically symmetric waveguide.

	TE-modes			TM-modes		
	$x'_{m,1}$	$x'_{m,2}$	$x'_{m,3}$	$x_{m,1}$	$x_{m,2}$	$x_{m,3}$
$m = 0$	3.832	7.016	10.173	2.405	5.520	8.654
$m = 1$	1.841	5.331	8.536	3.832	7.016	10.173
$m = 2$	3.054	6.706	9.969	5.136	8.417	11.620

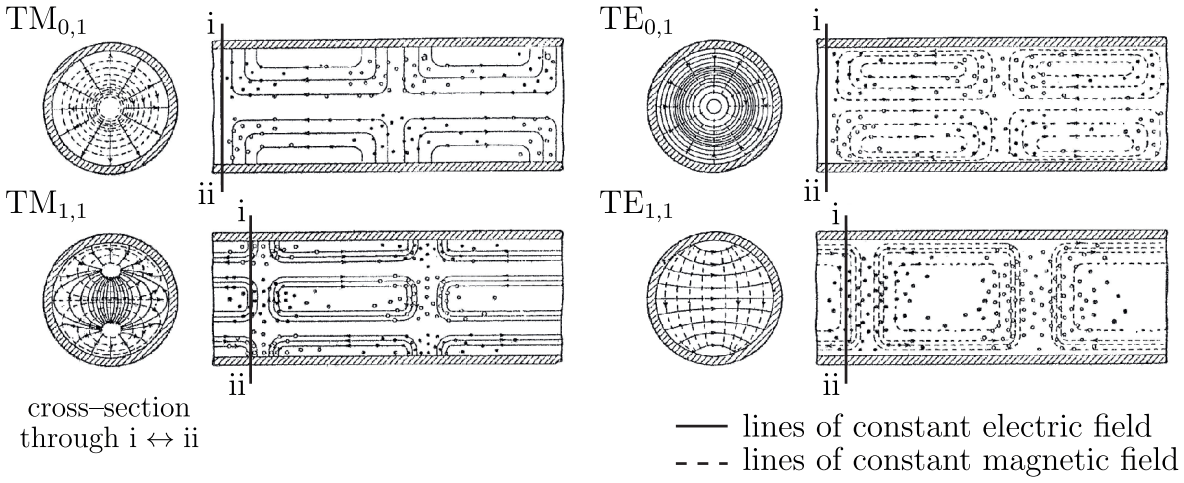

Figure 2.1: Lines of constant electric and magnetic field of the $TM_{0,1}$, $TM_{1,1}$, $TE_{0,1}$ and $TE_{1,1}$ modes in a cylindrical waveguide. The right side of each mode picture shows a longitudinal cut through the waveguide and the left sides show the lines of constant field strength in transverse slice through i ↔ ii. Adapted from Reference [153].

This mode features an electric field maximum on the symmetry axis of the waveguide and is thus ideal for the transverse confinement of neutral polar molecules in high-field-seeking states. Plots of the lines of constant electric and magnetic field for the lowest TE and TM modes ($TM_{0,1}$, $TM_{1,1}$, $TE_{0,1}$ and $TE_{1,1}$) are displayed in Figure 2.1.

2.4 Cylindrical microwave resonators

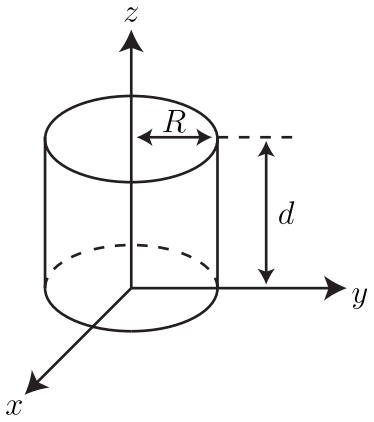

Figure 2.2: Scheme of a cylindrically symmetric microwave resonator, with radius R and length d in a Cartesian coordinate system.

A cylindrically symmetric resonator is a waveguide with radius R and length d that is closed on both ends with flat, ideally conducting surfaces perpendicular to the cylinder axis (see Fig. 2.2). In contrast to the waveguide, the electromagnetic wave is reflected back and forth between the front and the end face. This standing wave results in a z-dependence of the electric field $E(\rho, \phi, z, t) = E_t(\rho, \phi)E_z(z)e^{-i\omega t}$ according to

$$E_z(z) = A \sin kz + B \cos kz$$

which can only be fulfilled at the front face, $z = 0$, and the end face, $z = d$, if

$$k = \frac{p\pi}{d}. \tag{2.26}$$

Here, $p = 0, 1, 2, \ldots$ is the longitudinal mode number. The boundary conditions 2.11 at the front and end faces can be translated into $\hat{z} \times \vec{E}_t(z = 0, z = d) = 0$, i.e., $\vec{E}_t$ vanishes at $z = 0$ and $z = d$. In the case of TM modes ($B_z = 0$), it follows from the term $\frac{\partial E}{\partial z}$ in Equation 2.9, that this requires $A = 0$ and $B = 1$:

$$E_z = E_0 \psi(\rho, \phi) \cos\left(\frac{p\pi z}{d}\right).$$

E_0 is the electric field strength. For TE modes ($E_z = 0$), the vanishing of $\vec{E}_t$ is equivalent to $B_z = 0$ at $z = 0$ and $z = d$ (see Eq. 2.9), i.e., $A = 1$ and $B = 0$. Thus,

$$B_z = B_0 \psi(\rho, \phi) \sin\left(\frac{p\pi z}{d}\right). \tag{2.27}$$

Here, $p = 0$ is the trivial solution ($\vec{E} = \vec{B} = 0$), i.e., in the case of TE modes, the longitudinal mode number has to be equal to one or larger ($p \geq 1$). B_0 is the magnetic

flux density. The resonance frequencies of the microwave resonator can be obtained from Equation 2.19 with Equation 2.26:

$$\gamma_{m,n}^2 = \mu\epsilon\omega^2 - \left(\frac{p\pi}{d}\right)^2.$$

Then the resonance frequencies for TE modes are

$$\omega_{m,n,p} = \frac{c}{\sqrt{\mu_r\epsilon_r}}\sqrt{\frac{x'^2_{m,n}}{R^2} + \frac{p^2\pi^2}{d^2}}, \tag{2.28}$$

and for TM modes we get

$$\omega_{m,n,p} = \frac{c}{\sqrt{\mu_r\epsilon_r}}\sqrt{\frac{x^2_{m,n}}{R^2} + \frac{p^2\pi^2}{d^2}} \tag{2.29}$$

which can then be used to calculate the resonance frequencies in a cylindrically symmetric resonator. As already shown before, the transverse electric and magnetic field components can be calculated from the longitudinal components. Inserting the solutions for the longitudinal field components E_z and B_z for TE and TM modes in a closed cylindrically symmetric resonator, respectively, into Equations 2.9 and 2.10 one finds:

$$\vec{E}_t = -B_0\frac{i\omega}{\gamma_{m,n}^2}\sin\left(\frac{p\pi z}{d}\right)\hat{z}\times\vec{\nabla}_t\psi(\rho,\phi) \text{ and} \tag{2.30}$$

$$\vec{B}_t = B_0\frac{p\pi}{d\gamma_{m,n}^2}\cos\left(\frac{p\pi z}{d}\right)\vec{\nabla}_t\psi(\rho,\phi) \tag{2.31}$$

for the TE modes and

$$\vec{E}_t = -E_0\frac{p\pi}{d\gamma_{m,n}^2}\sin\left(\frac{p\pi z}{d}\right)\vec{\nabla}_t\psi(\rho,\phi) \text{ and} \tag{2.32}$$

$$\vec{B}_t = \frac{E_0}{c}\frac{i\mu_r\epsilon_r\omega}{c^2\gamma_{m,n}^2}\cos\left(\frac{p\pi z}{d}\right)\hat{z}\times\vec{\nabla}_t\psi(\rho,\phi) \tag{2.33}$$

in the case of TM modes.

2.5 $TE_{1,1,p}$-mode resonators

In the cylindrical waveguide, it is clear from the cut-off frequency (Eq. 2.20) and the roots of the Bessel functions (Table 2.1) that the $TE_{1,1}$ mode is the fundamental mode. For the closed cylindrically symmetric resonator this is true for most cases but with one exception: In a short, cylindrically symmetric resonator with a large diameter ($2R > d$), the mode with the lowest resonance frequency is the $TM_{0,1,0}$ mode, as displayed in Figure 2.3. This is a consequence of the additional longitudinal mode number that can be zero for TM modes but has to be at least one for the TE modes. The resonators used throughout the experiments described in this thesis are long if compared to their radius ($R \ll d$), so the fundamental mode is indeed the $TE_{1,1,p}$ mode. An advantage of fundamental modes is that they can easily be identified in the frequency spectrum.

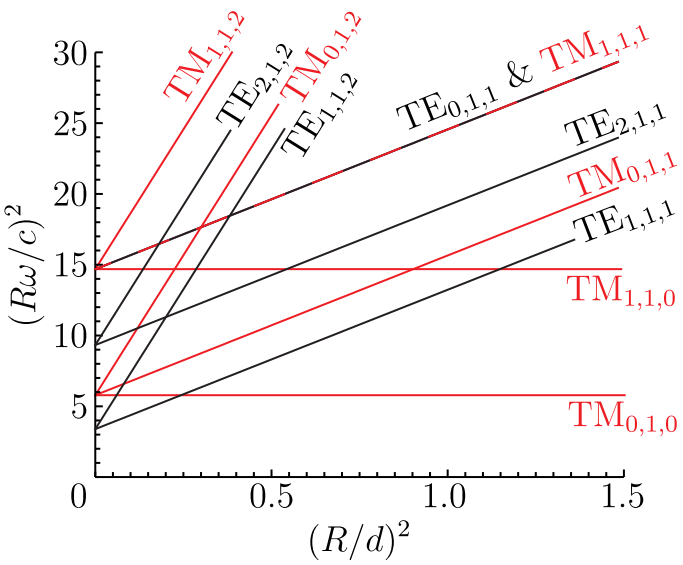

Figure 2.3: Mode chart for the lower $\mathrm{TE}_{n,m,p}$ and $\mathrm{TM}_{n,m,p}$ modes $(n, m, p < 3)$. The abscissa is the ratio of resonator radius over resonator length squared $(R/d)^2$ and the ordinate is in units of $(\omega R/c)^2$.

Furthermore, they guarantee the smallest resonator volume if compared to higher order modes which is beneficial for a high power density that results in strong electric fields. The scalar wavefunction of the $\mathrm{TE}_{1,1,p}$ mode is the special case of Equation 2.34 with n, $m = 1$:

$$\psi(\rho, \phi) = J_1(\gamma_{1,1}\rho)\cos\phi. \tag{2.34}$$

The transverse electric and transverse magnetic field components can be calculated from the scalar wavefunction and from the general resonator solution given in Equations 2.30 and 2.31. For the $\mathrm{TE}_{1,1,p}$ mode the result can be simplified further:

$$\vec{E}_t(\rho, \phi, z) = -B_0 \frac{i\omega}{\gamma_{1,1}^2} \sin\left(\frac{p\pi z}{d}\right) \hat{z} \times \vec{\nabla}_t J_1(\gamma_{1,1}\rho)\cos\phi \tag{2.35}$$

and

$$\vec{B}_t(\rho, \phi, z) = B_0 \frac{p\pi}{d\gamma_{1,1}^2} \cos\left(\frac{p\pi z}{d}\right) \vec{\nabla}_t J_1(\gamma_{1,1}\rho)\cos\phi. \tag{2.36}$$

The derivative of the Bessel function, $\frac{\partial}{\partial x} J_1(ax)$, can be expressed in terms of $J_0(ax)$ and $J_1(ax)$:

$$\frac{d}{dx} J_1(ax) = a\left(J_0(ax) - \frac{1}{ax} J_1(ax)\right).$$

Then the electric field component for the $\mathrm{TE}_{1,1,p}$ mode can be calculated:

$$E_\rho(\rho, \phi, z) = -E_0 \frac{i\omega}{\gamma_{1,1}^2 c} \frac{J_1(\gamma_{1,1}\rho)}{\rho} \sin\phi \sin\left(\frac{p\pi z}{d}\right) \tag{2.37}$$

$$\begin{aligned} E_\phi(\rho, \phi, z) &= -E_0 \frac{i\omega}{\gamma_{1,1}^2 c} \frac{\partial}{\partial\rho} J_1(\gamma_{1,1}\rho)\cos\phi \sin\left(\frac{p\pi z}{d}\right) \\ &= -E_0 \frac{i\omega}{\gamma_{1,1} c} \left(J_0(\gamma_{1,1}\rho) - \frac{J_1(\gamma_{1,1}\rho)}{\gamma_{1,1}\rho}\right) \cos\phi \sin\left(\frac{p\pi z}{d}\right) \end{aligned} \tag{2.38}$$

$$E_z(\rho, \phi, z) = 0. \tag{2.39}$$

In this result, the relation between the electric field strength and the magnetic flux density is used, $B_0 = E_0/c$. From Equation 2.27 we find the longitudinal magnetic field component and by solving Equation 2.36, the transverse magnetic field components can be found:

$$B_\rho(\rho,\phi,z) = B_0 \frac{p\pi}{d\gamma_{1,1}} \left(J_0(\gamma_{1,1}\rho) - \frac{J_1(\gamma_{1,1}\rho)}{\gamma_{1,1}\rho} \right) \cos\phi \cos\left(\frac{p\pi z}{d}\right), \tag{2.40}$$

$$B_\phi(\rho,\phi,z) = -B_0 \frac{p\pi}{d\gamma_{1,1}^2} \frac{J_1(\gamma_{1,1}\rho)}{\rho} \sin\phi \cos\left(\frac{p\pi z}{d}\right), \tag{2.41}$$

$$B_z(\rho,\phi,z) = B_0 J_1(\gamma_{1,1}\rho) \cos\phi \sin\left(\frac{p\pi z}{d}\right). \tag{2.42}$$

At this point, the analytical solutions for the electric and magnetic fields in a cylindrically symmetric closed resonator, in particular for the $TE_{1,1,p}$ mode, are known. The parameter for the electric field strength, E_0, will be addressed in Section 2.8. First, however, the quality factor of a cavity that links the stored energy to power losses will be introduced.

2.6 Unloaded Q_0 of $TE_{m,n,p}$ modes

The quality factor Q of a cavity is a measure for the losses within. It is the ratio of averaged stored energy W to power loss P_{Loss} at a particular resonance frequency ω_0:

$$Q = \omega_0 \frac{W}{P_{Loss}}. \tag{2.43}$$

In other words: the stored energy is Q-fold the amount of energy lost per cycle. This amplitude enhancement at resonance is crucial for the creation of strong electric fields for motion manipulation experiments. In this section, the quality factor of a cylindrically symmetric closed resonator for the $TE_{m,n,p}$ mode will be derived. Power loss can have various reasons:

- dielectric losses if the cavity is filled with a dielectric medium,
- refraction losses in the case of apertures in the resonator, and
- Ohmic losses due to eddy currents induced by the magnetic fields, which are the main focus of this section.

It should be noted that quality factors due to different loss mechanisms add up:

$$\frac{1}{Q_{total}} = \frac{1}{Q_1} + \frac{1}{Q_2} + \dots \tag{2.44}$$

The so-called unloaded quality factor, Q_0, which is discussed in this section, is a property of a completely undisturbed resonator. In any real-life application, the resonator will be connected to a drive or probe circuit. This external circuit has additional losses that have to be added according to Equation 2.44.

The energy densities of the electric and the magnetic field in an electromagnetic wave are equal:

$$\langle u_{EM} \rangle = \langle u_E + u_M \rangle = \epsilon_0 \left\langle \vec{E}(\rho, \phi, z, t)^2 \right\rangle = \frac{1}{\mu_0} \left\langle \vec{B}(\rho, \phi, z, t)^2 \right\rangle .$$

Assuming a linearly polarized plane wave, time averaging gives a factor of ½ and the total, time-averaged energy, W, can be written as:

$$W = \frac{\epsilon_0}{2} \int_0^d \int_0^{2\pi} \int_0^\rho \left| \vec{E}\left(\rho, \phi, z\right) \right|^2 \rho \, d\rho d\phi dz \tag{2.45}$$

$$= \frac{\epsilon_0 \omega_0^2 R^4 B_0^2 \pi d}{8 x'^2_{m,n}} \left[1 - \left(\frac{m}{x'_{m,n}} \right)^2 \right] J_m^2 \left(x'_{m,n} \right) . \tag{2.46}$$

Dielectric losses within the resonator can be neglected because all experiments are conducted in vacuum. To a good approximation, we assume only Ohmic losses. These occur due to the use of real metal as resonator material rather than an ideal conductor. The magnetic fields penetrate into the metal surface, S, and induce currents. Due to finite conductivity, σ, of even the best conductors, power is dissipated according to:

$$P_c = \frac{R_s}{2\mu} \int_S \left| \vec{B}_{\tan} \right|^2 dS. \tag{2.47}$$

Here, $\mu = \mu_r \mu_0$ is the permeability of the conductor and $\vec{B}_{tan}$ is the magnetic field component tangential to the metal surface ($|B_\phi(\rho = R)|^2 + |B_z(\rho = a)|^2$ at the cylinder wall and $|B_\rho(z = 0)|^2 + |B_\phi(z = 0)|^2$ at the front and back faces). $R_s = \sqrt{\mu\omega_0/2\sigma}$ is the surface resistivity of the imperfect conductor and inversely proportional to the square of the conductivity σ. Inserting the magnetic fields of the $\mathrm{TE}_{m,n,p}$ mode into Equation 2.47 gives:

$$P_c = \frac{R_s \pi B_0^2}{2\mu^2} J_m^2 \left(x'_{m,n} \right) \left[\frac{dR}{2} \left[1 + \left(\frac{mp\pi R}{x'^2_{m,n} d} \right)^2 \right] + \left(\frac{p\pi R^2}{x'_{m,n} d} \right)^2 \left(1 - \frac{m^2}{x'^2_{m,n}} \right) \right] . \tag{2.48}$$

Thus, we find the solution for the quality factor by dividing the stored energy of the electromagnetic field, Equation 2.46, by the Ohmic power loss, Equation 2.48 according to Equation 2.43:

$$Q_0 = \frac{\epsilon_0 \mu^2 \omega_0^3 R^4 d}{4 R_s x'^2_{m,n}} \times \frac{1 - \left(\frac{m}{x'_{m,n}} \right)^2}{\frac{dR}{2} \left[1 + \left(\frac{mp\pi R}{x'^2_{m,n} d} \right)^2 \right] + \left(\frac{p\pi R^2}{x'^2_{m,n} d} \right)^2 \left(1 - \left(\frac{m}{x'_{m,n}} \right)^2 \right)} . \tag{2.49}$$

For the special case of the $\mathrm{TE}_{1,1,p}$ mode, this formula can be simplified further:

$$Q_0 \approx \frac{1.471 \epsilon_0 \sqrt{\sigma \mu^3 \omega_0^5} \, d^3 R^3}{10.000 \, d^3 + p^2 (8.590 \, dR^2 + 12.116 \, R^3)} . \tag{2.50}$$

From this formula, the unloaded quality factor Q_0 of the $\mathrm{TE}_{1,1,p}$ mode in a cylindrically symmetric cavity can be calculated. The so-called loaded quality factors of the resonators used throughout the experiments described in this thesis can be found in Chapter 4, where the effects of the coupling into the mode are also discussed. For typical sizes of the microwave lenses a Q_0 factor of about 6000 is estimated. For the closed microwave decelerator this value is on the order of about 11 000.

2.7 Ring-down time

Conservation of energy dictates that the energy dissipated via Ohmic losses and possibly other loss channels is the negative of the decay rate of the energy stored in the electromagnetic field, W. With the quality factor, Equation 2.43, this relation can be expressed as:

$$P_{loss} = -\frac{dW}{dt} = \frac{\omega_0}{Q} W.$$

The solution to this equation is an exponential decay:

$$W(t) = W_0 e^{-t/\tau},$$

with the so-called ring-down time $\tau = Q/\omega_0$ that refers to the time when the stored energy in the resonator drops to 1/e of its original value. The stored energy depends on the square of the electric field strength, so we find for the decay of the electric field:

$$E(t) = E_0 e^{-t/2\tau},$$

When the microwave generation is switched on, the electric field in the resonator is not immediately at full strength. It rather follows an exponential function of the form

$$E(t) = E_0 \left[1 - e^{-t/2\tau}\right]$$

For quality factors up to 10^4 and a resonance frequency of $\omega_0 \approx 2\pi \cdot 23.7\,\mathrm{GHz} = 1.49 \cdot 10^{11}\,\mathrm{s}^{-1}$, the ring-down time is on the order of 135 ns or less. However, larger quality factors of the resonator, see for example Section 2.11, result in longer ring-down times. Superconducting resonators easily reach unloaded quality factors of 10^8, which means that the ring-down time is longer than a millisecond. Such a long ring-down time implies a low switching rate, which can be impractical for many molecular beam manipulation experiments.

2.8 Field strength

The electric field strength E_0 is the magnitude of the electric field and essential for calculating the Stark shifts of the ammonia molecules which are the reason for a force on the molecules in the inhomogeneous microwave field (see for instance Eq. 2.37 and 2.38). In an externally driven microwave resonator on resonance, the energy stored in the field initially increases over time, however, power is constantly dissipated in the resonator walls due to Ohmic losses, which heat up the resonator. This power loss depends on the strength of the electromagnetic field (see Section 2.6) and is thus related to the input power, P_{IN}. After some time, the system reaches an equilibrium in which the power loss equals the input power with a certain amount of energy, W, stored in the electromagnetic field. Then, the power loss in Equation 2.43 can be replaced by the input power, P_{IN}:

$$W = \frac{P_{\mathrm{IN}} Q}{\omega_0}. \tag{2.51}$$

By inserting the stored electric energy, W, of the $TE_{m,n,p}$ mode from Equation 2.46, we find for the electric field strength of the $TE_{m,n,p}$ mode:

$$E_0 = c\sqrt{\frac{8P_{\mathrm{IN}}Q}{\epsilon_0\omega_0^3\pi R^4 d\left[1-\left(\frac{m}{x'_{m,n}}\right)^2\right]}}\frac{x'_{m,n}}{J_m\left(x'_{m,n}\right)}. \tag{2.52}$$

E_0 is not the maximum electric field strength. The maximum electric field strength can be obtained by absorbing additional factors $\omega R(cx'_{n,m})^{-1}$ from Equation 2.35 from the $TE_{1,1,p}$ case which are in principle identical in the more general $TE_{n,m,p}$ case (Equation 2.30). Taking into account, that the maximum of the Bessel function $J_1(x)$ amounts to ½ at $x = 0$, one finds:

$$E_{0,\max} = \sqrt{\frac{2P_{\mathrm{IN}}Q}{\epsilon_0\omega_0\pi R^2 d\left[1-\left(\frac{m}{x'_{m,n}}\right)^2\right]}}\frac{1}{J_m\left(x'_{m,n}\right)}. \tag{2.53}$$

The maximum electric field strength depends on the square root of the quality factor, the square root of the input power, a geometric term that is the resonator volume, $V = \pi R^2 d$, and a term that is entirely mode dependent. For a particular mode, the expression in Equation 2.53 can thus be simplified further. The motion manipulation experiments in the closed resonators are exclusively carried out with the $TE_{1,1,p}$ modes, for which we find

$$E_{0,\max} = \sqrt{\frac{2P_{\mathrm{IN}}Q}{\epsilon_0\omega_0 V\left(x'^2_{1,1}-1\right)}}\frac{x'_{1,1}}{J_1\left(x'_{1,1}\right)} \tag{2.54}$$

$$\tag{2.55}$$

$$= 2.9\cdot\sqrt{\frac{P_{\mathrm{IN}}Q}{\epsilon_0\omega_0 V}}. \tag{2.56}$$

It should be noted that both input power and quality factor do not include coupling effects yet, such as impedance mismatch between the resonator and the feed line. Furthermore, the notation regarding the electric field strength in References [124–126] is different. There, E_0 is the maximum value of the electric field strength in the resonator which in this thesis is denoted as $E_{0,\max}$. The electric field components of the $TE_{1,1,p}$ mode (Eq. 2.37, 2.38 and 2.39) can be written with the maximum electric field strength as pre-factor:

$$E_\rho(\rho,\phi,z) = -2iE_{0,\max}\frac{J_1(\gamma_{1,1}\rho)}{\gamma_{1,1}\rho}\sin\phi\sin\left(\frac{p\pi z}{d}\right) \tag{2.57}$$

$$\begin{aligned} E_\phi(\rho,\phi,z) &= -2iE_{0,\max}\frac{\partial}{\partial\rho}\frac{J_1(\gamma_{1,1}\rho)}{\gamma_{1,1}}\cos\phi\sin\left(\frac{p\pi z}{d}\right) \\ &= -2iE_{0,\max}\left(J_0(\gamma_{1,1}\rho)-\frac{J_1(\gamma_{1,1}\rho)}{\gamma_{1,1}\rho}\right)\cos\phi\sin\left(\frac{p\pi z}{d}\right) \end{aligned} \tag{2.58}$$

$$E_z(\rho,\phi,z) = 0. \tag{2.59}$$

2.9 Open resonators

As an alternative resonator design, an open Fabry–Pérot resonator is considered, similar to what is suggested in Reference [122]. For their use in lasers these resonators have been studied in great detail for over 50 years [154, 155]. Furthermore, these resonators are wide-spread in the field of rotational spectroscopy, since they enhance both the excitation field and the molecular response [156, 157].

In contrast to the closed cylindrically symmetric resonators, open Fabry–Pérot resonators support $\mathrm{TEM}_{p,l,q}$ modes that neither have a longitudinal electric nor a longitudinal magnetic field component. The fundamental $\mathrm{TEM}_{0,0,q}$ mode is of particular interest because it features electric field maxima on the longitudinal resonator axis that are crucial for motion manipulation of polar molecules in high-field-seeking states. Molecules in high-field-seeking states are attracted by the electric field maximum, consequently they experience transverse focusing in the electric field of the $\mathrm{TEM}_{0,0,q}$ mode in an open Fabry–Pérot resonator.

A trap for neutral polar molecules as well as a microwave deceleration experiment using an open spherical resonator were proposed already in 2004 and 2005 [122, 123]. Recently a similar resonator has been realized for the $\mathrm{TEM}_{0,0,3}$ mode at $\nu_{0,0,3} = 14.5\,\mathrm{GHz}$ for trapping polar molecules, see also Reference [128] for further details, but successful trapping was not reported yet.

Another difference between the closed and the open resonators is the significantly higher quality factors that can be reached since the contact of the electromagnetic field with the conductor is limited to the mirror surfaces. On the other hand diffraction losses occur that can be kept small with the appropriate resonator design. Figure 2.4 shows how the length of the resonator, i.e., the mirror distance, and the mirror curvature affect the diffraction losses. The white areas describe the stable regions, where only low diffraction losses occur. Parameter sets that reside in the grey areas are unstable due to large diffraction losses. The most straightforward design consists of two mirrors

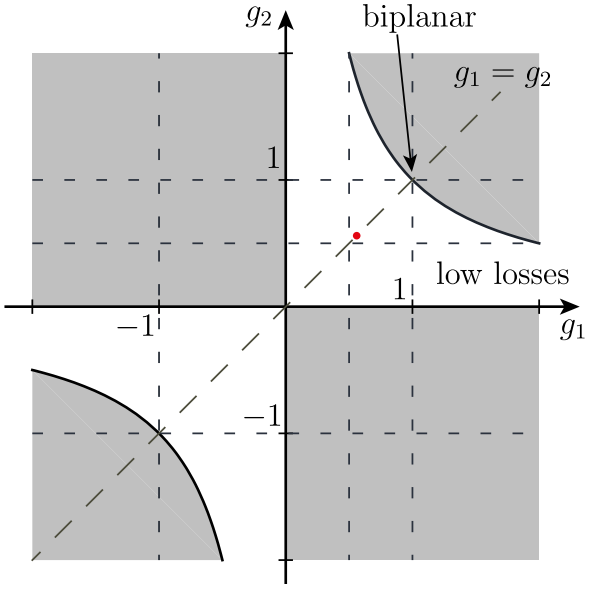

Figure 2.4: Stability diagram for open resonators with the length d between the two mirrors with radii of curvature b_i. Parameters in the white area make good resonators, while parameter sets in the grey-shaded areas lead to unstable results. The diagonal line represents the case $g_1 = g_2$, with $g_i = 1 - \frac{b_i}{d}$, which are setups with equal mirror curvatures, $b_1 = b_2$. The plane-parallel (biplanar) case is indicated, with $b_1 = b_2 = \infty$ as well as a red dot that marks the parameters for the open resonator used in this thesis (see also Sec. 4.2.2).

with identical radii of curvature b_i with the mirror spacing being equal to said curvature

($b_1 = b_2 = d$). However, this particular resonator design is located right in the center of the stability diagram (Fig. 2.4). Already small misalignment can lead to strong diffraction losses, hence a low quality factor and only weak electric fields. A more favorable design is $b_1 = b_2 > d$, for example.

The resonance frequencies for TEM modes in such a Fabry–Pérot resonator can be calculated following:

$$\omega_{p,l,q} = \frac{c}{2d}\left[q + 1 + \frac{1}{\pi}(2p + l + 1)\arccos\left(1 - \frac{d}{b}\right)\right]. \tag{2.60}$$

The electric field distribution for the $\mathrm{TEM}_{0,0,q}$ mode in the open resonator is given by

$$\vec{E}(\rho, \phi, z) = \begin{pmatrix} E_\rho(\rho, z) \\ 0 \\ 0 \end{pmatrix}$$

according to References [123, 157]. The radial component of the electric field has the following form:

$$E_\rho = \frac{E_0}{\sqrt{1 + \frac{z^2}{z_0^2}}} \exp\left[-\frac{k\rho^2}{2z_0(1 + \frac{z^2}{z_0^2})}\right] \cos\left[kz - \arctan\left(\frac{z}{z_0}\right) + \frac{k\rho^2}{2z\left(1 + \frac{z_0^2}{z^2}\right)}\right], \tag{2.61}$$

with the wave vector $k = \frac{\omega}{c}$. z_0 is the Rayleigh length, defined as

$$z_0 = \frac{1}{2}\sqrt{2bd - d^2}. \tag{2.62}$$

An important parameter is the beam width, $w(z)$, that depends on the position along the longitudinal resonator axis, z:

$$w(z) = w_0\sqrt{1 + \frac{z^2}{z_0^2}}. \tag{2.63}$$

Here, $w_0 = \sqrt{\frac{2cz_0}{\omega_{l,p,q}}}$ is the beam waist, i.e., the minimum width of the Gaussian-type beam in the center of the resonator. The maximum electric field, $E_{0,\max}$, can be found in a similar manner as for the closed-cavity situation explained in Section 2.8. According to References [123, 157], the solution for the special case of the $\mathrm{TEM}_{0,0,q}$ mode is:

$$E_{0,\max} = \sqrt{\frac{4P_{\mathrm{IN}}Q}{\pi\epsilon_0 c z_0 d}}. \tag{2.64}$$

This result shows similarities to the electric field strength in the closed resonators regarding the dependence on power and the quality factor (see Equation 2.55).

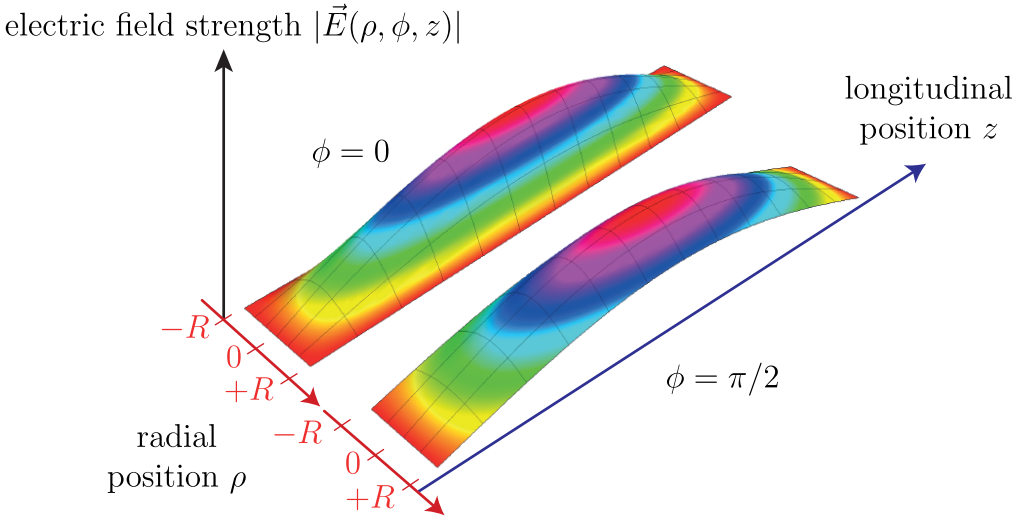

Figure 2.5: Electric field distribution, $\left|\vec{E}(\rho, \phi, z)\right|$, depending on the position in the (ρ, z)-plane with $\phi = 0$ (right) and $\phi = \pi/2$ (left) for the $TE_{1,1,1}$ mode(microwave lens). The linearly-polarized electric field of the $TE_{1,1,p}$ mode is not cylindrically symmetric.

2.10 Microwave resonators for motion control of ammonia molecules

As a first step towards motion control of polar molecules a microwave lens was developed. It is in direct analogy to electrostatic hexapole focusers for polar molecules in low-field-seeking states that became useful in a number of studies where state selection was important, see for example Reference [158]. A microwave lens provides focusing in transverse directions and leaves the longitudinal motion unchanged. The lens thus requires a transverse electric field gradient. The effect of such a field gradient on polar molecules is strongly quantum-state dependent. Molecules in so-called high-field-seeking states are attracted by local maxima of the electric field while molecules in low-field-seeking states are attracted by local field minima. In the study presented in this thesis, the main interest is the motion control of molecules in high-field-seeking states. Here, we use ammonia as a well-studied prototype molecule. All resonators are optimized such that their resonance frequencies are close to the so-called inversion transition of the rovibronic ground state of para-ammonia, $^{14}NH_3$, at 23.695 GHz. Then, strong AC-Stark shifts and thus strong forces occur. Exactly resonant radiation ($\nu = 23\,695$ MHz) needs to be avoided to prevent losses via dipole transitions. Therefore, the resonance frequency used for the manipulation experiments is blue detuned by approximately 50 MHz from the molecular transition (see also Sec. 3.4 for further details).

Stable manipulation for molecules in high-field-seeking states requires electric field maxima on the axis of the molecular beam. Among others, this condition is fulfilled by the $TE_{1,1,p}$ mode in a closed cylindrically symmetric resonator as well as the $TEM_{0,0,q}$ mode in an open Fabry–Pérot resonator. The two modes are the fundamental ones in the respective resonator types, offering strong electric fields because we optimized them to have small resonator volumes. The electric fields used for the microwave focusing

experiments are $TE_{1,1,p}$ modes, with $p = 2, 4$, in the closed, cylindrically symmetric resonator 1 and the $TE_{1,1,1}$ mode in the closed resonator 2 (see Section 2.5 for the details). 3D plots of the electric field of the $TE_{1,1,1}$ mode in such a closed resonator are shown in Figure 2.5. The electric field is not cylindrically symmetric, thus the fields are given in two perpendicular (ρ, z)-planes for $\phi = 0$ and $\phi = \pi/2$.

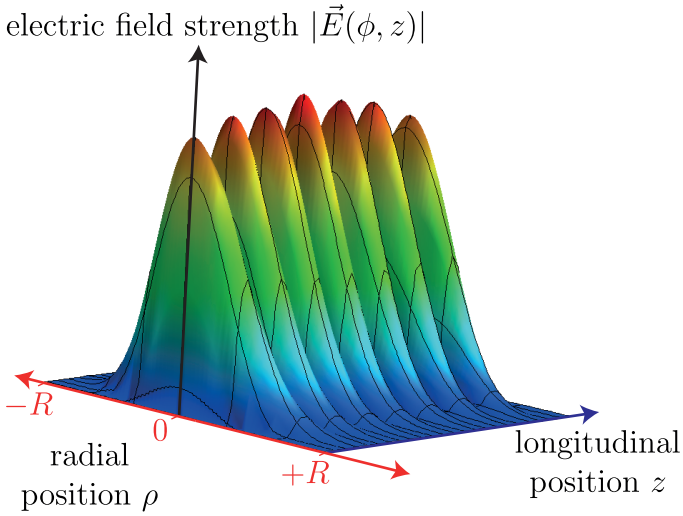

Figure 2.6: Electric field distribution, $|\vec{E}(\rho, z)|$, depending on the position in the (ρ, z)-plane of the $TEM_{0,0,6}$ mode in the open Fabry–Pérot resonator with spherical mirrors (microwave decelerator 1). Here, the linearly-polarized electric field of the $TEM_{0,0,q}$ mode is cylindrically symmetric.

In a first attempt on microwave deceleration, an open Fabry–Pérot resonator composed of two spherical mirrors of identical curvature and radius is used to alter the forward velocity of the molecules in the beam. The employed $TEM_{0,0,6}$ mode has seven electric field maxima along the symmetry axis of the resonator that coincides with the molecular beam axis, as shown in Figure 2.6. By switching the field on and off at the appropriate times, the forward kinetic energy of the molecules can be changed, allowing, in principle, for longitudinal focusing as well as deceleration and acceleration of polar molecules. On the downside, the beam width typically amounts to a few cm at resonance frequencies of 23.7 GHz, Equation 2.63, which results in lower transverse field gradients and thus worse transverse focusing, compared to the closed resonators.

To improve the performance, a second generation microwave decelerator was developed. The design was guided by the successful microwave lenses: This resonator is again a closed, cylindrical cavity optimized for the resonance frequency of the higher $TE_{1,1,12}$ mode. Figure 2.7 shows its electric field distribution, $|\vec{E}(\rho, \phi, z)|$, in the closed cylindrically symmetric microwave resonator 3. The 3D-plots show the absolute values of the electric field in the $(\phi = 0, z)$-plane (left) and the perpendicular $(\phi = \pi/2, z)$-plane (right).

From Figures 2.5 and 2.7 it becomes clear that the linearly-polarized electric field of the $TE_{1,1,p}$ mode is *not* cylindrically symmetric even though the resonator is. One of the consequences is that the microwave lens has a focusing ellipse rather than a focal point (see also Sec. 5.2).

Strong electric fields are required for a strong interaction with the molecules. As discussed, the field strength depends on the quality factor of the resonator that in turn depends on the conductivity of the resonator material (see Equations 2.43 and 2.55). Copper has a high conductivity of $\sigma = 59.6 \cdot 10^6\,\mathrm{S/m}$ at room temperature, only surpassed by silver with approximately $61 \cdot 10^6\,\mathrm{S/m}$. The microwave resonators designed

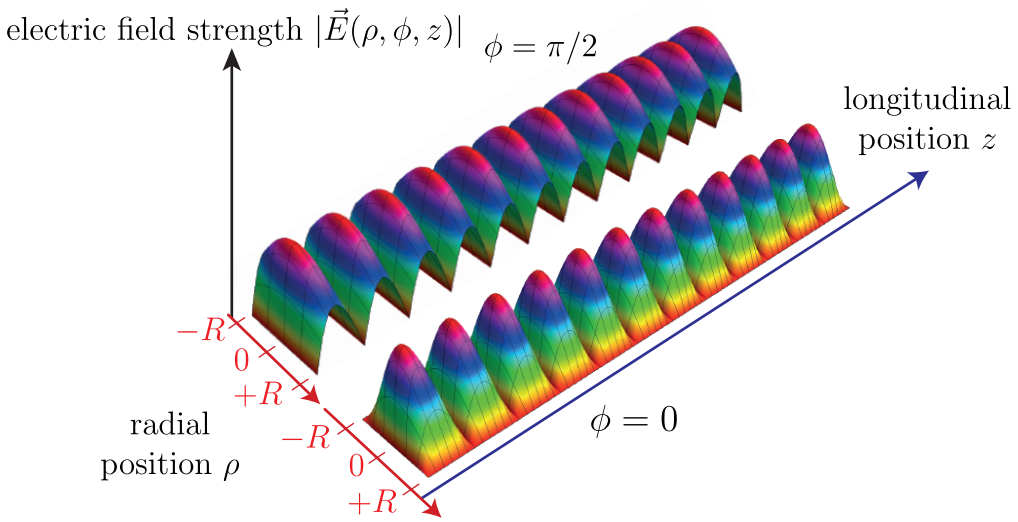

Figure 2.7: Electric field distribution, $|\vec{E}(\rho,\phi,z)|$, depending on the position in the (ρ,z)-plane with $\phi = \pi/2$ (top) and $\phi = 0$ (bottom) for the $TE_{1,1,12}$ mode (microwave decelerator 2).

and used throughout this thesis are mostly made of copper for obvious financial reasons. To achieve stronger electric fields, the closed resonator 3 was cooled to 77 K using liquid nitrogen.

2.11 Electrical conductivity and temperature

In general, the electrical conductivity of a metal increases with decreasing temperatures. A limiting process of the electrical conductivity in simple metals (such as copper) is the scattering of electrons off phonons. Cooling the metal freezes the phonons and thus the electrical conductivity increases. The dominating effect that limits the conductivity of such a metal at low temperatures is its purity: electrons scatter off the defects in the crystal structure. The purity can be expressed as the ratio of the electrical resistivity at room temperature and at cryogenic temperatures, the so-called residual resistivity ratio (RRR).

The Bloch–Grüneisen formula describes the temperature dependence of the electrical resistivity (in Ωm) of a metal. In a simple metal, like copper, only electron-phonon scattering is assumed and the Bloch–Grüneisen formula is [159]:

$$\rho(T) = \rho_0 + \frac{\mathrm{C}}{m \cdot \Theta}\left(\frac{T}{\Theta}\right)^5 \int_0^{\frac{\Theta}{T}} \frac{x^5 e^x}{\left(e^x - 1\right)^2} dx \tag{2.65}$$

Here, ρ_0 is the residual resistivity at absolute zero that can be expressed as the ratio of resistivity at room temperature and the residual resistivity ratio, $\rho_0 = \rho\left(T = RT\right)/RRR$. Θ is the so-called Debye temperature, a material's constant, so is the mass of the metal atoms, m. The constant C is required to set the resistivity of copper to $1.67 \cdot 10^{-8}\,\Omega$m at 0°C, hence, C is also material dependent. The constants required to calculate the

resistivity of copper are summarized in Table 2.2. Logarithmic plots of $\rho(T)$ in the temperature range from 1 to 400 K are shown in Figure 2.8 for the two residual resistivity ratios 10 and 100.

m	Θ	typical RRR	C	$\rho\,(T = 273.15\,K)$
63.5 u	343.5 K	10 to 700	$1.85 \cdot 10^{-3}$	$1.67 \cdot 10^{-8}\,\Omega$m

Table 2.2: Relevant constants for characterizing the temperature dependence of the electrical resistivity of bulk copper.

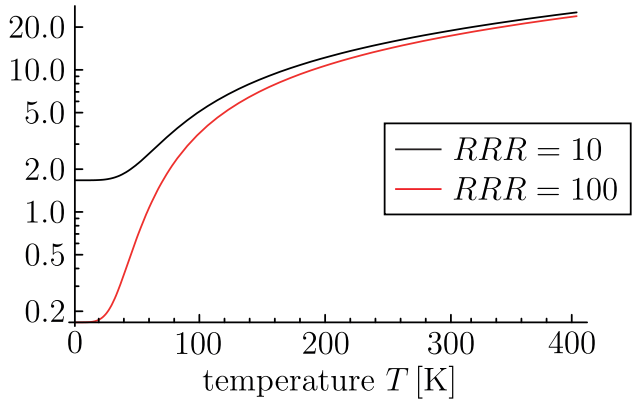

Figure 2.8: Plots of the electric resistivity in $10^{-9}\,\Omega$m of copper according to Equation 2.65 depending on the temperature ranging from 1 to 400 K.

A straightforward way to cool a resonator is based on evaporation cooling with liquid nitrogen. Temperatures down to 77 K can be reached. According to Reference [160], the conductivity of bulk copper should increase by a factor of approximately 8, which corresponds to an increase of the resonator's quality factor by $\sqrt{8} \approx 2.83$. However, the experimentally observed values for the microwave decelerator displayed in Table 4.1 in Chapter 4 only show an increase in the quality factor of about 1.8. From the Bloch–Grüneisen equation 2.65 it can be seen that the conductivity increase highly depends on the residual resistivity ratio (RRR), i.e., the defects in the material structure due to impurities. For normal copper (electrolytic tough pitch, ETP) the RRR is on the order of 10–100. To reach the increase in conductivity by a factor of 8, a RRR of 60 or more is necessary. To ensure a residual resistivity ratio higher than 60, highly pure oxygen-free copper (US: C10100, Germany: Kupfer OFE and purer alloys) should be used, since the typical values of the RRR easily exceed 100. Another issue that can limit the electrical conductivity of the copper resonators are surface defects inherent in the material or due to the machining process. Annealing can be a possibility to repair those.

The quality factors of the closed resonators described in this thesis are on the order of 3000 to 5500 at room temperature. The closed resonator 3 has a quality factor of approximately 9100 at 77 K which is an increase by a factor of 1.9 over its room temperature value. A plausible reason for this lower than expected increase in conductivity

is the resonator material. All resonators are made of ETP copper (electrolytic-tough-pitch) that is specified to be $> 99.9\%$ pure so that the RRR is not good enough for a maximum conductivity increase upon cooling.

Even lower temperatures and thus higher quality factors can be reached using liquid helium evaporation or closed cycle pulse-tube coolers that allow cooling to temperatures close to absolute zero. In this temperature domain many materials become superconducting, i.e., the resistivity of the material abruptly approaches zero and is no longer described by the Bloch–Grüneisen Equation 2.65.

The advantages of using superconducting materials for resonators are much higher quality factors on the order of 10^8 up to 10^{11}. Thus, large electric field strengths are possible with moderate input powers. In particle accelerator physics, this is often used for radio-frequency accelerator cavities that generate several hundreds of kV/cm of electric field strength at input powers on the order of kilowatts. Niobium is one of only three elemental type-II superconductors. These have the advantage of generally high critical temperatures and they are able to withstand much and higher critical magnetic fields. In the special case of niobium, the critical temperature, T_c, is at 9.2 K.

The breakdown of superconductivity is equivalent to the breakdown of the cooper pairs and happens when the superconductor gets warmer than the critical temperature ($T > T_c$). Furthermore, the magnetic fields that induce currents in the conductor can eventually quench the superconductivity. When using electromagnetic fields, the frequency is also important. Higher frequency photons carry more energy and thus are more likely to break the cooper pairs apart. This is reflected in the surface resistance according to BCS theory. At temperatures well below the critical temperature, a non-classical contribution in the resistance depends on the square of the frequency ($R_S(\mathrm{BCS}) \propto \omega^2$).

An example for high-performance superconducting radio-frequency cavities are the resonators used in the linear electron accelerator of the European XFEL (X-ray free-electron laser) currently built in Hamburg. Maximum electric fields of 20 to 40 MV/m (200 to 400 kV/cm) can be reached with unloaded quality factors of 1 to $2 \cdot 10^{10}$. During operation, these cavities are cooled to 2 K and the resonance frequency is about 1.3 GHz [161]. These electric fields are on the same order of magnitude as those applied in Stark decelerators. However, aside from a sizable investment, the frequency dependence (see above) is an issue. The resistance of the superconductor depends on the square of the frequency to a good approximation, thus it dramatically increases when using microwave frequencies on the order of 15 to 25 GHz appropriate for the manipulation of small and medium-sized polar molecules. Hence, the advantage of superconducting cavities at these frequencies is much smaller than might be expected.

3 Ammonia

Ammonia is a light and polar molecule. Its main isotopologue $^{14}NH_3$ has a mass of 17 u (1 u= $1.66{\cdot}10^{-27}$ kg) and a permanent dipole moment of 1.47 Debye ($4.9{\cdot}10^{-33}$ Cm). It is required at the beginning of the synthesis of almost every substance containing nitrogen atoms and as such inextricably linked to modern industrialized agriculture via fertilizers. So far, two Nobel Prizes were awarded to research related to ammonia. In 1918, Fritz Haber was awarded the Nobel Prize in Chemistry for the synthesis of ammonia from H_2 and N_2 using the famous Haber–Bosch procedure. In 1964, Charles Townes received half of the shared Nobel Prize in Physics for his work on the MASER, the first of which was realized by population inversion in the inversion-split rovibronic ground state of para-ammonia, see also Chapter 1.

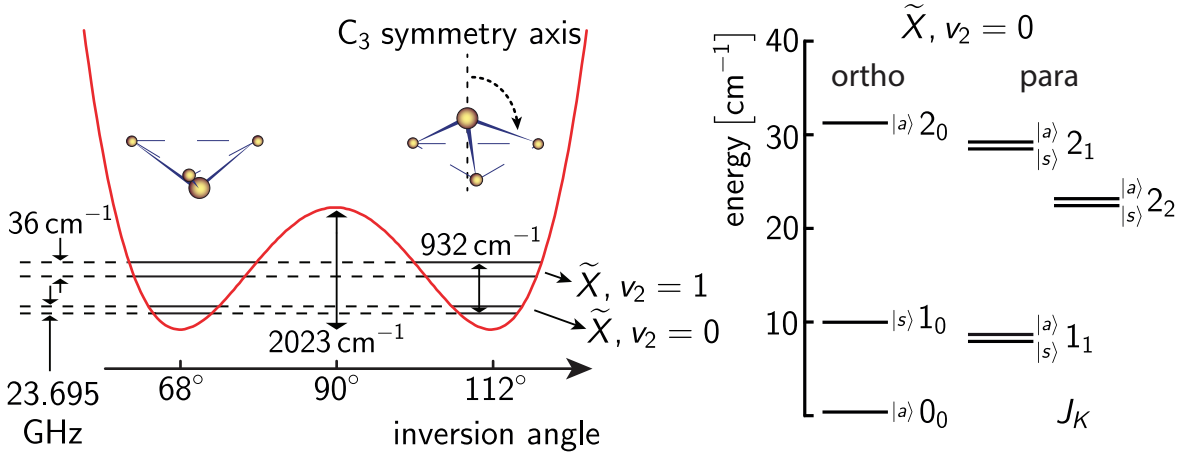

Figure 3.1: Double-minimum potential of ammonia ($^{14}NH_3$) depending on the inversion angle, i.e., the angle of the N–H bonds with the C_3 symmetry axis of the molecule. The two potential minima correspond to the configurations displayed on top of the potential wells. The first two vibrational levels of the large-amplitude inversion motion, $v_2 = 0, 1$, of para-ammonia in their rotational ground states $|J, K\rangle = |1, 1\rangle$ are indicated. These states are inversion split into a symmetric and an antisymmetric level. The plot on the right side of the figure shows the energy-level structure of the energetically lowest rovibronic states in $^{14}NH_3$.

The ammonia molecule is shaped like a regular pyramid with the nitrogen atom at the apex and the three hydrogen atoms at the base plane. The pyramidal structure can be realized with the nitrogen on either side of the hydrogen-atom plane. This is expressed in the double-well potential of ammonia depending on the angle of the N–H bonds with the C_3 symmetry axis, as shown in Figure 3.1. The barrier between the two minima is 2023 cm^{-1}. At higher vibrational energies the ammonia molecule is no longer

rigid and can change its umbrella configuration. This is the so-called inversion motion and its corresponding vibrational mode is denoted v_2. The barrier is of finite height, which means the hydrogen atoms can tunnel through the plane containing the nitrogen atom even at lower energies. Consequently, all states with energies smaller than the barrier height split into two states that can be described by linear combinations of the wave functions for the left, ϕ_L, and the right, ϕ_R, potential well: $1/\sqrt{2}(\phi_L + \phi_R)$ and $1/\sqrt{2}(\phi_L - \phi_R)$. These two linear combinations differ in parity, the sum is symmetric, s, and the difference is antisymmetric, a.

In order to satisfy the Pauli exclusion principle, the total wavefunction has to be antisymmetric under exchange of two fermions. The nuclear spins of the three protons ($I = 1/2$) and the nuclear spin of the ^{14}N nucleus ($I = 1$) can couple to states with A_1-symmetry (totally symmetric or *ortho*) and E-symmetry (antisymmetric or *para*), according to the C_{3v} point group. Therefore only certain combinations of rotational wave functions with nuclear spin wave functions are possible. This is indicated on the right side of Figure 3.1.

The quantum state of ammonia used in the microwave motion-manipulation experiments is the $|J, K\rangle = |1, 1\rangle$ rotational state in the vibronic ground state $(\tilde{X}, v_2 = 0)$, indicated in Figure 3.1. It is the ground state of para-ammonia, and its inversion splitting into two states with different symmetry amounts to $h \times 23.695\,\mathrm{GHz}$.

3.1 Rotation of a symmetric top

In the equilibrium structure all three N–H bonds are identical (C_{3v} point group), thus the ammonia molecule is an oblate symmetric rotor. In a symmetric top, at least two of the three moments of inertia are equal. The molecule is considered oblate if the equal moments of inertia, $I_a = I_b$, are smaller than the third one, I_c. In the case of ammonia, $^{14}NH_3$, I_c amounts to $4.4 \cdot 10^{-47}\,\mathrm{kgm}^2$ and I_a is approximately $2.8 \cdot 10^{-47}\,\mathrm{kgm}^2$. The Hamilton operator, $\hat{H}_0$, of an oblate symmetric top, neglecting all degrees of freedom except the rotation, has the following form [162]:

$$\hat{H}_0 = B\hat{J}^2 + (C - B)\,\hat{J}_z^{\,2}. \tag{3.1}$$

B and C are the rotational constants that depend on the molecule's moments of inertia ($A = B = \frac{h}{8\pi^2 c I_b}$ and $C = \frac{h}{8\pi^2 c I_c}$) which amount to $B = 10\,\mathrm{cm}^{-1}$ and $C = 6.3\,\mathrm{cm}^{-1}$. $\hat{J}$ is the total angular momentum operator and $\hat{J}_z$ its projection onto the molecule's C_3-symmetry axis, $\vec{z}$. The energies of the rotational states, W_{rot}, depend on the eigenvalues $J = 0, 1, 2, \ldots$ and $K = -J, \ldots, 0, \ldots, +J$ of the operators $\hat{J}$ and $\hat{J}_z$ and take the following form:

$$W_{rot} = BJ(J + 1) + (C - B)\,K^2. \tag{3.2}$$

The quantum numbers J and K have already been used to identify the para-ammonia ground state in previous parts of this thesis. The lowest lying rotational levels are shown on the right of Figure 3.1. The selection rules for dipole transitions in a symmetric top are $J = J' \pm 1$ if the symmetry is conserved and $J = J'$ if levels of different symmetry are coupled. Hence, the next accessible rotational level from the $|J, K\rangle = |1, 1\rangle$ state is the $|J, K\rangle = |2, 1\rangle$ state. The energy difference is approximately $20\,\mathrm{cm}^{-1}$

or $h \times 600\,\mathrm{GHz}$ (see Fig. 3.1), which is far larger than the inversion splitting of the ground state. Consequently, the $|J, K\rangle = |1, 1\rangle$ inversion doublet is considered to be an isolated two-level system to a good approximation. The different symmetries of the two inversion components of the para-ammonia ground state make it a good candidate for the manipulation with electric fields as described in Section 3.3 on the Stark effect. The inversion transition frequency of 23.695 GHz falls into the microwave domain, $\lambda \approx 12.7\,\mathrm{mm}$, K-band (18–26.5 GHz), so that ammonia is well suited for experiments with microwave radiation close to 23.7 GHz.

3.2 Supersonic expansion of ammonia

Ammonia is a gas at room temperature ($\sim 300\,\mathrm{K}$) and atmospheric pressures. Under these conditions many rotational and vibrational modes are excited. The Boltzmann distribution

$$p(\mathrm{QS}) \propto e^{-\frac{E_{\mathrm{QS}}}{k_B T}} \tag{3.3}$$

gives the probability p of finding a particle in a quantum state QS with the corresponding energy eigenvalue E_{QS} in a sample at thermal equilibrium and temperature T. The Boltzmann constant amounts to $k_B = 1.38 \cdot 10^{-23}\mathrm{JK}^{-1}$.

In ammonia, the energy difference between rotational levels is on the order of cm^{-1}. The vibrational splitting is on the order of 100 to $1000\,\mathrm{cm}^{-1}$. Considering the thermal energy $k_B T$ of approximately $200\,\mathrm{cm}^{-1}$ at room temperature, many rotational states and even some vibrational states will be populated with significant fractions. Thus, cooling is required to obtain a large number of molecules in the desired para-ammonia ground state, $|\tilde{X}, v_2 = 0\rangle\,|J, K = 1, 1\rangle$.

Packets of translationally and internally cold ammonia molecules are produced by supersonically expanding the molecules from a high-pressure container through a pulsed valve. This method is also described in Section 1.4.1 and depicted in Figure 1.5 with the typical velocity distribution for a pure sample of ammonia molecules in the room temperature cell and the supersonic beam.

For the experiments described in this thesis, about 0.35 bar of ammonia (mass 17 u) are mixed with 1.65 bar of the seed gas xenon (mass 131.29 u) in the gas reservoir that is cooled to $-70°\mathrm{C}$. The cooling lowers the thermal energy in the reservoir by approximately 25%. Under these conditions, a pure xenon beam would have a mean forward velocity of approximately 280 m/s. Due to the large admixture of ammonia, however, the average weight of the particles in this expansion is on the order of 111 u, which is about 15% lighter than in a pure xenon beam so that the mean velocity of the supersonic beam is on the order of 300 m/s.

Cooling of the internal degrees of freedom is very efficient so that a large fraction of the molecules in the ammonia beam exclusively populates the $|J, K\rangle = |1, 1\rangle$ para-ammonia ground state. Therefore, the generation of seeded ammonia beams via supersonic expansion is a great starting point for sophisticated motion-manipulation experiments.

3.3 DC-Stark effect

Energy levels of atoms or molecules (Eq. 3.2) shift or split up under the influence of an external electric field, $\vec{E}$. This behavior is described by the Stark effect, named after the German physicist Johannes Stark who was awarded the Nobel Prize in Physics in 1919 partially for the discovery of spectral line splittings in electric fields.

One distinguishes the Stark effect in static electric (DC) fields and in electromagnetic (AC) fields. For polar molecules, Stark shifts arise from the interaction of the molecule's permanent dipole moment, $\vec{\mu}_{\text{perm.}}$, with an external electric field. This interaction can be described by an additional term in the Hamiltonian:

$$\hat{H} = \hat{H}_0 - \vec{\mu} \cdot \vec{E}. \tag{3.4}$$

Here, $\hat{H}_0$ is the unperturbed rotational Hamiltonian (Eq. 3.2) and $\hat{H}_{\text{Stark}} = -\vec{\mu} \cdot \vec{E}$ accounts for the perturbation due to the Stark effect. Ammonia is a symmetric top, thus it has only one permanent dipole moment component μ along its C_3-symmetry axis, $\vec{z}$. The component of the permanent dipole moment along the axis of the electric field, μ_E, can be calculated from the projection of the permanent dipole moment onto the C_3-symmetry axis, μ_K:

$$\mu_K = \mu \frac{K}{\sqrt{J(J+1)}} \text{ and}$$
$$\mu_E = \mu_K \frac{M}{\sqrt{J(J+1)}}.$$

As mentioned above, the inversion doublet in the $|J, K\rangle = |1, 1\rangle$ state can be assumed to be a two-level system to a good approximation. The first-order corrected energy levels can be calculated using perturbation theory, since the effect of the electric field is small:

$$W_{\text{Stark}} = W - \mu \frac{MK}{J(J+1)}. \tag{3.5}$$

This equation shows that a degenerate $|J, K\rangle$ state splits up into $(2J+1)$ M components in an external electric field. Depending on the sign of MK a state loses or gains potential (Stark-)energy with increasing electric field strength $E(\vec{r}) = |\vec{E}(\vec{r})|$. This behavior is essential to the manipulation of neutral, polar molecules with electric fields because it essentially results in a force, $\vec{F} = -\vec{\nabla} W_{\text{DC-Stark}}(E(\vec{r}))$, in an inhomogeneous electric field. Molecules in states with $MK < 0$ are attracted by electric-field minima and are thus referred to as low-field-seeking states. On the other hand, states with $MK > 0$ are attracted by local electric field maxima, so-called high-field-seeking states.

Second-order corrections yield Stark shifts that depend on the square of the electric field strength and are thus significantly weaker. A more detailed description of the DC-Stark effect including higher-order corrections can be found in References [163, 164]. A detailed analysis of ammonia in electric fields can be found in Reference [163, 165].

Figure 3.2 shows the energy shifts of the inversion doublet in the para-ammonia ground state of $^{14}NH_3$ and $^{14}ND_3$ in moderate static electric fields. The inversion splitting at zero field of deuterated ammonia is on the order of 1.5 GHz. This is due to the higher

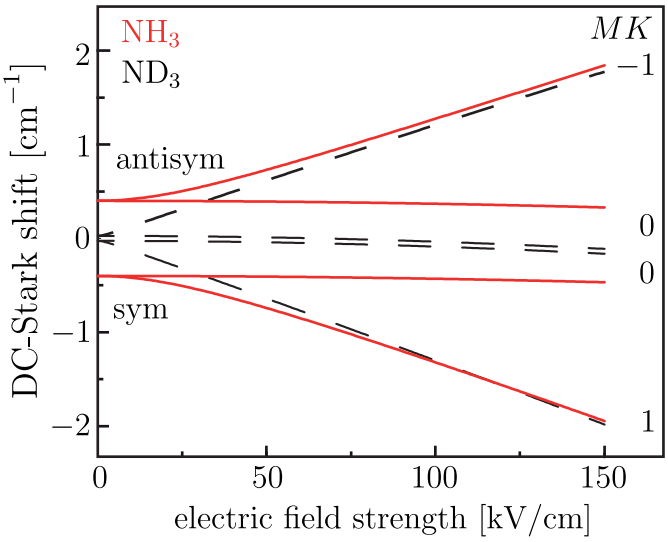

Figure 3.2: DC-Stark shifts for the two symmetric-top molecules $^{14}NH_3$ and $^{14}ND_3$ in the inversion-split $|J, K\rangle = |1, 1\rangle$ state of the vibronic ground state.

reduced mass if compared to regular ammonia, which slows down the tunneling rate, i.e., the tunneling splittings for states below this barrier are smaller. For both molecules, the inversion doublet splits up into four states in an external electric field.

The nuclear quadrupole coupling in principle couples the nuclear spin $\vec{I}$ of the nitrogen atom to the rotational angular momentum $\vec{J}$, resulting in the total angular momentum $\vec{F}_1$. For small electric field strength, these have to be explicitly considered as is discussed in Reference [97]. However, as can be seen from Figure 3.3 for $^{14}NH_3$ and $^{14}ND_3$, respectively, all nuclear-quadrupole-coupling components of a given rotational level split into two groups: states that experience a strong Stark shift or states with almost no significant Stark shift. These two classes closely follow the behavior of the $MK = 0$ and $MK = -1$ states displayed in Figure 3.2 in particular at the higher electric field strengths that are relevant for the present work. Consequently, the hyperfine splitting is omitted.

The two components of the inversion splitting have different symmetry, a vs. s, so that they can strongly interact with each other via an external electric field. States with different symmetries are mixed by the dipole operator and repel each other with increasing electric field strength. In order to find the first order Stark energy of the inversion doublet, the 2×2 matrix that accurately describes the Hamiltonian has to be solved.

$$H = \begin{pmatrix} \frac{W_{\text{inv}}}{2} & -\mu \frac{MK}{J(J+1)} E \\ -\mu \frac{MK}{J(J+1)} E & -\frac{W_{\text{inv}}}{2} \end{pmatrix}.$$

W_{inv} is the inversion splitting in zero electric field. The energy eigenvalues of the mixed states ϵ_i are found by diagonalizing H, i.e., solving the characteristic polynomial $\epsilon_i^2 - \text{tr}(H) \cdot \epsilon_i + \det(H) = 0$ in the case of a 2×2 matrix.

$$\epsilon_{1,2} = \pm \sqrt{\left(\frac{W_{\text{inv}}}{2}\right)^2 + \left(\mu E \frac{MK}{J\,(J+1)}\right)^2}.$$

The positive square root describes the energy of molecules in the low-field-seeking upper inversion-doublet component whereas the negative square root is valid for molecules

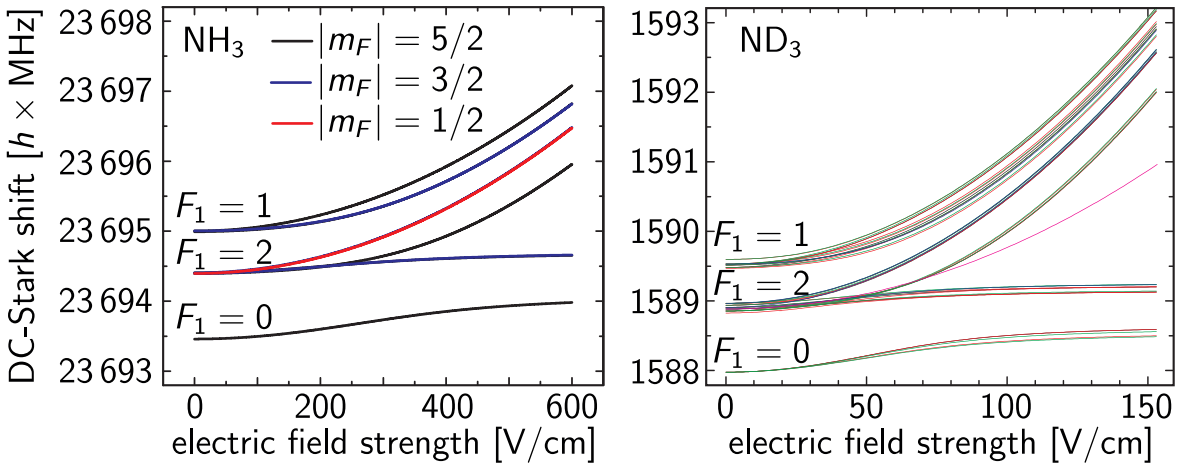

Figure 3.3: DC-Stark shifts of the upper inversion doublet component of the $|J, K\rangle = |1, 1\rangle$ state in the vibronic ground state of $^{14}NH_3$ (left panel) and $^{14}ND_3$ (right panel) in low electric fields. F_1 is the quantum number associated with the total angular momentum of rotation, $\vec{J}$, and the nuclear spin of the ^{14}N nucleus, $\vec{I}_N$ ($\vec{F}_1 = \vec{J} + \vec{I}_N$). The quantum number F also incorporates the additional coupling of the nuclear spin of the hydrogen/deuterium atoms, $\vec{I}_H/\vec{I}_D$, $\vec{F} = \vec{F}_1 + \vec{I}_{H/D}$. [97, 166, 167]

in the high-field-seeking lower inversion-doublet component. The bare DC-Stark shifts with respect to zero field for the upper and lower inversion doublet component are thus:

$$W^1_{\text{Stark,DC}} = \pm\sqrt{\left(\frac{W_{\text{inv}}}{2}\right)^2 + \left(\mu E \frac{MK}{J\,(J+1)}\right)^2} \mp \frac{W_{\text{inv}}}{2}. \tag{3.6}$$

At very weak electric fields, the Stark shift follows a quadratic behavior and becomes linear at stronger electric fields. In $^{14}NH_3$, this linearization occurs at about 50 kV/cm while the linearization for $^{14}ND_3$ starts already at a few kV/cm. This difference arises from the much smaller inversion splitting that is only 1.5 GHz in $^{14}ND_3$ due to the heavier deuterium atoms (see also Fig. 3.2).

Motion control of molecules in low-field-seeking states requires electric field minima, that can easily by realized using static-electric fields from electrode arrays, for instance in two dimensions (2D) in a hexapole focuser or a Stark decelerator and in 3D in ring-decelerators or molecule traps.

For molecules in high-field-seeking states, electric field maxima are required, which is incomparably more difficult because true 3D field maxima in free space cannot be generated from purely static fields alone. This is a direct consequence of Maxwell's equations and summarized by Earnshaw's theorem [67].

3.4 AC-Stark effect of ammonia

In the case of a polar molecule in an AC-electric field, for instance an electromagnetic wave, the Hamiltonian 3.4 is in principle still valid, however, the electric field is time-dependent. The straightforward approach is to solve the time-dependent Schrödinger

equation [168]

$$i\hbar\frac{\partial\psi}{\partial t} = \hat{H}_0\psi - \vec{E}\cdot\vec{\mu}\psi$$

with the electric field, $\vec{E}$, and the dipole moment operator of the molecules, $\vec{\mu}$. For a linearly polarized, monochromatic field, the field strength at a certain point in space can be expressed as:

$$E_x = \mathcal{E}\cdot\cos\omega t, \tag{3.7}$$

with the amplitude of the electric field $\mathcal{E}$. In the case of circular polarization one would find

$$\begin{aligned} E_x =& \frac{\mathcal{E}}{\sqrt{2}}\cdot\cos\omega t \text{ and} \\ E_y =& \frac{\mathcal{E}}{\sqrt{2}}\cdot\sin\omega t. \end{aligned}$$

For this discussion, it is assumed that the wave vector of the microwave radiation points in the z-direction. Thus, the dipole interaction can be rewritten as

$$-\vec{E}\cdot\vec{\mu} = -\frac{\mathcal{E}}{2}\left(\mu_z e^{-i\omega t} + \mu_z e^{i\omega t}\right) \tag{3.8}$$

for the linearly polarized electric field and

$$-\vec{E}\cdot\vec{\mu} = -\frac{\mathcal{E}}{2\sqrt{2}}\left[\left(\mu_x + i\mu_y\right)e^{i\omega t} + \left(\mu_x - i\mu_y\right)e^{-i\omega t}\right]$$

in the case of a circularly polarized microwave field. Then the time-dependent Schrödinger equation for the AC-Stark effect in the linearly polarized case is

$$i\hbar\frac{\partial\psi}{\partial t} = \hat{H}_0\psi - \frac{\mathcal{E}}{2}\left(\mu_z e^{-i\omega t} + \mu_z e^{i\omega t}\right)\psi.$$

The solution of the Schrödinger equation (Eq. 3.4) can be expanded into a Fourier series of $e^{im\omega t}$, because of the sinusoidal periodicity of 2π:

$$\psi = \sum_{m=-\infty}^{m=+\infty}\sum_n a_{n,m}e^{im\omega t - i\epsilon t/\hbar}\psi_n.$$

The ψ_n are the eigenfunctions of the field-free Hamiltonian $E_n\psi_n = \hat{H}_0\psi_n$ (see Eq. 3.2). m can be understood as the number of photons of frequency ω in the AC-electric field and $\epsilon = E_n + m\hbar\omega$ is the zero-order energy of the so-called dressed state, which will be explained below. The amplitudes $a_{m,n}$ read as

$$\epsilon\cdot a_{m,n} = \left(E_n + m\hbar\omega\right)a_{m,n} - \frac{1}{2}\mathcal{E}\left[\sum_{n'}\left(\mu_z\right)_{n,n'}a_{m-1,n'} + \sum\left(\mu_z\right)_{n,n'}a_{m+1,n'}\right].$$

This result is best understood in the dressed-state model that is frequently employed in the field of atomic physics to describe the interaction of atoms with laser fields. In

this respect, often the term light shift is used. In contrast to the Hamiltonian used so far to describe the interaction of the electric field with a polar molecule (Eq. 3.4), the dressed-state model considers the electric field not as a classical field, but as a quantized photon bath. The Hamiltonian $\mathcal{H}$ is thus written as

$$\mathcal{H} = H_0 + H_{\text{AC-Stark}} + H_{\text{EM}}. \tag{3.9}$$

The dressed-state model is a fully quantum mechanical description that includes the quantization of the electric field, according to $H_{\text{EM}} = \hbar\omega(\hat{a}^\dagger\hat{a} + 1/2)$. The Hamiltonian for the quantized electric fields incorporates the photon creation operator $\hat{a}^\dagger$ and the photon annihilation operator $\hat{a}$. The eigenvalues of the electromagnetic field are $E_m = (m + 1/2)\hbar\omega_0$ with the photon number m and the zero-point energy $\hbar\omega/2$.

The eigenfunctions of the total Hamiltonian $\mathcal{H}$ are the so-called dressed states. In zero-order approximation the quasi-energy levels of the dressed states are the sum of the field-free molecular energy level with the number of photons in the field, m, i.e. $\epsilon = E_n + m\hbar\omega$. The interaction matrix elements $-\frac{1}{2}\mathcal{E}\,(\mu_z)_{n,n'}$ couple the zero-order quasi-energy levels $E_{n'} + m'\hbar\omega$ and $E_n + m\hbar\omega$ with $\Delta m = \pm 1$. Further details on solving a Hamiltonian with a periodic potential can be found in References [169, 170]. The dressed-state model is addressed in greater detail in References [12, 171, 172], for example.

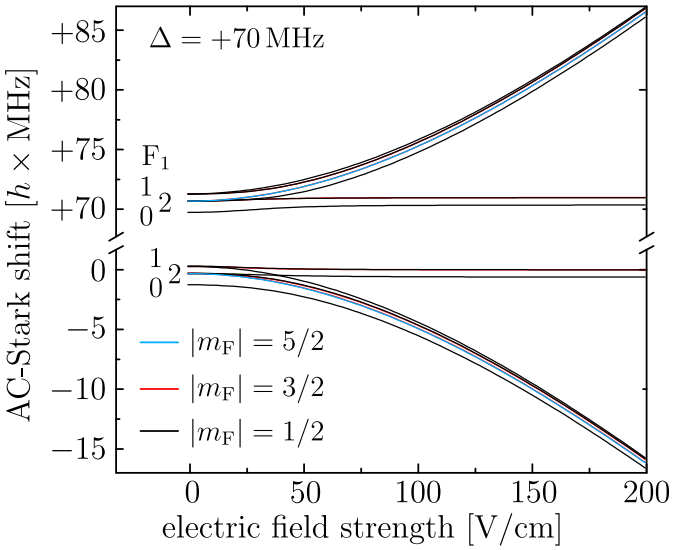

Figure 3.4: Hyperfine resolved AC-Stark shifts of the inversion doublet in the para-ammonia ($^{14}NH_3$) ground state ($|J, K\rangle = |1, 1\rangle$). The detuning is $\Delta = +70\,\text{MHz}$. F_1 is the quantum number associated with the angular momentum $\vec{F}_1 = \vec{J} + \vec{I}_N$. The $|m_F|$ are the projections of the total rotational angular momentum $\vec{F} = \vec{F}_1 + \vec{I}_H$ onto the electric field axis. [168]

In the case of ammonia, the $|J, K\rangle = |1, 1\rangle$ inversion doublet can be considered to be a two-level system due to the same consideration as mentioned in Section 3.3: the next rotational level with dipole-allowed transitions ($\Delta J = 1$ and $\Delta K = 0$), the $|J, K\rangle = |2, 1\rangle$ state is about 30 times the inversion splitting higher in energy, as indicated in Figure 3.1. The different hyperfine states due to the nuclear quadrupole coupling are shown in Figure 3.4. In the microwave resonators, electric field strengths up to 1.4 kV/cm can be achieved. There, the typical AC-Stark shifts are on the order of several hundred MHz, whereas the hyperfine splitting is about two orders of magnitude smaller. Hence, the hyperfine splitting can be neglected for the states and the electric field strengths relevant to this work.

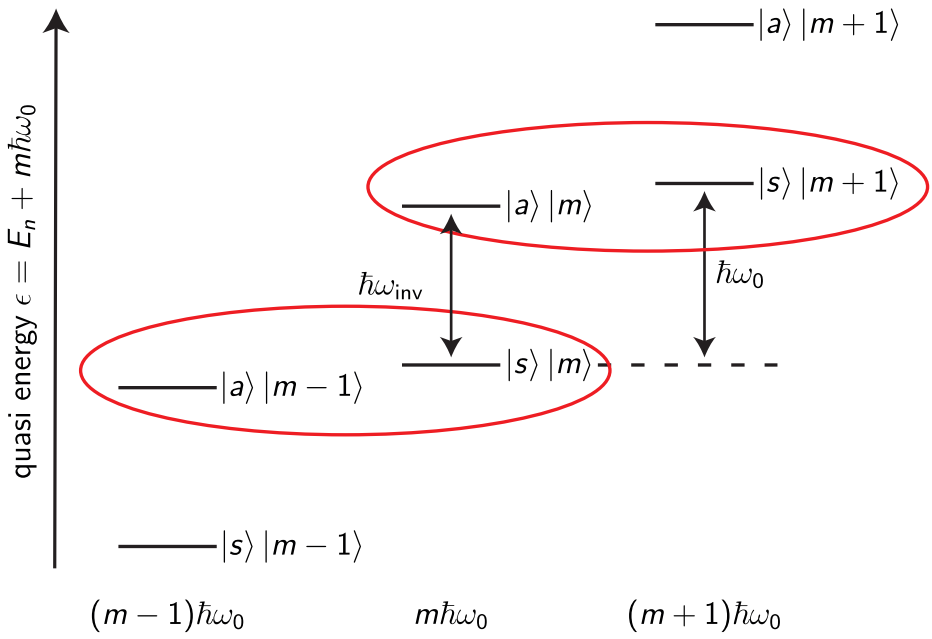

Figure 3.5: Dressed-state quasi-energy levels of ammonia ($^{14}NH_3$) molecules in the $|J,K\rangle = |1,1\rangle$ inversion doublet. The lower and upper components are labeled $|s\rangle$ (symmetric) and $|a\rangle$ (antisymmetric), respectively, according to their symmetry. The second ket contains the photon number of the dressed state. The AC-Stark interaction occurs between states with different symmetry and a difference in photon number by $\Delta m = 1$. The ellipses illustrate the states that are coupled by the microwave field. The interaction strength depends on the difference of the microwave frequency $\omega_0 = \omega_{\text{MW}}$ to the frequency associated with the inversion transition, i.e., the so-called detuning: $\Delta = (\omega_{\text{MW}} - \omega_{\text{inv}})/2\pi$.

The dressed-state picture for the $|J,K\rangle = |1,1\rangle$ inversion doublet in ammonia is visualized in Figure 3.5 as parallel ladders of bare molecule states. The ladders differ in photon number and are thus shifted in quasi-energy by $\hbar\omega_0$. The coupling occurs between states with different parity ($|s\rangle$ vs. $|a\rangle$) and a difference in photon number of $\Delta m = 1$, as indicated by the red ellipses.

Based on the concept of the dressed-state formalism and neglecting all other states except the inversion doublet, the Hamiltonian can be written as a 2×2 matrix

$$\mathcal{H} = \begin{pmatrix} h\Delta/2 & -\frac{\mu E}{2}\frac{MK}{J(J+1)} \\ -\frac{\mu E}{2}\frac{MK}{J(J+1)} & -h\Delta/2 \end{pmatrix}. \tag{3.10}$$

The solutions for the energy eigenvalues $\epsilon_{1,2}$ of this matrix can be obtained by solving the characteristic polynomial:

$$\epsilon_{1,2} = \pm\sqrt{\left(\frac{h\Delta}{2}\right)^2 + \left(\frac{\mu E}{2}\frac{MK}{J\,(J+1)}\right)^2}$$

and for the AC-Stark shifts for the upper and lower inversion-doublet component we

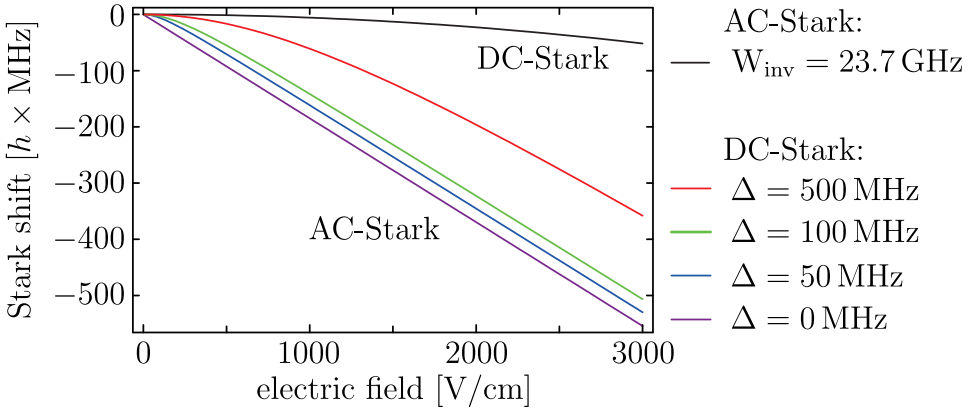

Figure 3.6: Comparison of the Stark shifts of the $|J, K\rangle = |1, 1\rangle$ para-ammonia ground state up to 3 kV/cm. The black trace shows the DC-Stark shift of the lower inversion-doublet component ($W_{\text{inv}} = 23\,695$ MHz) and the colored traces represent AC-Stark shifts of the upper inversion-doublet component with blue-detunings from $\Delta = 0$ to $+500$ MHz.

find:

$$W_{\text{AC-Stark}} = \pm\sqrt{\left(\frac{h\Delta}{2}\right)^2 + \left(\frac{\mu E}{2}\frac{MK}{J(J+1)}\right)^2} \mp \frac{h\Delta}{2}. \tag{3.11}$$

Comparing Equations 3.6 and 3.11, there are obvious differences between the AC- and the DC-Stark effect. At large electric fields, the AC-Stark shift is smaller than in the DC case due to the additional factor of ½ in the interaction term under the square root. This reduction arises from time-averaging of the AC-electric field. The detuning Δ, i.e., the difference between the inversion frequency and the frequency of the electromagnetic field $\Delta = \nu_{\text{MW}} - \nu_{\text{inv}}$, replaces the inversion splitting in the DC case. The detuning is not a fixed molecular property, hence two additional parameters arise if AC-electric fields are used to manipulate the motion of polar molecules. The first parameter is the magnitude of the detuning: A small detuning brings about a strong, that is linear, AC-Stark shift at already weak electric fields. This behavior is displayed in Figure 3.6 where the DC-Stark shift of the upper inversion-doublet component of the para-ammonia ground state is compared to AC-Stark shifts with blue detunings ranging from 0 to $+500$ MHz of the same state. In an experiment $\Delta = 0$ should be avoided, i.e., microwave radiation on resonance with the inversion transition ($\nu_{\text{MW}} = \nu_{\text{inv}}$), because it causes undesired transitions.

The second important parameter is the sign of the detuning: both red- ($\Delta < 0$) and blue-detunings ($\Delta > 0$) are possible. In Figure 3.7, the AC-Stark shifts for the ammonia $|J, K\rangle = |1, 1\rangle$ inversion doublet are shown for both cases in electric fields up to 0.75 kV/cm. In the red-detuned case (left side of Fig. 3.7, $\Delta = -50$ MHz), the upper (lower) inversion-doublet component has a positive (negative) AC-Stark shift. This situation is similar to the DC case, the AC-Stark shift is just stronger at weak electric fields because of the small detuning. In the blue-detuned case on the right side ($\Delta = +50$ MHz), however, the $|1, 1, s\rangle\,|m+1\rangle$ state is higher in quasi-energy than the $|1, 1, a\rangle\,|m\rangle$ state. Consequently, the signs of the AC-Stark shifts of the inversion-doublet

components reverse and the upper (lower) component has a negative (positive) AC-Stark shift. Consequently, ammonia molecules in the upper inversion doublet component that are always DC-low-field seeking can be made AC-high-field-seeking by applying a blue detuned microwave field.

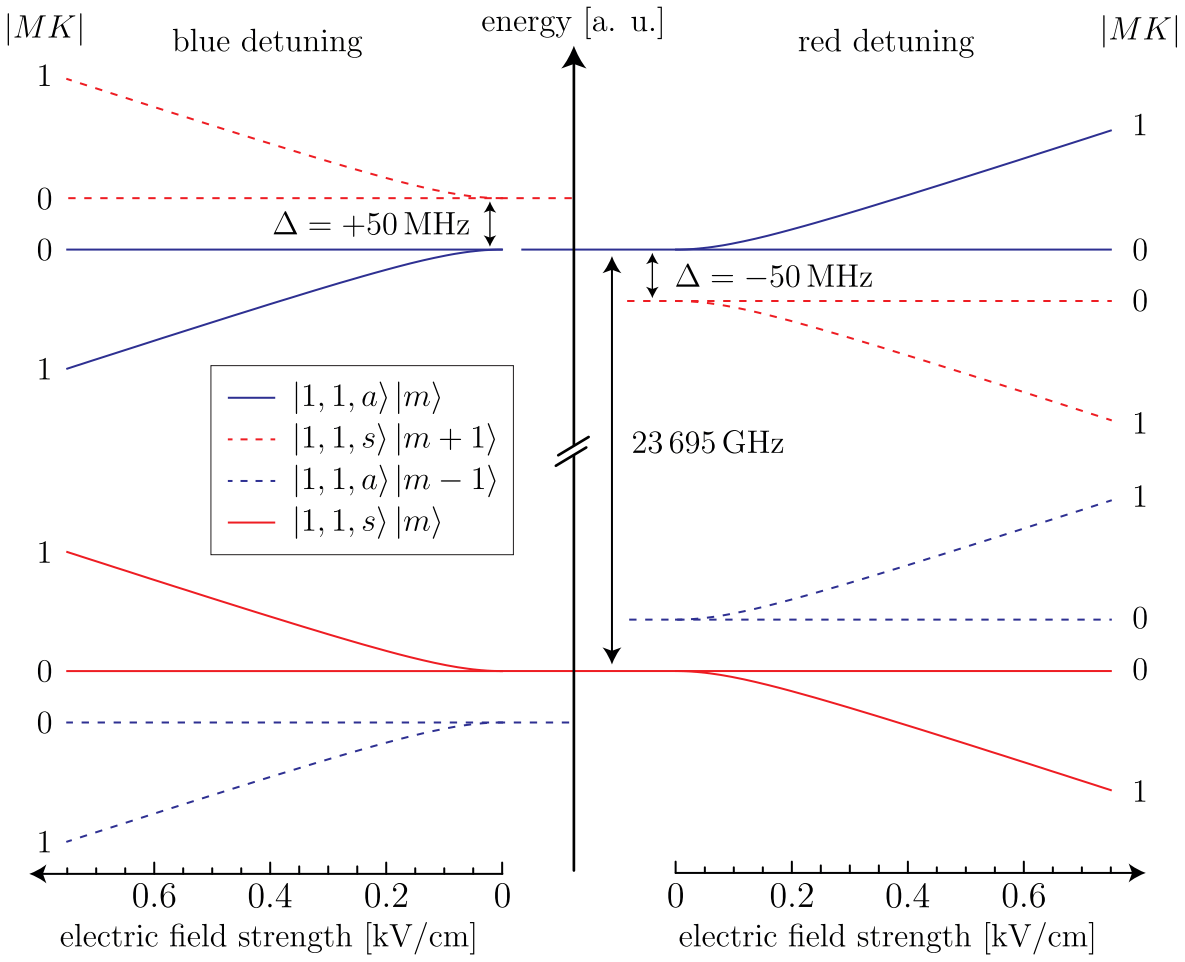

Figure 3.7: Plots of AC-Stark shifts for the ammonia $|J, K\rangle = |1, 1\rangle$ inversion doublet in a red-detuned (left) and a blue-detuned (right) microwave field. The magnitude of the detuning is 50 MHz in both cases. The AC-Stark shifts of the $|MK| = 1$ states become linear at approximately 0.15 kV/cm. The straight traces are dressed with m photons, the dashed red traces are dressed with $m + 1$ photons and the dashed blue traces with $m - 1$ photons.

A similar approach to calculate the AC-Stark shifts in the zero-order approximation of the medium-sized molecule 4-aminobenzonitrile (4ABN) is presented in Chapter 6. These larger molecules are particularly challenging since their rotational level structure is much denser and more complex and the molecule can no longer be approximated as a two-level system interacting with microwave radiation. Consequently, the dressed-state model has to be extended to the many-level case.

4 Experimental setup

In this chapter, an overview of the experimental details is given. These details include the experimental setup that is covered in Section 4.1 and 4.2, but also the coupling into the microwave resonators in Section 4.4, details of the detection process in Section 4.5 and the implementation of the switching sequences required for longitudinal motion control in Section 4.7.

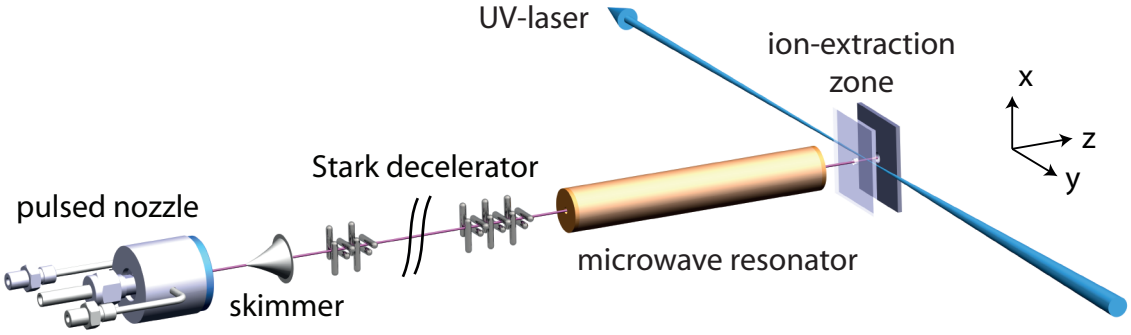

Figure 4.1: Schematic of the experimental setup with a closed resonator.

Figures 4.1 and 4.2 show schematics of the molecular beam apparatuses (not to scale) with the closed and the open resonator, respectively. Both are housed in a differentially pumped vacuum chamber. The molecular beam (see also Sec. 3.2) is produced by expanding a mixture of approximately 0.35 bar ammonia in 1.65 bar xenon into the source chamber through a modified General Valve Series 9 (Parker) cooled to -70°C. The nozzle opening is 0.8 mm in diameter, and a skimmer with a 1.5 mm aperture, about 35 mm downstream from the nozzle, separates the source chamber from the decelerator and detection chamber. The skimmer pre-selects molecules with small transverse velocity components and also serves for differential pumping. Turbo-molecular pumps, TMU 1001 and TMU 501, from Pfeiffer Vacuum backed by a single diaphragm pump ensure the operating pressure under gas load of 2 to $6 \cdot 10^{-6}$ mbar in the source chamber and 2 to $4{\cdot}10^{-8}$ mbar in the differentially pumped detection region.

Due to the cooling of the valve the mean initial velocity of the ammonia beam is about 280 m/s, and a large fraction of the molecules populates the inversion-split para-ammonia ground state. In the decelerator chamber, a 60 mm long hexapole that consists of 3 mm diameter electrodes (not shown in Fig. 4.1) focuses the ammonia molecules in the upper inversion-doublet component into the 94-stage Stark decelerator. The Stark decelerator is made of 3 mm diameter electrode pairs. The electrode spacing within the pairs is 2 mm, while the pair-to-pair spacing is 2.5 mm. Further details of the Stark-decelerator setup can be found in Reference [73].

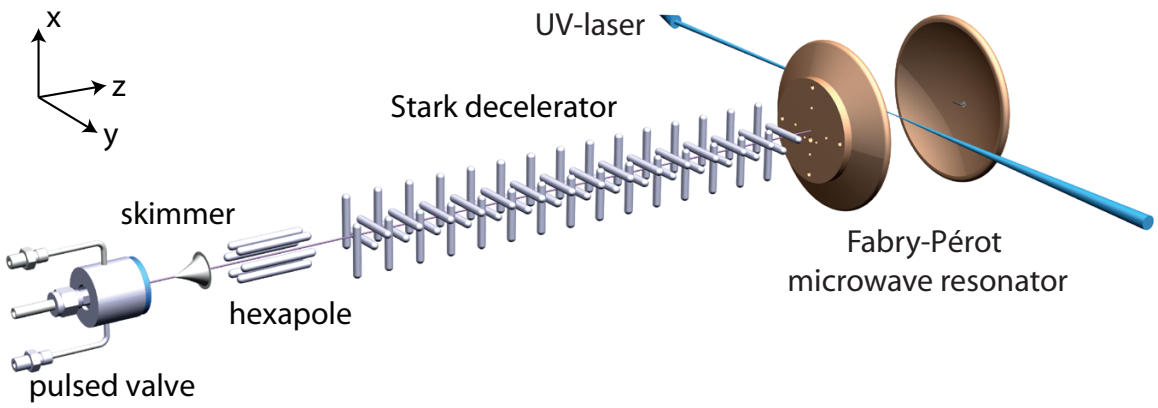

Figure 4.2: Schematic of the experimental setup with the open resonator. The TOF-MS electrodes are not indicated but they are shown in Figure 4.11.

The cylindrically symmetric microwave resonators (see Fig. 4.1) are located 4 mm behind the Stark decelerator. They are arranged such that the resonator axis coincides with the molecular beam axis. In total, four different resonators have been used throughout the experiments described in this thesis (further details are displayed in Sec. 4.2). The three closed copper resonators are about 120 mm long. The closed resonator 1 is a microwave lens supporting the $TE_{1,1,2}$ and the $TE_{1,1,4}$ mode. The closed resonator 2 was designed for focusing experiments with the $TE_{1,1,1}$ mode and the closed resonator 3 is a microwave decelerator, that employs the $TE_{1,1,12}$ mode. The molecules are detected about 5 mm behind the microwave resonator by photo-resonant ionization (details are given in Section 4.5) and detection of the parent ion with a multi-channel plate (-1.9 to -2.1 kV) in a compact time-of-flight mass spectrometer (TOF-MS). A photograph of the on-axis repeller ($+1.9$ kV) and extractor ($+0.5$ kV) plates, that are spaced by approximately 5.5 mm, is shown in Figure 4.4. Both plates have central apertures covered by a fine nickel mesh with a very high transmission. An additional flight tube (-1.5 to -2.1 kV) completes a Wiley-McLaren type configuration [173].

In the experimental setup with the open resonator (see Fig. 4.2), the gap between the Stark decelerator and the first mirror is 3.5 mm. A 3 mm diameter aperture in the center of the first mirror leaves enough space for the ammonia molecules to fly into the resonator. The mirrors have a radius of curvature of 100 mm and a diameter of 70 mm. They are made from a copper tungsten mixture (at the Stark decelerator side) and the rear mirror is made from copper (CU-ETP) and have a thickness of 3.5 mm in the center. The spacing between the mirrors, the resonator length, is approximately 46.2 mm to support the $TEM_{0,0,6}$ mode at 23.774 GHz and thus close to resonance with the inversion transition in ammonia. In this setup, the molecules are ionized close to the center of the resonator, about 26 mm downstream from the Stark decelerator. The ions are extracted vertically by a 80 mm spaced TOF electrode pair centered with respect to the resonator axis. These electrodes are not shown in Figure 4.2 but can be seen in the photograph of the open resonator in Figure 4.11. As a consequence of this setup, stable ion trajectories are limited to the resonator center. The voltage across the two TOF electrodes is typically on the order of 700 V.

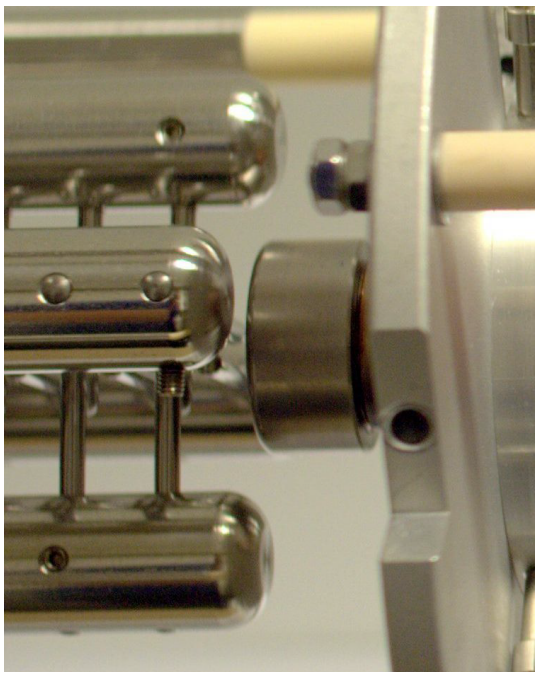

Figure 4.3: Photograph showing the 4 mm gap between the final electrode pair of the Stark decelerator and the front cap of the microwave resonator.

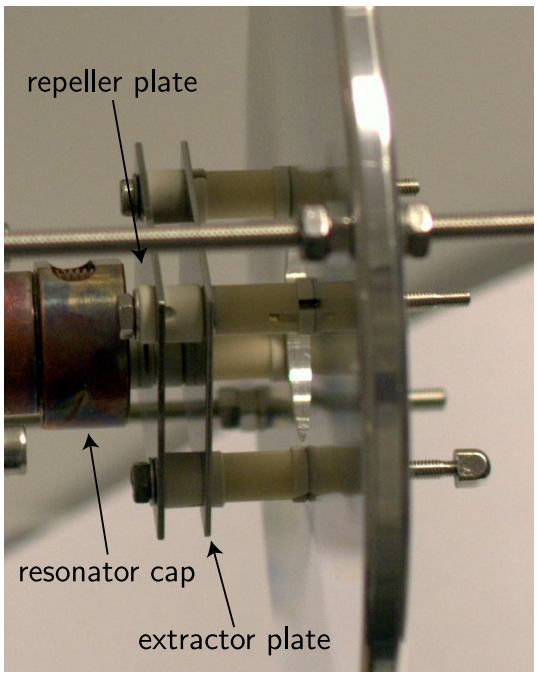

Figure 4.4: Photograph of the detection zone directly behind the microwave resonator. The gap between the rear cap and the repeller plate of the TOF-MS is approximately 3 mm.

4.1 The Stark decelerator

The energy levels of a polar molecule shift in a DC-electric field depending on the electric field strength. Figure 3.2 shows this behavior for the $|J, K\rangle = |1, 1\rangle$ inversion doublet of ammonia and deuterated ammonia. Here, the DC-Stark effect splits the inversion doublet into four components of which two are mixed such that they repel each other with increasing electric field ($MK < 0$ vs. $MK > 0$). These energy shifts, $W_{\text{DC-Stark}}$, give rise to a force in an inhomogeneous electric field proportional to $-\nabla W_{\text{DC-Stark}}$, driving the molecule towards regions with stronger fields (DC-high-field-seeking state) or weaker fields (DC-low-field-seeking state) depending on their quantum state.

The Stark decelerator, first demonstrated in 1999 [71, 174], is an electrode array that employs inhomogeneous DC-electric fields to manipulate the forward motion of internally cold, polar molecules from a molecular jet. The first molecule to be decelerated was CO in the metastable $a^3\Pi$ state [71]. Since then, Stark deceleration was used to slow down an impressive number of molecular species: ND_3 [72, 73], NH_3 [74], OH [75–79], metastable NH ($a^1\Delta$) [80, 81], OD [82], H_2CO [83], SO_2 [84], LiH [85], CaF [86], YbF [87], SrF [88] and NO [89].

Figure 4.5 is a photograph of the Stark decelerator used in the microwave manipulation experiments. It consists of 95 pairs of parallel electrodes (3 mm diameter, 2 mm gap). Adjacent electrode pairs (pair-to-pair distance 2.5 mm) are rotated by 90° with respect to each other. Every second pair of electrodes is set to high voltage (±10 kV) and the

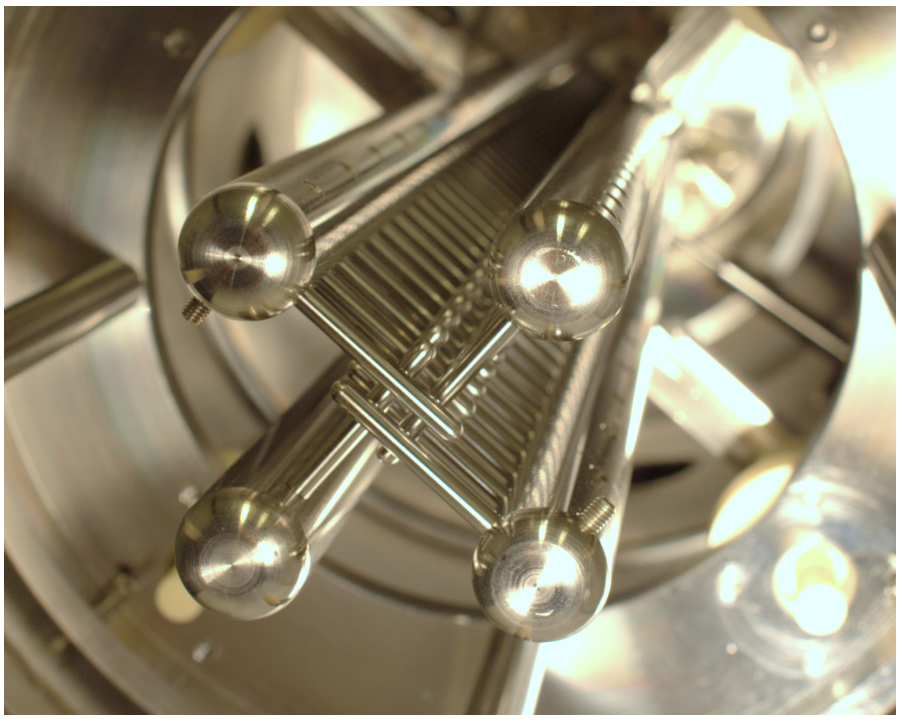

Figure 4.5: Photograph of the 52 cm long, 94-stage Stark decelerator in the vacuum chamber. The point of view is from the back of the Stark decelerator. The steel electrodes have a diameter of 3 mm. The gap within the parallel pairs is 2 mm. The pathway of the molecules points right through the center of the square formed by the adjacent electrode pairs.

next-neighboring pairs are kept at ground. During operation, two different settings are used: either the electrode pairs with even numbers are at high voltages while the odd ones are grounded or the voltages are interchanged. A schematic of the two different settings is depicted in Figure 4.6. A molecule in a low-field-seeking state traveling along the axis of the Stark decelerator will experience a potential hill when approaching a pair of high-voltage electrodes. In order to climb this hill, kinetic energy from the forward motion will be converted into DC-Stark (potential) energy. If the molecule is undisturbed and has enough kinetic energy to reach the top of the potential, the DC-Stark energy is reconverted to kinetic energy as it moves out of the electric field maximum. However, if the voltages are switched rapidly into the second configuration close to the peak of the potential hill, then the kinetic energy cannot be regained and the molecule is decelerated. This process is repeated in every stage, i.e., in total 94 times.

The supersonic expansion of ammonia seeded in xenon from a pulsed nozzle produces a large packet of molecules with a given spatial and velocity distribution (phase space). Hence, a fictitious so-called synchronous molecule is defined. It travels at exactly the velocity that is supposed to be manipulated. The switching occurs when this synchronous molecule is at the position z in a particular stage defined by the phase angle φ according to: $z(\varphi) = \varphi \cdot L/180°$. Then the synchronous molecule and also the molecular packet around it experience accelerations for phase angles smaller than zero, decelerations for

$\varphi > 0$ and the case of zero phase angle is referred to as guiding (see also Fig. 4.6).

In the guiding mode, the mean velocity of a packet of molecules is not changed because the switching occurs when the synchronous molecule is right in-between the high-voltage electrode pair and the grounded electrode pair. The Stark shifts of the two field configurations are equal at this position. The concept of phase angles will be addressed again for the switching sequences of the microwave decelerator (Sec. 4.7).

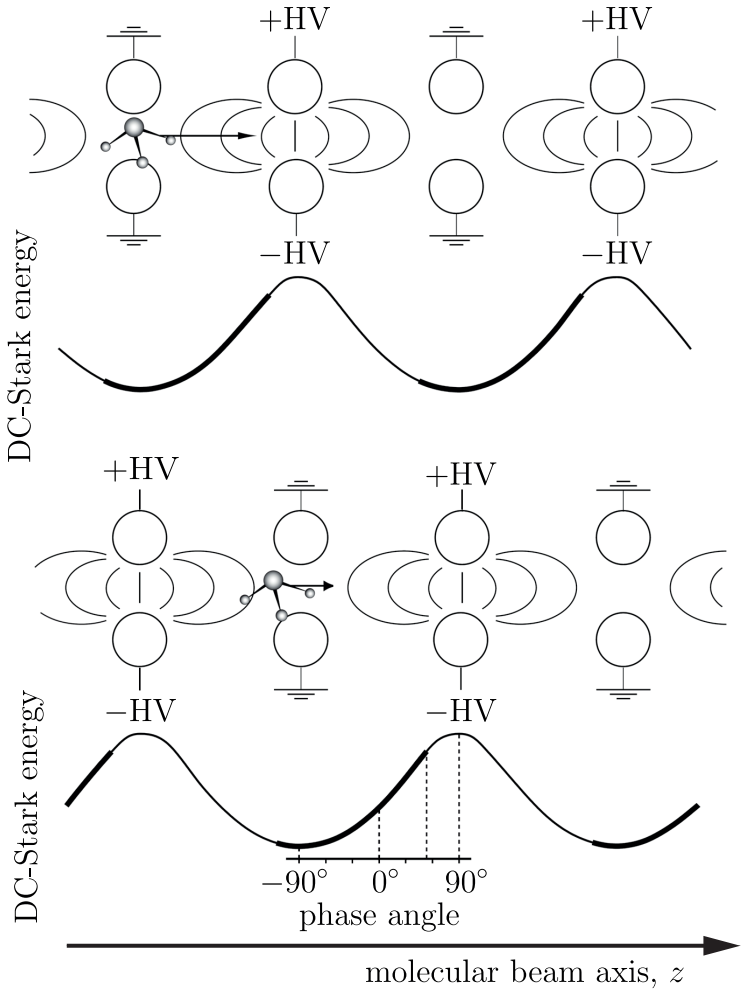

Figure 4.6: Schematic of the working principle of a Stark decelerator: every second electrode pair is set to high voltage whereas the next neighboring pairs are grounded. In a second configuration the voltages are exchanged ($\pm$HV $\leftrightarrow$ ground). By switching between the two configurations at the appropriate times, kinetic energy from the forward motion will be converted into DC-Stark energy or vice versa. Thus, with apt switching times given by the phase angle, φ, the molecules can be accelerated ($\varphi < 0$), guided ($\varphi = 0$) or decelerated ($\varphi > 0$).

4.1.1 Phase stability

Manipulating the motion of molecular packets with periodic electric field structures as generated by a Stark- or a microwave decelerator requires that the packet of molecules is kept together throughout the acceleration, guiding or deceleration process, both in real space and in momentum space. In the transverse directions, this is straightforward because the electric field is designed to be transversally focusing. In the longitudinal direction, the situation is more complex because the moving molecules experience different accelerations or deceleration with respect to the synchronous molecule depending on their relative longitudinal positions, see also Figure 4.6.

For keeping a packet of molecules together in the longitudinal direction, the so-called phase stability is important. In guiding mode this can easily be understood by the following example: Molecules initially faster than the synchronous molecule are slightly ahead while slower ones lag behind the synchronous molecule. The synchronous molecule travels at the constant phase angle $\varphi_0 = 0$, and experiences no net change in kinetic energy, while the molecules ahead experience a larger relative phase $\varphi > 0$ and the molecules that lag behind a smaller relative phase $\varphi < 0$. Due to the shape of the potential, positive phase angles smaller than $+90°$ experience net decelerations and negative phases larger than $-90°$ experience net accelerations. In the longitudinal (z,v_z)-phase space, this collective motion can be described as a clockwise rotation of the packet of molecules around the synchronous molecule. As a consequence the packet is stabilized against imperfections, for instance, from stage-to-stage variations of the electric field. A more detailed description of phase-space stability and phase-space motions can be found in Reference [175].

In the Stark decelerator, transverse focusing occurs in only one direction per stage. For instance for the odd electrode pairs in the x-direction and for the even ones in the y-direction. In combination with the rotation of the molecules around the synchronous molecule in longitudinal phase space, this can result in phase instabilities. That are regions in phase space where no transmission of molecules occurs even though the parameters of the molecules (position, velocity) are well within the so-called acceptance of the decelerator.

The molecule output of the Stark decelerator is displayed in Figure 4.7, where the 2D longitudinal phase-space around the synchronous molecule of the 94-stage Stark-deceleration sequence is shown. The sequence used here, decelerates the ammonia molecules in the upper $|J, K\rangle = |1, 1\rangle$ inversion doublet component from initially $v_{z,i} = 320\,\mathrm{m/s}$ down to $v_z = 20\,\mathrm{m/s}$. This plot is the result of a trajectory simulation. Since the initial packet of molecules generated by the pulsed valve is comparably large due to the opening time of approximately $100\,\mu\mathrm{s}$, several stages in the Stark decelerator are populated with molecules. These different packets are decelerated simultaneously and spaced by two longitudinal stages (11 mm). The black packet of molecules has the highest molecule density because it is optimized with respect to the output of the pulsed valve. It contains the synchronous molecule for the switching sequence and is thus called the synchronous packet. There are also packets ahead of the synchronous (black) packet; however these experienced at least one deceleration stage less and are consequently faster. To avoid the mixing of molecules from the different packets emitted by the Stark decelerator, the switching sequence was adapted with an additional (95th)

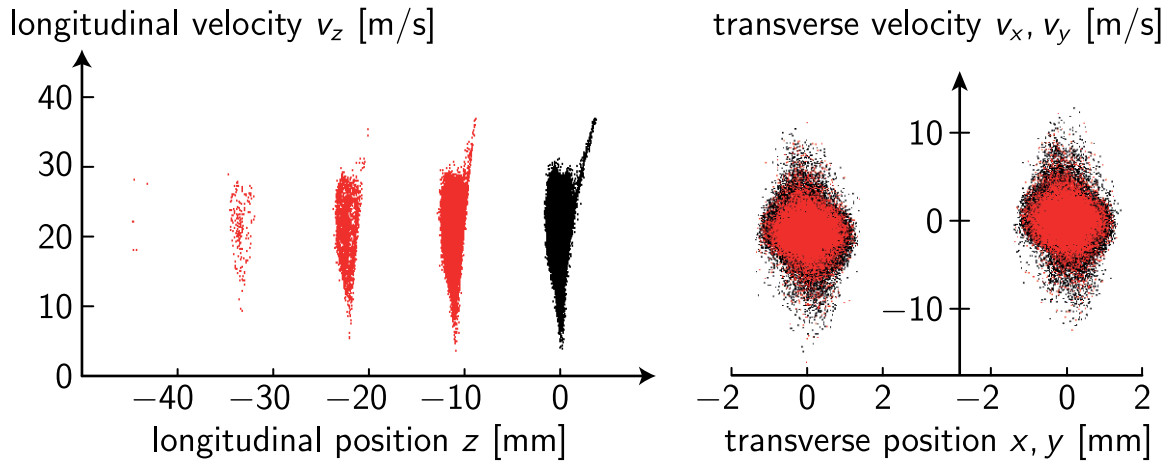

Figure 4.7: Phase-space plots from a trajectory simulation for the Stark decelerator used throughout the experiments described in this thesis. The left shows the 2D longitudinal phase space with the molecule packet that contains the synchronous molecule in black (synchronous packet). The trailing packets contain fewer molecules and are usually eliminated with a special switching sequence to obtain a cleaner output for the subsequent microwave manipulation experiments. The 2D transverse (x and y-direction) phase-space plots from the same simulation output are shown on the right side.

switching stage. Then, the trailing (red) packets from Figure 4.7 are decelerated even further. Molecules in a trailing packet with a velocity below approximately 33 m/s can even be reflected back into the Stark decelerator.

4.2 Microwave resonators

4.2.1 Closed resonators

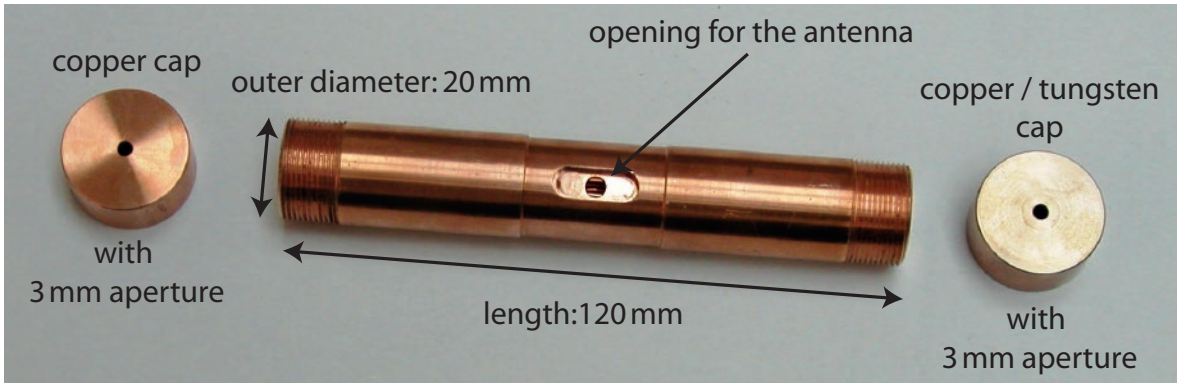

Figure 4.8: Closed resonator components, i.e., a copper cap with a central hole (left), the hollow copper cylinder with a central opening for the antenna and outer threads for the caps (middle), and the cap made from a copper/tungsten mixture (right).

The closed microwave resonators are copper cylinders with an outer diameter of

20 mm, a well-defined inner diameter $2R$ and length d. They are closed by threaded caps with 3 mm diameter apertures in the center, so that their actual lengths are adjustable and the molecules can still fly through. The length and the diameter are chosen such that the resonance frequency (see Eq. 2.29) of the desired mode is close to resonance with the inversion transition of ammonia ($^{14}NH_3$) at 23.695 GHz. An example for the $TE_{1,1,12}$ mode in the closed resonator 3 at 23.754 GHz is shown in Figure 4.9. Also the antenna is depicted, but scaled by a factor of 6 in the longitudinal direction for better visibility; the actual diameter of the wire is only 0.1 mm

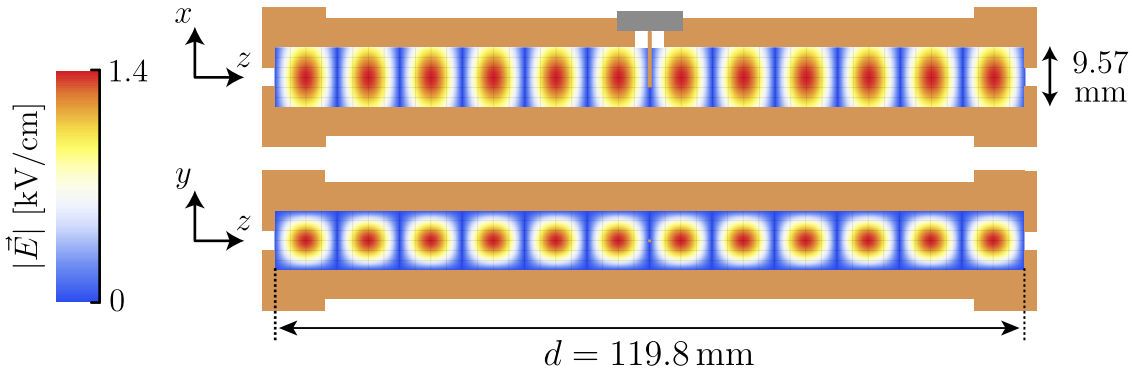

Figure 4.9: Density plot of the electric field distribution of the $TE_{1,1,12}$ mode in the cylindrically symmetric closed resonator 3. The resonance frequency of the not cylindrically-symmetric mode is $\nu_{1,1,12} = 23.754$ GHz. The antenna width is scaled up by a factor of six for clarity.

The end cap towards the detection zone is made of copper. On the Stark-decelerator side, the cap is made of a much more resilient copper/tungsten mixture. The outside is polished so that the softer copper is removed and mainly tungsten remains. The high surface hardness and the high melting point (3422 °C) of tungsten assure protection against damage from high-voltage discharges. The microwave lenses are precisely 120 mm long with an inner diameter of 7.41 mm (closed resonator 1) and 7.40 mm (closed resonator 2). The precision of the inner diameter is particularly important since already small deviations have a strong impact on the resonance frequency. Both lenses are fabricated on a lathe using a long, six-edged reamer. The microwave decelerator (closed resonator 3) is 119.8 mm long with an inner diameter of 9.57 mm at room temperature. It is made using a wire cutting EDM machine which provides a better uniformity of the circular hole in the resonator. The reamer, however, makes a slightly better, i.e., smoother surface.

The length and inner diameter of the microwave decelerator at 77 K can be calculated using the following formula:

$$L(T) = L_0 e^{\alpha(T-T_0)},$$

with the linear thermal expansion coefficient α, that is approximately $14.1 \cdot 10^{-6}\,\mathrm{K}^{-1}$ in the range from room temperature to 77 K. Then the length of the closed microwave decelerator at 77 K is 119.43 mm and the inner diameter is 9.54 mm.

The precision of the inner diameter is important since deviations of only 10 μm shift the resonance frequency by about 30 MHz in the microwave lenses and by about 15 MHz

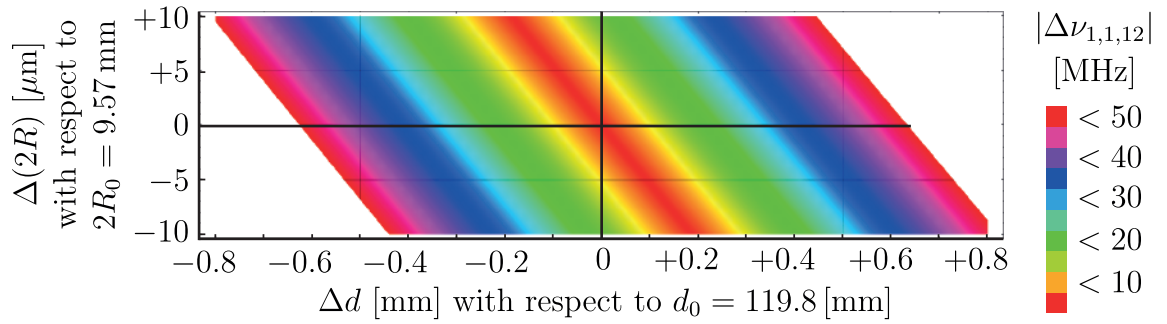

Figure 4.10: Deviation of the resonance frequency $\Delta\nu = |\nu_{1,1,12}(R,d) - \nu_{1,1,12}(R_0,d_0)|$, see Equation 2.28, in the closed microwave decelerator depending on variations of the length d and the diameter $2R$ with respect to the actual room temperature values $d_0 = 119.8\,\text{mm}$ and $2R_0 = 9.57\,\text{mm}$.

in the microwave decelerator as can be seen from Figure 4.10. The aperture size could be proven to be a good compromise between a high molecule transmission and acceptable microwave attenuation.

4.2.2 The open resonator

The open resonator is shown in Figure 4.11. It is a Fabry–Pérot type resonator made from two metal mirrors. The mirror that is closest to the Stark decelerator is made from the same copper/tungsten mixture as used for the front cap of the closed resonators (see Sec. 4.2.1) to prevent discharges from the high-voltage electrodes. The spherical mirrors, with radii of curvature of 100 mm and a diameter of 70 mm, are spaced by 46.2 mm. Both mirrors have a 3 mm diameter aperture in the center, one for the molecular beam to pass through and one for the dipole antenna (see also Sec. 4.4).

The mode close to the inversion transition in ammonia is the $\text{TEM}_{0,0,6}$ mode at 23.774 GHz which corresponds to a detuning of $\Delta = +79\,\text{MHz}$ with a loaded quality factor of $Q_L \approx 15\,000$. The electric field distribution of the $\text{TEM}_{0,0,6}$ mode is depicted in Figure 4.12. The analytical solutions for the fields are introduced in Section 2.9. The beam waist (w_0), the narrowest part of the electric field distribution in the transverse direction, is in the center of the resonator. It is defined as the distance from the resonator axis to where the field amplitude drops to 1/e with respect to the value on the axis. Here, the spot size of the Gaussian beam, that is $2w_0$, amounts to 26 mm. Directly next to the mirrors, the beam width amounts to 29.6 mm according to Equation 2.63.

4.3 Microwave electronics

The electronic components used for the microwave-manipulation experiments are outlined in Figure 4.13. The microwave radiation is generated with a signal generator, SMR 27 by Rohde & Schwarz, with a frequency range of 1 kHz–27 GHz (Fig. 4.13(1)). The generator has a maximum output power at 23.75 GHz of about 17 dBm ($\approx 50\,\text{mW}$) and is connected to the power amplifier via a high-speed single-pole double-throw

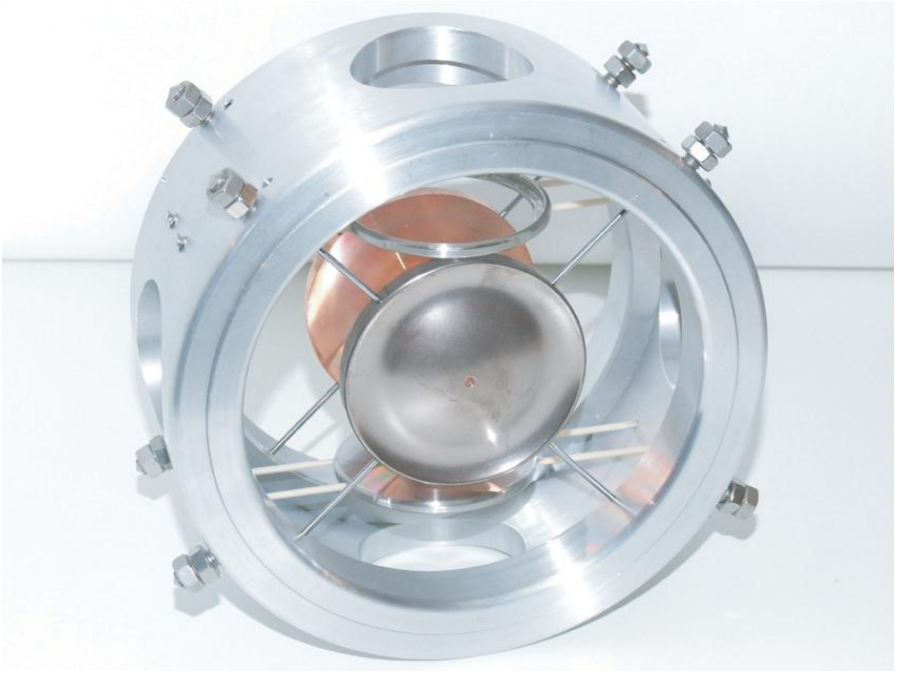

Figure 4.11: Photograph of the open resonator (Fabry–Pérot type) in an aluminum casing for easy alignment with the molecular beam. The front mirror is made from a copper/tungsten mixture. The 3 mm diameter aperture for the molecular beam can be seen. The rear mirror is made of plain copper. The two TOF electrodes, the stainless steel plate on the bottom of the resonator and the mesh on top of the mirrors, are spaced by 80 mm.

(SPDT) PIN-diode switch, SFB-0526 by Sierra Microwave (Fig. 4.13(2)). The switch allows for rapid switching (between on and off) for the microwave feed to the amplifier. In the microwave lenses this is used to apply a microwave field to the resonator only when molecules are in the lens to minimize thermal heating and frequency drifts. In the microwave decelerators the rapid switching is required to change the forward motion of the molecules. The solid state power amplifier, MKU 2410A from Kuhne Elektronik (Fig. 4.13(4)), has a narrow bandwidth around 23 694 MHz and delivers up to 10 W (40 dBm) of output power with a maximum gain of 30 dB. A coaxial circulator, SMC1826 by SMT (Fig. 4.13(5)), prevents back reflection from the resonator into the power amplifier and enables reflected signal to be monitored using a detector diode, 8473C by Agilent (Fig. 4.13(7)) and an oscilloscope, TDS 220 by Tektronix (Fig. 4.13(8)). The detector diode tolerates power levels up to 1 W, thus, an attenuator, AF868-10 by ATM (Fig. 4.13(6)), is required to protect it from potentially higher power levels. All coaxial cables, the SMA (sub-miniature A) connectors and the other passive components, for instance the vacuum feed-through, cause power losses. Consequently, maximum power that is delivered to the position of the antenna is between 6 and 7 W, depending on the actual experiment. For the microwave lenses and the open resonator, the power was 6 W, and for the closed decelerator 7 W was reached.

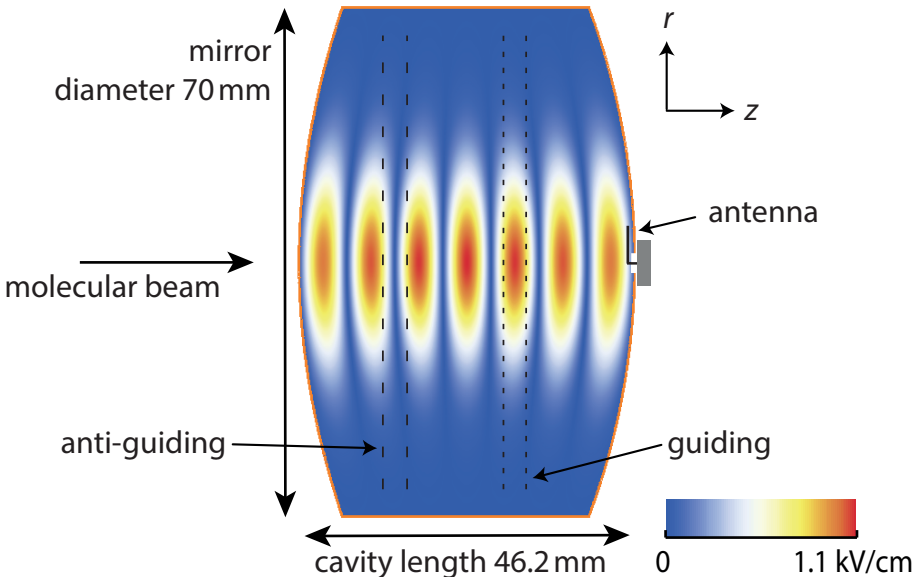

Figure 4.12: Density plot of the electric field distribution of the cylindrically symmetric $TEM_{0,0,6}$ mode in the open resonator at 23.774 GHz. The antenna is drawn to scale, however in the real Fabry–Pérot cavity, the antenna is bent to follow the curvature of the copper mirror.

4.4 Coupling

The microwave electronics described in the previous section deliver the microwave radiation via coaxial cables. An antenna is required to couple the coaxial feed line to the $TE_{1,1,p}$ and $TEM_{0,0,q}$ modes in the different resonators. Ideal in both cases is capacitive coupling using a simple dipole antenna. The antennas are modified from commercially available SMA panel receptacles that feature an SMA jack on one side and a central pin (typically beryllium-copper) surrounded by a PTFE layer on the other side. In the case of the microwave lenses (resonators 1 and 2), the central pin is machined down to 0.4–0.5 mm diameter and the length of the pin is optimized experimentally. For the microwave decelerators (open and closed) additional degrees of freedom and smaller antenna diameters were required. The pin is replaced by a 0.1 mm copper wire, soldered to the receptacle. In all cases, the PTFE isolates the central pin from the resonator body, and it allows for a tight fit to the antenna opening (Fig. 4.8, closed resonators) and stabilizes the antenna position. The coupling can be monitored by measuring the microwave intensity that is reflected from the resonator, U_R. The reflection coefficient, ρ, is the ratio of reflected intensity to the input intensity, $\rho = \frac{U_R}{U_{IN}}$. Then the coupling coefficient, κ, can be defined as

$$\kappa = \frac{1+\rho}{1-\rho}. \tag{4.1}$$

The two limiting cases are

a) perfect or critical coupling: no power is reflected from the resonator, hence $\rho = 0$ and $\kappa = 1$.

b) all microwave intensity is reflected (no coupling), then $\rho = 1$ and $\kappa \to \infty$.

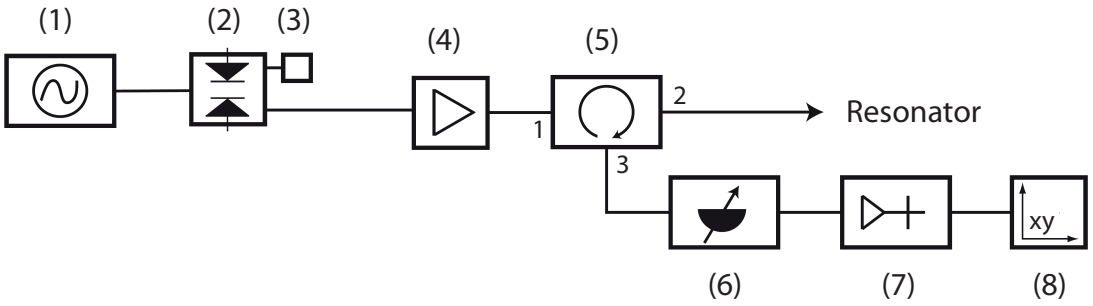

Figure 4.13: Schematic setup of the microwave electronics: (1) Microwave signal generator with frequency range of 1 kHz–27 GHz (SMR 27, Rohde & Schwarz), (2) pin diode switch SPDT (SFB-0526, Sierra Microwave), (3) termination (50 Ω), (4) power amplifier (MKU-2410 A, Kuhne Elektronik), (5) circulator 18–26 GHz (SMC1826, Sierra Microwave), (6) adjustable attenuator 14–26 GHz (AF868-10, Advanced Technical Materials), (7) detector diode 10 MHz–26.5 GHz (8473C, Agilent), (8) oscilloscope (TDS 220, Tektronix)

The system of the microwave resonator and the driving electronics can be understood as capacitively coupled resonant circuits. The coupling is good if the impedance of the two circuits is matched. In the case of the microwave resonators, this is achieved by adjusting the length and the precise position of the antenna. The antenna made of thin wire can be bent into the appropriate position. As a rule of thumb, the optimum antenna length corresponds to approximately $\lambda/2$ for microwave frequencies above 10 GHz. For the experiments discussed in this thesis the antennas are typically 5–7 mm long, except for the case of the $TE_{1,1,1}$ mode. Below 10 GHz it is generally more practical to choose antenna lengths close to $\lambda/4$.

At this point, it is instructive to reconsider the power delivered to the cavity, P_{IN}. From a theoretical point of view, two resonant circuits are capacitively coupled. One contains the driving circuitry, as mentioned above (Sec. 4.4), and the other one is the microwave resonator. Maximum power transfer occurs in the case of critical coupling. Then the power delivered to the two circuits is equal:

$$P_{\mathrm{IN}} = \frac{1}{1+\kappa} P_0. \tag{4.2}$$

From this equation, the power delivered to the various $TE_{1,1,p}$ modes and the $TEM_{0,0,6}$ mode, P_{IN}, can be calculated from the coupling coefficients and the available power at the position of the antenna, P_0. The coupling to an external resonant circuit also affects the quality factor Q (see also Sec. 2.6). The quality factor can be determined accordingly by the full width at half maximum (FWHM or $\Delta\nu$) of the resonance. The ratio of the resonance frequency to the FWHM gives the quality factor,

$$Q_L = \frac{\nu_{1,1,p}}{\Delta\nu}. \tag{4.3}$$

This measured quality factor, the so-called loaded Q_L, is always the collective quality factor of the external system, Q_E, and of the bare resonator, Q_0 (Eq. 2.50 for the $TE_{1,1,p}$

mode). Adding up quality factors is briefly mentioned in Chapter 2:

$$\frac{1}{Q_L} = \frac{1}{Q_0} + \frac{1}{Q_E}. \tag{4.4}$$

Including the coupling effect, the loaded quality factor is connected to the unloaded Q_0 of the resonator via

$$Q_L = \frac{Q_0}{1+\kappa}. \tag{4.5}$$

In the case of critical coupling ($\kappa = 1$), the loaded Q_L is half of the unloaded Q_0. This relation has to be considered when comparing the values from Equation 2.50 with the measured Q_Ls. Using the loaded Q_L and the power delivered to the resonator P_{IN}, the electric field strength in the cavity, E_0, can be determined using Equation 2.55. Table 4.1 shows all important values of the various employed $\mathrm{TE}_{1,1,p}$ modes in the different resonators.

Table 4.1: List of the relevant modes in the various microwave resonators. The closed resonators 1 and 2 are microwave lenses. The open resonator and the closed resonator 3 are microwave decelerators. $\Delta\nu$ is the full width at half maximum of the respective resonance and the detuning Δ is given with respect to the inversion transition in $^{14}NH_3$ at 23 695 MHz.

resonator	mode	$\nu_{1,1,p}$ in MHz	$\Delta\nu$ in MHz	Q_L	detuning in MHz
closed 1	$\mathrm{TE}_{1,1,2}$	23 765	4.5	5200	71
closed 1	$\mathrm{TE}_{1,1,4}$	24 152	6.1	3959	457
closed 2	$\mathrm{TE}_{1,1,1}$	23 761	6.75	3520	66
open	$\mathrm{TEM}_{0,0,6}$	23 774	1.53	15 000	78
closed 3 at RT	$\mathrm{TE}_{1,1,12}$	23 695	5.0	4740	0
closed 3 at 77 K	$\mathrm{TE}_{1,1,12}$	23 753	2.7	9100	58

The antenna is a conductor and thus introduces additional boundary conditions to the electromagnetic field in the resonator. In the closed resonators 1 and 3, the antenna is placed in the center of the resonator (see Fig. 4.8), so that the mode requires an electric field node at the position of the antenna. Modes with a field maximum at this position are suppressed. Consequently, the closed resonators 1 and 3 support only $\mathrm{TE}_{1,1,p}$ modes with even p. The antenna for the closed resonator is optimized for the $\mathrm{TE}_{1,1,2}$ mode and has an optimum length of 5.5 mm. Resonator 2 was designed to support the $\mathrm{TE}_{1,1,1}$ mode to study microwave focusing when no additional electric field node is in the middle of the resonator (see also Fig. 2.5). In order to achieve reasonable coupling, which also means without disturbing the field too much, the antenna opening had to be close to the end of the copper cylinder (approximately 5 mm). The best value for the antenna length is found experimentally to be only 1.75 mm, significantly shorter than $\lambda/4$ (3.15 mm for 23.7 GHz). This short antenna length is a compromise to allow for coupling to the field without disturbing it. Consequently, the reflected power at resonance with respect to

the reflected power off resonance is approximately $U_R = 10\%$ for the $TE_{1,1,1}$ compared to only 3–5% for the even modes in the closed resonator 1 (see also Tab. 4.2).

In the open Fabry–Pérot resonator, a 0.3 mm diameter and approximately 6.5 mm long wire is used as antenna. It is placed in the center of the rear spherical mirror and is bent such that it follows the curved mirror surface as good as possible. The node of the electric field is at the mirror surface which means that it is imperative to get the wire as close as possible to the mirror surface without shorting it out.

Table 4.2: List of the available power P_0, the reflected power on resonance U_R, the coupling coefficient κ (Eq. 4.1) the actual input power P_{IN} (Eq. 4.2) and the resulting maximum electric field strength $E_{0,max}$ in the different resonator at their respective resonance frequencies. The maximum electric field strength is determined using Equation 2.55 and the also experimentally determined quality factors (Q_L) that can be found in Table 4.1.

mode	resonator	P_0 in Watt	U_R	κ	P_{IN} in Watt	$E_{0,max}$ in kV/cm
$TE_{1,1,2}$	closed 1	5.6	3%	1.06	2.7	1.31
$TE_{1,1,4}$	closed 1	5.6	6%	1.13	2.6	1.11
$TE_{1,1,1}$	closed 2	7.6	11%	1.24	3.4	1.21
$TEM_{0,0,6}$	open	7.16	5%	1.11	3.4	1.14
$TE_{1,1,12}$	closed 3	7.16	11%	1.24	3.1	1.44

The closed resonator 3, the second generation microwave decelerator, is designed for the $TE_{1,1,12}$ mode. That means the antenna can be conveniently mounted in the center of the resonator. The antenna is an approximately 6 mm long, 0.1 mm diameter copper wire soldered to an SMA receptacle. Since the resonator is cooled to 77 K during operation, achieving perfect coupling is challenging. Consequently, the coupling (10% reflected microwave power at resonance) is slightly worse than for the modes in the closed resonator 1. Table 4.2 shows the available power at the antenna, as measured by a detector diode. From this, the power coupled into the resonator can be calculated using the coupling coefficient according to Equation 4.1. The maximum electric field strength in the resonators can thus be calculated using Equation 2.55 for the $TE_{1,1,p}$ mode in the closed resonators and with Equation 2.64 for the $TEM_{0,0,q}$ mode in the open Fabry–Pérot resonator.

4.5 Detection

For the detection of ammonia molecules in the experiments presented here, the so-called 2+1-REMPI process is used, Ref. [176]. REMPI is short for resonance enhanced multi-photon ionization. The 2+1 indicates that two photons are required to excite the molecule from the ground state $X(v_2 = 0)$ into an electronically and vibrationally excited state ($B(v_2 > 0)$). The third photon of the same wavelength ionizes the molecule (see

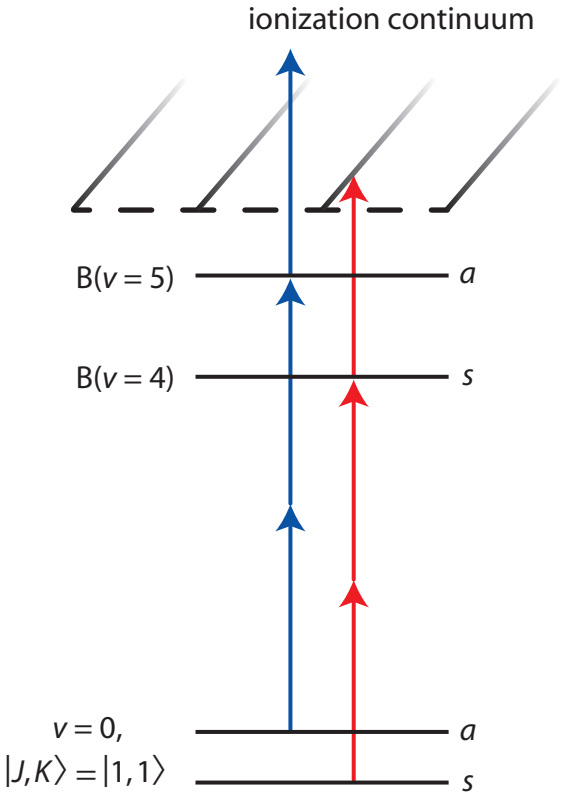

Figure 4.14: Schematic of the 2+1-REMPI detection process for ammonia molecules in the $|J, K\rangle = |1, 1\rangle$ inversion doublet. The a and s are the symmetry labels of the states involved. The energy differences are not drawn to scale: n the ground state the inversion splitting is less than $1\,\mathrm{cm}^{-1}$ whereas the energy difference between the $|B, v_2 = 4\rangle$ and $|B, v_2 = 5\rangle$ state is about $600\,\mathrm{cm}^{-1}$, allowing for state-selective detection.

also Fig. 4.14). The parent ion is detected in a simple time-of-flight mass spectrometer of Wiley-McLaren type [173] with a 250 mm drift tube. The first acceleration stage for the ions is made up by two electrode plates with a 3 mm aperture for the molecules to fly through and a 10 mm aperture for the ions to pass through. The apertures are covered with a fine nickel mesh to allow for a high particle transmission and homogeneous electric fields. The electrode spacing is about 5.5 mm and the repeller voltage is +1.9 kV with the extractor at $+500\,V$. The 250 mm long flight tube at −1.2 kV is the subsequent focusing stage. The ions are finally collected on a Jordan micro channel plate set to −2.1 kV.

The states of interest in ammonia, the $|J, K\rangle = |1, 1\rangle$ inversion doublet, requires near-UV radiation of 317 nm for the lower inversion doublet component or 312 nm for the upper inversion doublet component. Since 2+1-REMPI involves a two-photon transition, this non-linear process requires high photon intensities. This is achieved by a tunable Nd:YAG-pumped-dye-laser system. The Nd:YAG laser, a Spitlight 500 from InnoLas, produces 500 mJ per pulse of 1064 nm light at a 10 Hz repetition rate. In a subsequent second-harmonic-generation (SHG) unit, the light is converted into approximately 300 mJ per pulse of 532 nm in an anti-reflex coated lithiumtriborate (LBO) crystal. For the dye laser (Narrowscan by Radiant Dyes) we use the bright orange dye DCM (4-(dicyanomethylene)-2-methyl-6-(4-dimethylaminostyryl)-4H-pyran) dissolved in ethanol to generate broadband light on the order of 620 to 640 nm. A specific wavelength is chosen by using a resonator consisting of two grazing-incident gratings. This light is then amplified in subsequent amplification stages up to approximately 60–70 mJ per pulse. The red laser light is frequency doubled in an additional subsequent SHG unit, a KDP

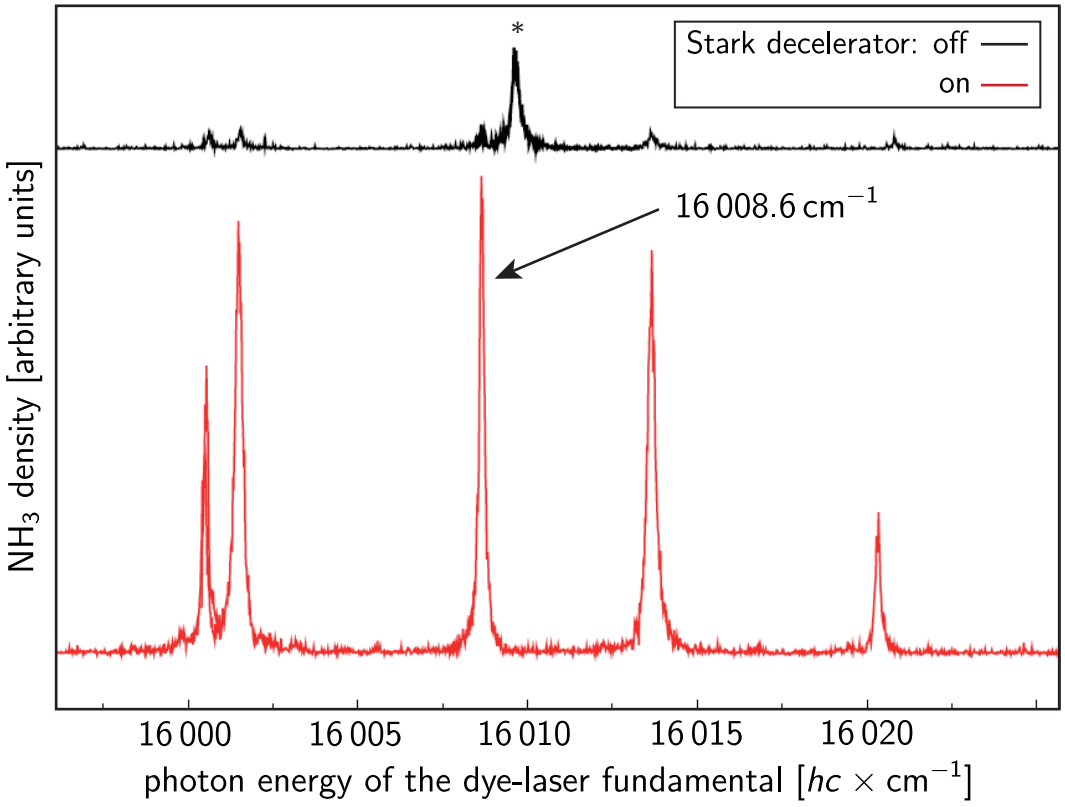

Figure 4.15: Rotationally resolved 2+1-REMPI spectrum for $^{14}NH_3$ obtained behind the Stark decelerator. The bottom trace is recorded with the Stark decelerator on and the top trace with the Stark decelerator off. Here, the 2+1-REMPI channel is the $|X, v_2 = 0\rangle \rightarrow |B, v_2 = 5\rangle$ transition. The individual transitions belong to different rotational sublevels of the $|B, v_2 = 5\rangle$ state. The molecule's initial $|J, K\rangle$ level is the $|1, 1\rangle$ state. All peaks except the one labeled with a star originate from the low-field-seeking upper inversion doublet component. The field-free transition that is labeled with a star has to originate from a high-field-seeking state possibly from higher v- or J-levels, since it disappears when the electric fields are switched on. The most intense transition at 16 008.6 cm^{-1} is used for the detection in the molecular beam experiments.

(potassiumdiphosphate) crystal, and 12–16 mJ per pulse UV radiation is obtained.

The different symmetries of the upper and lower inversion doublet components have to be conserved in a two-photon excitation. The selection rules allow for molecules in the lower $|J, K\rangle = |1, 1\rangle$ component (symmetric) only to be excited to the symmetric $|B, v_2 = 4\rangle$ state and for molecules in the upper inversion doublet component only into the $|B, v_2 = 5\rangle$ state. The energy difference due to these two pathways exceeds the bandwidth of the dye laser by far, so that the two states can be detected selectively (see also Figure 4.15). Figure 4.15 shows a rotationally resolved 2+1-REMPI spectrum for $^{14}NH_3$. Both traces are recorded directly behind the Stark decelerator with the Stark decelerator switched on (red trace) or off (black trace). The transverse focusing effect of the electric fields in the Stark decelerator on molecules in the antisymmetric, DC-low-field-seeking states is clearly visible. The strongest transition at 16 008.6 cm^{-1} is used

throughout the experiments described in this thesis.

The analog signal from the multi-channel plate is converted into a digital signal that can be interpreted by the homemade data acquisition software KouDA, by an Acqiris high-speed cPCI digitizer card, model dc438, with 12 bit and a sampling rate of 200 MS/s. This makes it possible to capture 2 μs of the time-of-flight signal with 5 ns resolution.

4.6 Timings

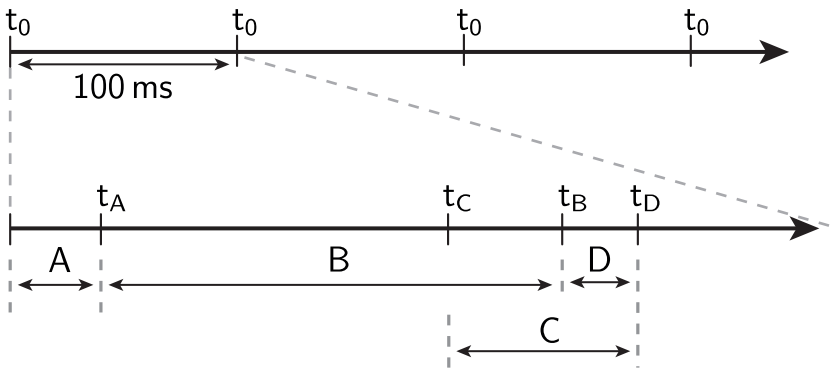

Figure 4.16: Schematic of the timings in the experiment. The repetition rate is 10 Hz (t_0 to t_0 = 100 ms). At the time t_0, the valve is triggered and opens for about 100 to 150 μs. A is the delay between the valve trigger and the start of the burst unit. The burst unit triggers the fast switchings of the hexapole, the Stark decelerator and also the microwave resonator. It is optimized to the valve conditions. B is the delay until the burst unit is switched off (t_B). D is a safety delay of typically 20 μs to ensure that no electric fields are present when the detection laser fires. t_D triggers the Q-switch of the detection laser. $C = t_D - 225\,\mu s$ is defined with respect to the laser firing and gives the trigger for the flashlamp of the Nd:YAG laser. This delay is optimized for maximum laser power. For the time-of-flight scans shown in this chapter, the time delay B is scanned.

In the experiments with the microwave lenses and the closed microwave decelerator, the ammonia molecules travel a total distance of 136 mm from the exit of the Stark decelerator to the detection region. Using the open Fabry–Pérot decelerator, the detection region is in the middle of the resonator which is approximately 35 mm downstream from the exit of the Stark decelerator.

The main tool to monitor the effects of the microwave field on the molecules is to measure the ammonia density in the detection zone as a function of the arrival time B as displayed in Figure 4.16. These time-of-flight measurements are used throughout the following Chapter 5 and their origin of time is when the Stark decelerator is switched off.

As a last experimental detail, the switching sequences of the microwave field are explained in greater detail in the following Section 4.7 .

4.7 Phase angles

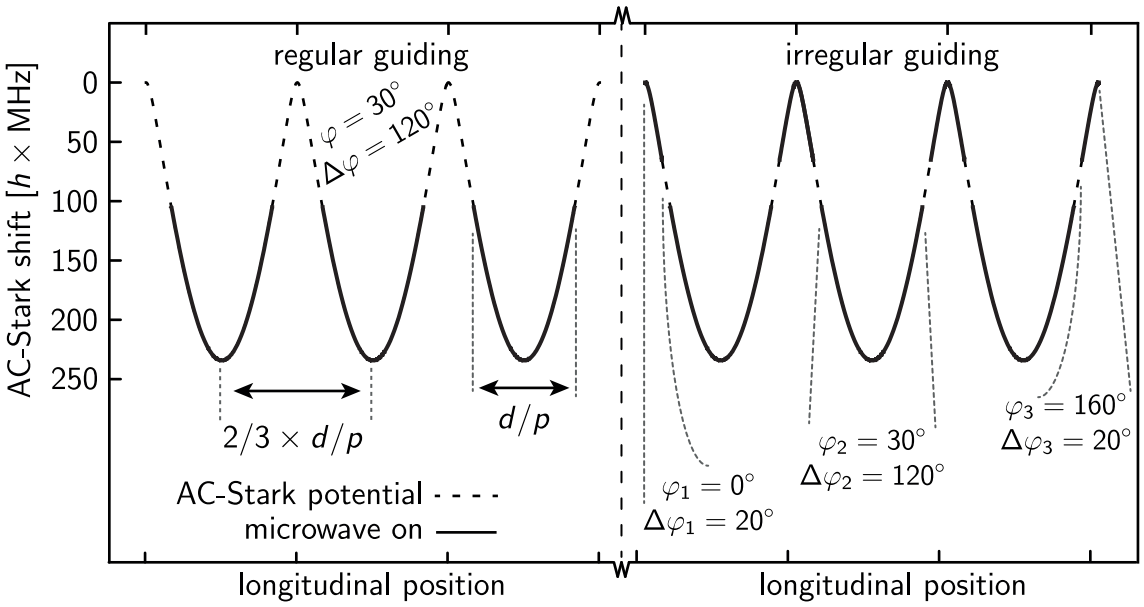

Figure 4.17: Potential of the synchronous ammonia molecule in the $|1,1,a\rangle$ state depending on the position, z, along the symmetry axis of the closed resonator (dashed curve). Two different switching schemes used for the guiding mode are indicated by the bold black lines. The regular guiding mode, $\varphi = 30°$ and $\Delta\varphi = 120°$, is shown on the left side. A modified guiding mode that additionally includes the electric field close to the nodes is shown on the right side. The indicated potential depth is valid for the closed microwave decelerator at 3 W input power.

Motion control in the longitudinal direction can be achieved by switching the microwave fields on and off at the appropriate times. Two switching schemes for guiding are displayed in Figure 4.17 and three switching sequences for acceleration and deceleration are depicted in Figure 4.18 and explained in greater detail in the following. The AC-Stark shift is approximately linear at the microwave field strengths in the resonators, $E_{0,\max} \approx 1.0$–$1.5\,\mathrm{kV/cm}$, consequently, the potential is essentially harmonic. In a blue-detuned microwave field ($\Delta > 0$), $^{14}NH_3$ molecules in the $|1,1,a\rangle$ state experience a potential that follows the negative absolute value of the electric field (see also Sec. 3.4 and in particular Eq. 3.11):

$$W_{\text{AC-Stark}} = -\sqrt{\frac{h^2\Delta^2}{4} + \frac{\mu^2}{16}|\vec{E}(\rho,\phi,z)|^2} + \frac{h\Delta}{2}.$$

The switching sequences are calculated for the so-called synchronous molecule, a fictitious molecule traveling along the symmetry axis of the microwave resonator, $\rho = 0$ and $\phi = 0$, with the exact initial longitudinal velocity that is supposed to be manipulated. This concept and how it relates to switching schemes have already been described in Section 4.1. Figures 4.17 and 4.18 are representations of the potential (AC-Stark energy) given by the $TE_{1,1,p}$ mode in the closed resonators of length d, however, the principle is equivalent for the $TE_{0,0,q}$ mode in the open resonator.

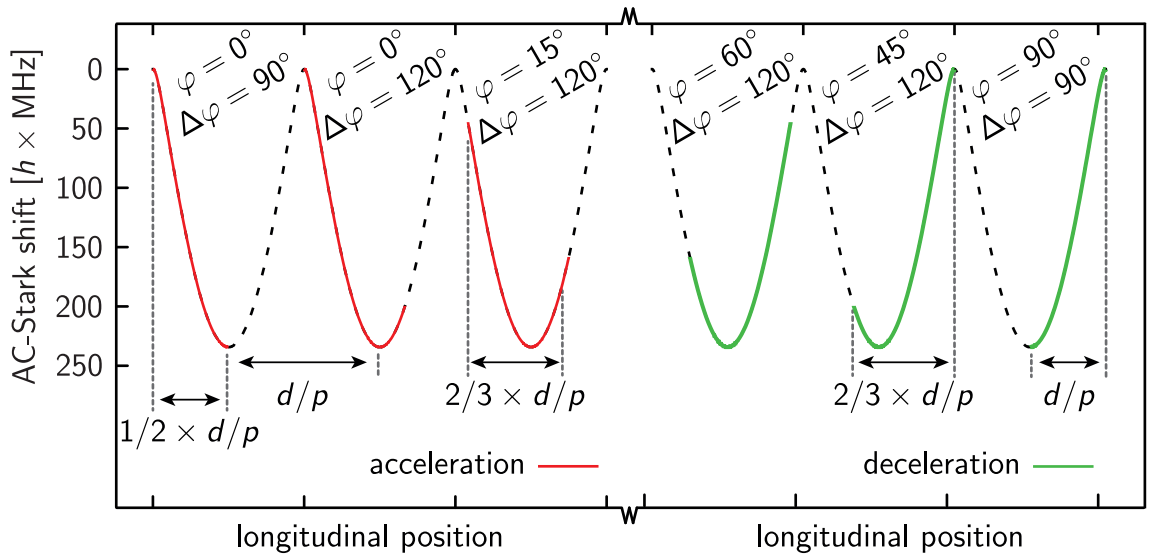

Figure 4.18: Potential of a $^{14}NH_3$ molecule in the $|1, 1, a\rangle$ state depending on the position, z, along the symmetry axis of a closed resonator. The corresponding switching schemes used for acceleration (red bold lines) and deceleration (green bold lines) of a packet of ammonia molecules are indicated. The potential depth indicated is valid for the closed microwave decelerator at 3 W input power.

The parameters for switching are defined as follows: in each stage, that is a single potential well, the fields are switched on when the synchronous molecule is at the position z_1. This position can be expressed using an angle $\varphi = 180° \cdot z_1/z_0$, with the length of a single stage $z_0 = d/p$. The microwave field remains switched on until the synchronous molecule arrives at the position $z_1 + \Delta z$. The distance Δz can also be converted into an angle: $\Delta\varphi = 180° \cdot \Delta z/z_0$. If multiple switching per stage is necessary, an additional index i indicates the switching cycle within a single stage $(\varphi_i, \Delta\varphi_i, \dots)$. $\Delta\varphi = 180°$ is the maximum duration that the fields can be turned on per single stage. Consequently, φ is zero, which corresponds to the lens mode.

The maximum acceleration that can be achieved this way is to only use the accelerating part of the potential, $\varphi = 0°$ with $\Delta\varphi = 90°$. Then the electric field is applied for half the time that the synchronous molecule spends in a single potential well. The same mode but for deceleration is the $\varphi = 90°$ with $\Delta\varphi = 90°$ sequence. The field close to the anti-nodes is much stronger than at the nodes, so that the transverse focusing benefits from reducing the maximum deceleration or acceleration by including a small part of the opposite longitudinal potential to increase the transverse focusing. This is shown in Figure 4.18 with the acceleration modes $\varphi = 0°$, $\Delta\varphi = 120°$ and $\varphi = 15°$, $\Delta\varphi = 120°$ or the deceleration sequences $\varphi = 45°$, $\Delta\varphi = 120°$ and $\varphi = 60°$, $\Delta\varphi = 120°$.

5 Results

5.1 The microwave lens

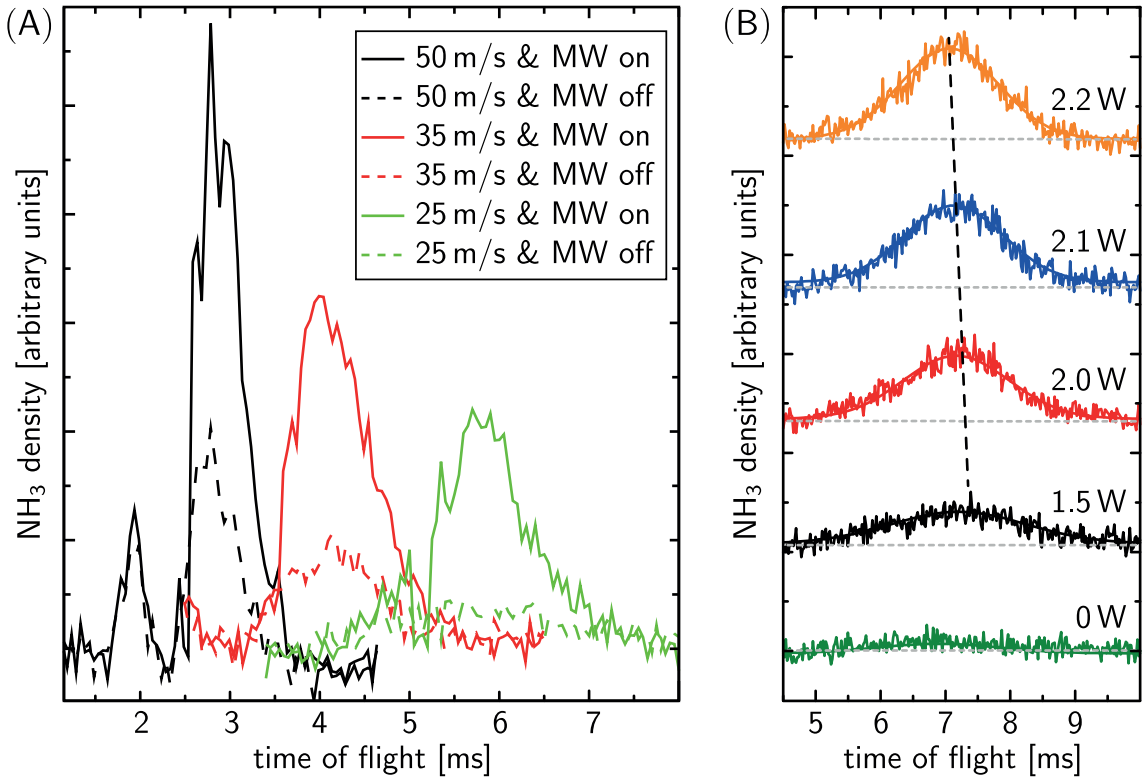

Figure 5.1: Microwave focusing of decelerated ammonia molecules in the $|1,1,a\rangle$ state as a function of their arrival time at the detection region (the total distance is 136 mm): (A) For three different forward velocities, v_z: 50 m/s (black), 35 m/s (red), and 25 m/s (green). Dashed curves represent measurements with microwave radiation turned off. (B) For 20 m/s slow ammonia molecules but with varying microwave input power P_{IN}. Bold curves are Gaussian-type fits to the experimental data.

The microwave lens mode is the elementary mode of operation since no switching of the microwave field is required. The blue-detuned $\mathrm{TE}_{1,1,p}$ mode exerts a net force on $^{14}\mathrm{NH}_3$ molecules in the $|1,1,a\rangle$ state in the transverse directions only. Figure 5.1(A) shows the experimental results for focusing ammonia molecules with different mean velocities of 50 m/s, 35 m/s, and 25 m/s in the $|1,1,a\rangle$ state using the $\mathrm{TE}_{1,1,1}$ mode in resonator 2. This mode has one field maximum in the longitudinal direction located in the middle of the resonator. The ammonia density is measured as a function of the time that the

molecular packet needs to travel from the exit of the Stark decelerator to the detection region (136 mm). For all three measurements, the microwave input power, P_{IN}, is approximately 3 W. All curves show a significant increase in signal intensity as compared to the measurements without microwave radiation (dashed lines): This amounts to an increase of circa 2.5 for 50 m/s compared to 3 for 35 m/s and 6 for 25 m/s. The different packet widths in the time-of-flight profiles are due to the different mean velocities of the packets in combination with the free flight in the forward direction. An additional peak is visible in the measurement for the 50 m/s slow molecules: These molecules belong to a second packet that is ahead of the packet of interest (with the actual 50 m/s). That means, it has experienced one Stark-deceleration stage less. Thus the mean velocity of this packet is approximately 70 m/s. For this considerably higher initial velocity, the transverse focusing is much weaker, as can be understood from the focal length of a microwave lens (see Sec. 5.2, in particular Eq. 5.8 and 5.9). In Figure 5.1(B), similar measurements using the $\mathrm{TE}_{1,1,2}$ mode in the closed resonator 1 with varying input power, P_{IN}, are displayed for ammonia molecules with a mean velocity of approximately 20 m/s. The intensity of the ion signal decreases with decreasing microwave power due to weaker focusing forces. Also, the position of the peak maximum is shifted towards slightly later arrival times. This clearly indicates that for different microwave powers different molecule velocities and thus different fractions of the molecular packet will be focused best.

Figure 5.2(A) shows the ammonia density in the detection zone depending on the microwave power, P_{IN}, for different detection times. At these low velocities ($v_z \ll 50$ m/s) a special switching sequence in the Stark decelerator is used so that only one packet of molecules is emitted, to a good approximation. The microwave lens does not affect the longitudinal motion of the molecules significantly. Consequently, the detection times correspond to different molecular velocities. All curves feature a steep increase in signal intensity with increasing microwave power, P_{IN}. A signal maximum occurs when the focus of the microwave lens overlaps best with the focus of the detection laser that has a beam waist of approximately 100 μm. For molecules traveling with $v_z \approx 20.5$ m/s, this maximum occurs around $P_{\mathrm{IN}} = 2.6$ W. A further increase of the microwave power shifts the lens focus closer to the microwave resonator and the ion signal becomes weaker. This is referred to as overfocusing and can be observed clearly for slower molecules with $v_z \approx 18.8$ m/s for which the maximum is located at around 2.0 W. For $v_z \approx 18.1$ m/s and $v_z \approx 14.0$ m/s slow molecules, the signal maximum is shifted to 1.6 W and 0.56 W, respectively.

5.2 Focal length of a $\mathrm{TE}_{1,1,p}$-mode microwave lens

In this section, an analytical expression for the focal length, L, of the $\mathrm{TE}_{1,1,p}$-mode microwave lens as shown in Figure 5.3 is derived. This requires a number of approximations: First it is assumed that the longitudinal motion is constant ($\dot{v}_z = 0$), which is strictly speaking incorrect because the molecules experience a small acceleration in the first half of each stage ($d/2p$) followed by a small deceleration in the second half. These two effects cancel each other in the sense that the final velocity is equal to the initial velocity but they bring about a reduced transit time of the molecules. Nonetheless, this

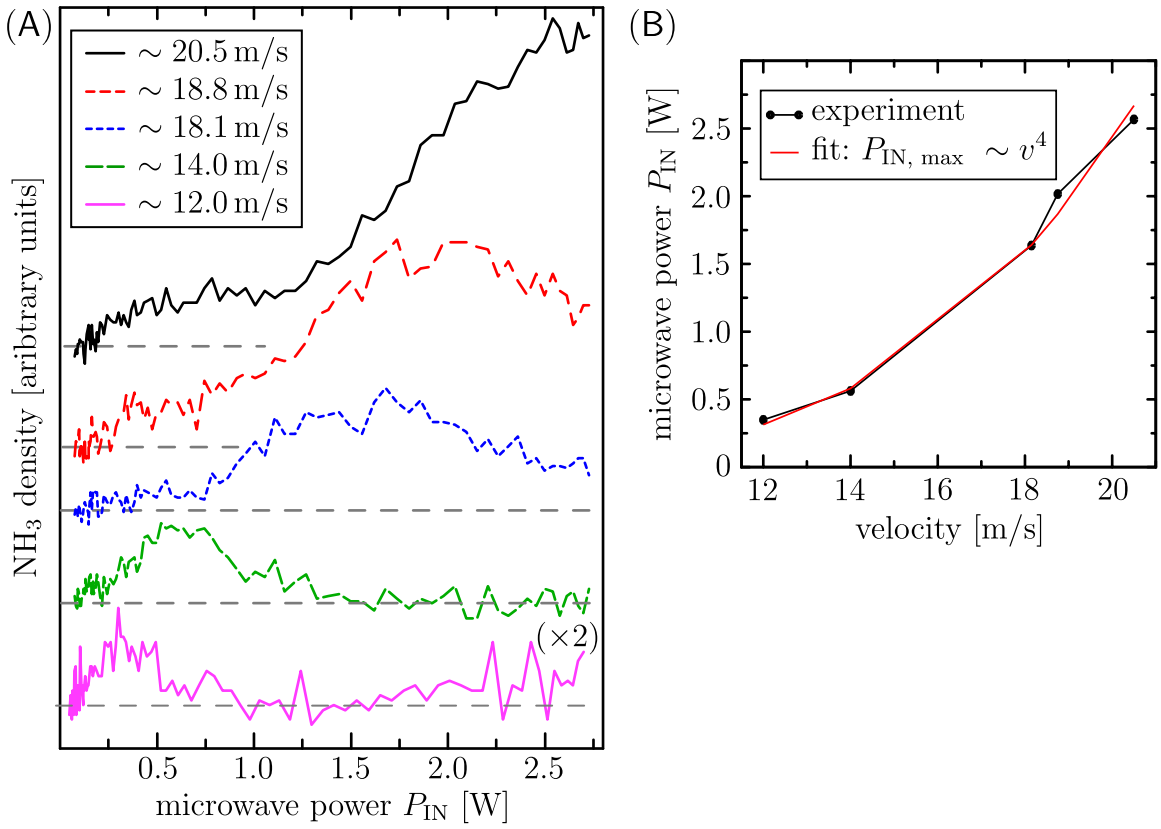

Figure 5.2: (A) Density of $^{14}NH_3$ molecules as a function of the microwave power, P_{IN}, for five different observation times and thus molecule velocities. The mean velocity of the packet is $v_z = 20\,\mathrm{m/s}$. The bottom trace is scaled by a factor of 2 for better visibility. (B) The optimum microwave power in Watt as a function of the corresponding molecule velocity. The black curve (with dots) shows the experimentally obtained data, while the red solid curve gives a fit to the experimental data according to Equation 5.8 (Sec. 5.2).

effect is small because the microwave lenses feature only a few (1–2) longitudinal electric field maxima. Second, the forward motion is considered decoupled from the transverse motion, as well as the radial from the azimuthal motion. Third, the anharmonicity in the potential, Equation 3.11, is neglected. Then the potential can be described by a harmonic oscillator (HO) potential. The equation of motion of a general harmonic oscillator is $\rho(t) = A\sin(\omega_{HO}t + \varphi)$ with the angular frequency of the harmonic oscillator $\omega_{HO} = \sqrt{f/m}$ and a constant phase φ. Here, f is the force constant and m the mass of the HO. The initial coordinates, ρ_0 and $v_{\rho,0}$ of the oscillator are incorporated in the constants A and φ according to

$$A = \sqrt{\rho_0^2 + \left(\frac{v_{\rho,0}}{\omega_{HO}}\right)^2}$$
$$\tan\varphi = \frac{\rho_0\omega_{HO}}{v_{\rho,0}} \tag{5.1}$$

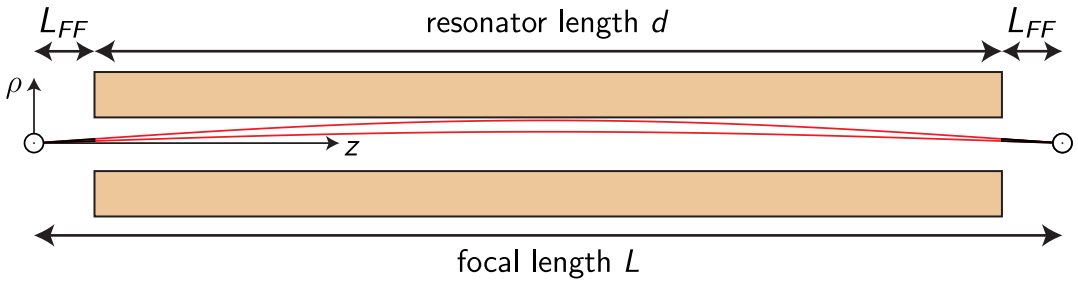

Figure 5.3: Schematic of the focal length L of the microwave lens (cylindrically symmetric closed resonator) with L being approximately as large as the resonator length d ($L - d \ll L$).

The constant longitudinal motion connects the time to the longitudinal position, $t = \frac{z}{v_z}$, and it follows:

$$\rho(z) = A \sin\left(\sqrt{\frac{f}{m}}\frac{z}{v_z} + \varphi\right).$$

The molecules are emitted from a point source and after a free-flight distance L_{FF} they arrive in the microwave lens with length d followed by a final free-flight distance which is considered to be of the same length as the first one. For convenience, the z origin is set to the beginning of the microwave lens and thus the harmonic potential. Then, focusing requires $\rho(z = 0) = \pm\rho(z = d)$. This condition is fulfilled by the following equation:

$$\sqrt{\frac{f}{m}}\frac{d}{v_z} = n\pi - 2\varphi,\ n = 1, 2, \cdots . \tag{5.2}$$

n stands for the number of oscillations performed by the HO or the molecule in the radial direction (Fig. 5.3 shows an example for $n = 1$). In the case of a long resonator and short free-flight zones $L_{FF}/d \ll 1$ and only few oscillations n, φ is small and the inverse tangent required to solve Equation 5.1 for φ can be approximated according to

$$\varphi = \arctan\left(\frac{\rho_0}{v_{\rho,0}}\omega_{\mathrm{HO}}\right) \approx \frac{L_{FF}}{v_z}\omega_{\mathrm{HO}}. \tag{5.3}$$

This result also incorporates the relation $\rho_0 = L_{FF}\frac{v_{\rho,0}}{v_z}$. Reorganizing Equation 5.2 with this result for the constant phase from Equation 5.3 gives:

$$\frac{d + 2L_{FF}}{v_z}\sqrt{\frac{f}{m}} = n\pi.$$

Here, the focal length $L = d + 2L_{FF}$ can be identified and we find

$$L = n\pi v_z\sqrt{\frac{m}{f}}. \tag{5.4}$$

The force constant of a harmonic oscillator, f, is related to its energy, W_{HO}, via

$$W_{\mathrm{HO}}(\rho) = \frac{1}{2}f\rho^2 + C, \tag{5.5}$$

with the constant C. The harmonized AC-Stark potential (Eq. 3.11) has the following form:

$$W_{\text{AC-Stark}} \approx -\frac{\mu MK}{2J(J+1)}|\vec{E}|$$

This is a good approximation for $\frac{h\Delta}{2} \ll \frac{\mu MK}{2J(J+1)}|\vec{E}|$. In the low fields, i.e., at the nodes and the resonator walls, this approximation eventually breaks down, however, the transverse forces at these positions are negligible. With the electric field for the $TE_{1,1,p}$ mode in a cylindrically-symmetric resonator (Eq. 2.57 to 2.59), we find:

$$W_{\text{AC-Stark}} \approx -\mu\frac{MK}{J(J+1)}E_{0,\max}\sqrt{\sin^2\frac{p\pi z}{d}}\sqrt{\left(\frac{J_1(\chi)}{\chi}\right)^2\sin^2\phi+\left(\frac{\partial J_1(\chi)}{\partial\chi}\right)^2\cos^2\phi}. \tag{5.6}$$

Here, $\chi = \gamma_{1,1}\rho/R$. The Bessel functions can be expanded into a Taylor series around $\chi = 0$:

$$J_1(\chi) = \frac{\chi}{2} - \frac{\chi^3}{16} + \mathcal{O}(\chi^5)$$
$$\frac{\partial J_1(\chi)}{\partial\chi} = \frac{1}{2} - \frac{\chi^2}{16} + \mathcal{O}(\chi^4)$$

The second square root in Equation 5.6 can then be approximated to:

$$\begin{aligned}
&\sqrt{\left(\frac{\frac{\chi}{2}-\frac{\chi^3}{16}}{\chi}\right)^2\sin^2\phi+\left(\frac{1}{2}-\frac{3\chi^2}{16}\right)^2\cos^2\phi+\mathcal{O}\left(\chi^4\right)}\\
&\approx\sqrt{\left(\frac{1}{4}-\frac{\chi^2}{16}\right)\sin^2\phi+\left(\frac{1}{4}-\frac{3\chi^2}{16}\right)\cos^2\phi+\mathcal{O}(\chi^4)}\\
=&\sqrt{\frac{1}{4}\underbrace{\left(\sin^2\phi+\cos^2\phi\right)}_{=1}-\frac{\chi^2}{16}\left(\sin^2\phi+3\cos^2\phi\right)+\mathcal{O}(\chi^4)}
\end{aligned} \tag{5.7}$$

The Taylor expansion of Equation 5.7 according to $\sqrt{1-x} = 1-\frac{x}{2}+\mathcal{O}(x^2)$ and omitting higher orders leads to

$$\frac{1}{2}\left[1-\frac{\chi^2}{8}\left(\sin^2\phi+3\cos^2\phi\right)\right].$$

ϕ is the azimuthal coordinate of a molecule in the microwave resonator. The azimuthal force is weak compared to the radial force. Hence, to a good approximation the azimuthal position remains constant during the passage of the microwave lens. The z-dependence, the first square root in Equation 5.6, can be averaged:

$$\frac{1}{d}\int_0^d\sqrt{\sin^2\frac{p\pi z}{d}}dz = \frac{p}{d}\int_0^{d/p}\sin\frac{p\pi z}{d}dz = \frac{2}{\pi}\text{ for all } p\in\mathbb{N}.$$

For the harmonized Stark energy we finally find:

$$W_{\text{AC-Stark,harm.}} = \frac{\mu MKE_{0,\max}}{8J(J+1)\pi}\left(\sin^2\phi+3\cos^2\phi\right)\gamma_{1,1}^2\rho^2\underbrace{-\frac{\mu MKE_{0,\max}}{J(J+1)\pi}}_{=C}$$

If we compare this result to the energy of the harmonic oscillator, Equation 5.5, the constant C and, more importantly, the force constant f can be assigned. With this force constant and the electric field strength, $E_{0,max}$, according to Equation 2.56, we find the focal length, L, of the harmonized microwave lens using Equation 5.4.

$$L = nA(\phi)\frac{v_z}{\sqrt[4]{P_{IN}}}. \tag{5.8}$$

Here, $A(\phi)$ is a proportionality factor that can be written as

$$A(\phi) = \frac{2R}{x'_{1,1}}\sqrt{\frac{m\pi^3 J(J+1)}{2.9\mu MK(\sin^2\phi + 3\cos^2\phi)}}\sqrt[4]{\frac{2\pi\epsilon_0\nu_{1,1,p}V}{Q}} \tag{5.9}$$

The focal length L of the microwave lens is proportional to the longitudinal velocity v_z and the inverse of the fourth-root of the microwave power, P_{IN}. J, K, M are the quantum numbers of a symmetric top molecule, m is the molecule's mass and μ its permanent dipole moment. $\nu_{1,1,p}$ is the resonance frequency of the corresponding $\mathrm{TE}_{1,1,p}$ mode and Q the quality factor of the closed resonator with the inner radius R and length d. $x'_{1,1}$ is approximately 1.8411.

The focusing experiments with ammonia $^{14}NH_3$ molecules (mass 17 u) in the upper inversion doublet component of the ro-vibrational ground state ($J = 1$ and $MK = 1$) in the electric field of the $\mathrm{TE}_{1,1,2}$ mode (resonator 1, see Sec. 5.1 and Tab. 4.1) where carried out with the detection laser intersecting the transverse plane at $\phi \approx 37°$. Then the setup is most sensitive to focusing in the perpendicular ($\phi = 127°, z$) plane. From Equation 5.9 we find $A(127°) \approx 8.1 \times 10^{-3}\,\mathrm{s}\sqrt[4]{\mathrm{W}}$. This proportionality is nicely followed by our experiments, as seen from Figure 5.2(B). It displays the microwave power, P_{IN}, needed to optimally focus various longitudinal velocities v_z, and a fit according to Equation 5.8. Based on the focusing curves displayed in Figure 5.2A, $\frac{v_z}{\sqrt[4]{P}}$ amounts to about $16\,\mathrm{m}(\mathrm{s}\sqrt[4]{\mathrm{W}})^{-1}$, which results in a theoretical focal length of $L \approx 130\,\mathrm{mm}$. Considering the assumption of a harmonic potential, this value is in good agreement with the distance in the experiment of $L \approx 136\,\mathrm{mm}$.

In comparison to lenses for molecules in low-field-seeking states, a microwave lens will have different spherical aberrations. Due to the nature of Stark shifts from an inversion doublet, the Stark potential is not harmonic. This anharmonicity has the largest influence at weak electric fields. In devices that focus molecules in low-field-seeking states, such as electrostatic quadrupoles or hexapoles, these are present on the molecular beam axis, where a large portion of the molecular beam passes through. In the microwave lens for molecules in high-field-seeking states, however, the fraction of the beam that travels close to the axis is in a strong electric field so that the potential mimics a harmonic potential very well.

The focusing properties of the $\mathrm{TE}_{1,1,p}$ mode have some limitations mostly because the electric field is not cylindrically symmetric, which would be the ideal shape of the electric field, but also because of the sinusoidal shape in the longitudinal direction, that effectively reduces the focusing strength due to the field nodes. A better alternative that fixes both issues can be found in the $\mathrm{TM}_{0,1,0}$ mode in a closed cylindrically symmetric resonator. Its electric field is cylindrically symmetric and constant along the longitudinal

direction:

$$|\vec{E}| = E(\rho) = E_0 J_0 \left(\frac{x_{0,1}}{R}\rho\right). \tag{5.10}$$

The disadvantage of this mode is that the resonance frequency is somewhat higher than for low $TE_{1,1,p}$ modes, see also Equations 2.28, 2.29 and Table 2.1. This can be compensated by increasing the size of the resonator (for example $d = 120\,\text{mm}$ and $2R = 9.66\,\text{mm}$) to assure that the resonance frequency of the $TM_{0,1,0}$ mode is at 23.75 GHz. However, a larger resonator brings about a larger volume so that the electric field strength would be lower if compared to low $TE_{1,1,p}$ modes with comparable quality factor and input power. A larger radius, as suggested here, additionally decreases the electric field gradient in the radial direction. If deceleration capabilities are not required, this mode can nonetheless be a suitable alternative.

5.3 Microwave deceleration of $^{14}NH_3$

The polar molecules that travel through the microwave lens are accelerated when approaching one of the longitudinal field maxima and subsequently decelerated when leaving it. This effect can be used to manipulate the longitudinal motion by switching the microwave fields on and off. The time sequences for the essential manipulation modes are explored in Section 4.7. The guiding mode is depicted in Figure 4.17 and the acceleration and deceleration modes in Figure 4.18. In the first set of microwave deceleration experiments with ammonia molecules ($^{14}NH_3$) the open Fabry–Pérot resonator is utilized. In contrast to the closed-cavity design, the open resonator allows for detection within the resonator. Furthermore, it is possible to move the mirrors over a range of centimeters allowing for a good tunability of the resonance frequencies (see also Eq. 2.60).

5.3.1 The open resonator

The first step towards complete motion control in three dimensions is guiding. The almost harmonic potential in the longitudinal direction is employed to keep a packet of molecules confined in the longitudinal direction without changing the mean longitudinal velocity of the packet. This is achieved experimentally by switching the microwave fields such that the losses and gains in kinetic energy of the synchronous molecule cancel each other.

Figure 5.4A shows a guiding measurement for a packet of slow ammonia molecules. The mean output velocity of the Stark decelerator is set to 20 m/s, and the time between the opening of the pulsed nozzle and the firing of the detection laser is scanned. The microwave field is given by the $TEM_{0,0,6}$ mode in the Fabry–Pérot resonator as shown in Figure 4.12. The black trace shows the ammonia density in the detection region depending on the flight time without a microwave field present. The red and the green traces correspond to measurements with a switched microwave field applied. Using the concept of phase angles introduced in Section 4.7, the guiding sequence for the red trace is $\varphi = 45°$ and $\Delta\varphi = 90°$. The green trace represents a measurement with the so-called anti-guiding sequence ($\varphi = 135°$ and $\Delta\varphi = 90°$). These two sequences are in principle identical but the beginning is shifted by a quarter wavelength (see also Fig. 4.12).

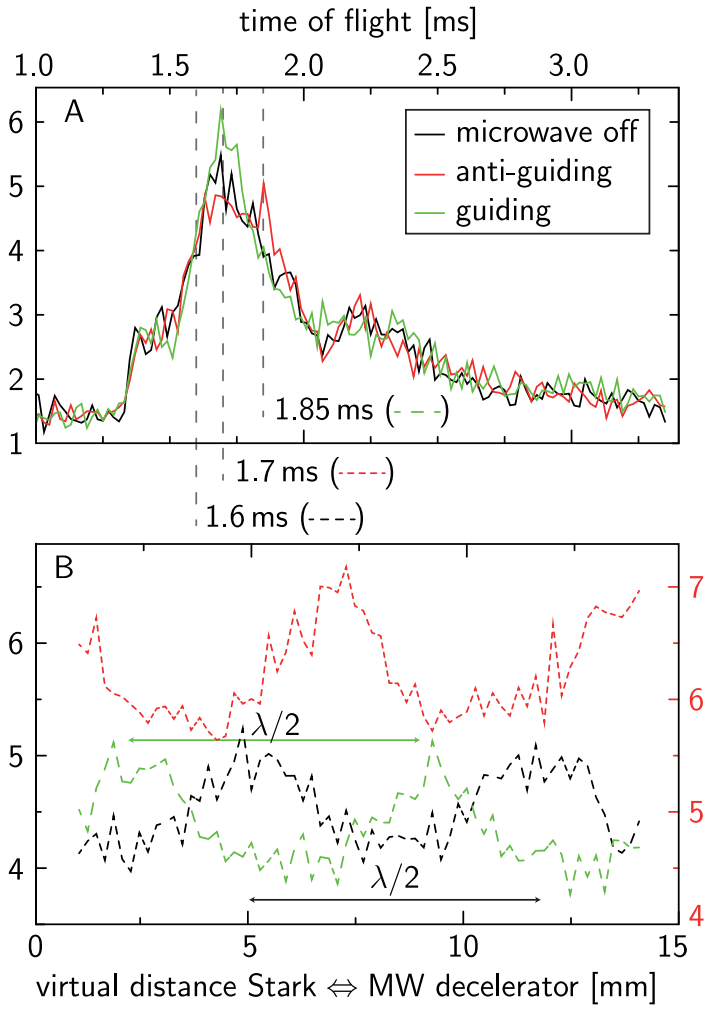

Figure 5.4: The upper panel A shows time-of-flight profiles of ammonia molecules using the open resonator. The Stark decelerator is set to an output velocity of 20 m/s. The lower panel B shows the ammonia density in the detection region at the arrival times indicated in A depending on the time delay between switching-off the Stark decelerator and the beginning of the microwave switching sequence. The red trace is offset by +0.5 arbitrary units for clarity. The signal shows a modulation depending on the structure of the microwave field. The anti-node to anti-node distance of the employed $TEM_{0,0,6}$ mode is $\lambda/2 = 6.6$ mm which resembles the modulation of the molecular density.

All three time-of-flight scans show comparable signal intensities but differ in their shape. The trace designated as *anti-guiding* is slightly longitudinally defocused while the guiding sequence shows a weak longitudinal bunching effect. However, these subtle differences are just above the noise level. To make them more pronounced, a second measurement was conducted with the same molecular beam setting (Fig. 5.4B). In these measurements, the time of flight is kept constant at the values 1.6, 1.7 or 1.85 ms as indicated by the dashed lines in Figure 5.4A. These timings correspond to features in the time-of-flight profile that could be associated with longitudinal bunching or defocusing. Since the two guiding sequences are in principle the same but shifted with respect to each other, i.e., they vary in the start time of the microwave switching sequence, this initial

switch-on time is scanned. Due to the constant longitudinal velocity of the molecules this time can be expressed as a virtual distance between the Stark decelerator and the microwave decelerator. The results are shown in Figure 5.4B. These measurements show indeed an effect of the microwave field that results in a periodic modulation of the signal intensity. This result can be understood as a longitudinal breathing motion of the molecular packet. As the packet is longitudinally bunched and defocused depending on the beginning of the microwave switching sequence, the signal intensity at the different detection times changes. The periodicity of the modulation can be attributed to the $TEM_{0,0,6}$ mode structure in the open resonator ($\lambda/2 = 6.6\,\mathrm{mm}$ is the node-to-node distance in the resonator). Nonetheless, the effect of the microwave field on the molecular motion is very small. This is due to the weak electric fields, $E_0 \approx 1.1\,\mathrm{kV/cm}$ (see also Tab. 4.1), as well as a lack of transverse focusing due to the low electric field strength and the large spot size of the microwave field (see Eq. 2.63) of 26 to 29.6 mm, that results in substantially weaker transverse electric field gradients than in the longer microwave lenses. Furthermore, a crucial part of the detection, the ion extraction of the parent ion, only worked close to the center of the resonator due to disturbances of the static electric field from the metal mirrors. Consequently only the first four of the seven electric field maxima could be used to change the longitudinal motion. In order to overcome these limitations, a second microwave decelerator that is based on the closed microwave lenses was developed.

5.3.2 The closed microwave decelerator

The closed microwave decelerator is based on the design for the microwave lenses, but has a larger diameter of 9.57 mm at room temperature to support the $TE_{1,1,12}$ mode that provides twelve consecutive stages for longitudinal motion control. The smaller resonator volume compared to the open resonator makes it possible to achieve larger electric fields. Moreover, the transverse fields drop to zero on a much smaller length scale (4.785 mm vs. 35 mm in the open resonator), consequently the transverse confinement is substantially better.

In a first series of measurements, the guiding mode is explored: The applied fields are switched such that the net effect of the microwave field on the longitudinal velocity of the synchronous molecule is zero. Due to the shape of the potential (see Fig. 4.17), molecules ahead of the synchronous molecule experience a small net deceleration, while molecules that lag behind are accelerated. That means, the molecular packet is kept confined, both in the transverse and in the longitudinal direction. The results from a time-of-flight measurement using 3 W of microwave power and a packet of ammonia molecules traveling with a mean initial forward velocity of 25 m/s are shown in Figure 5.5.

The upper (green) trace is recorded without a microwave field present. Similarly to the measurements with the microwave lens (Fig. 5.1), there is barely any ammonia signal visible. This is because the cavity length is more than 40 times the aperture diameter in the exit cap, whereas the mean forward velocity only amounts to approximately five times the mean transverse velocity. Consequently, most of the molecules collide with the inner walls of the cavity or the exit cap and do not contribute to the ion signal detected behind the resonator. The second (red), trace is recorded in lens mode, i.e., with the microwave field constantly on. The molecules are transversely confined and a significant

number of molecules arrives in the detection zone.

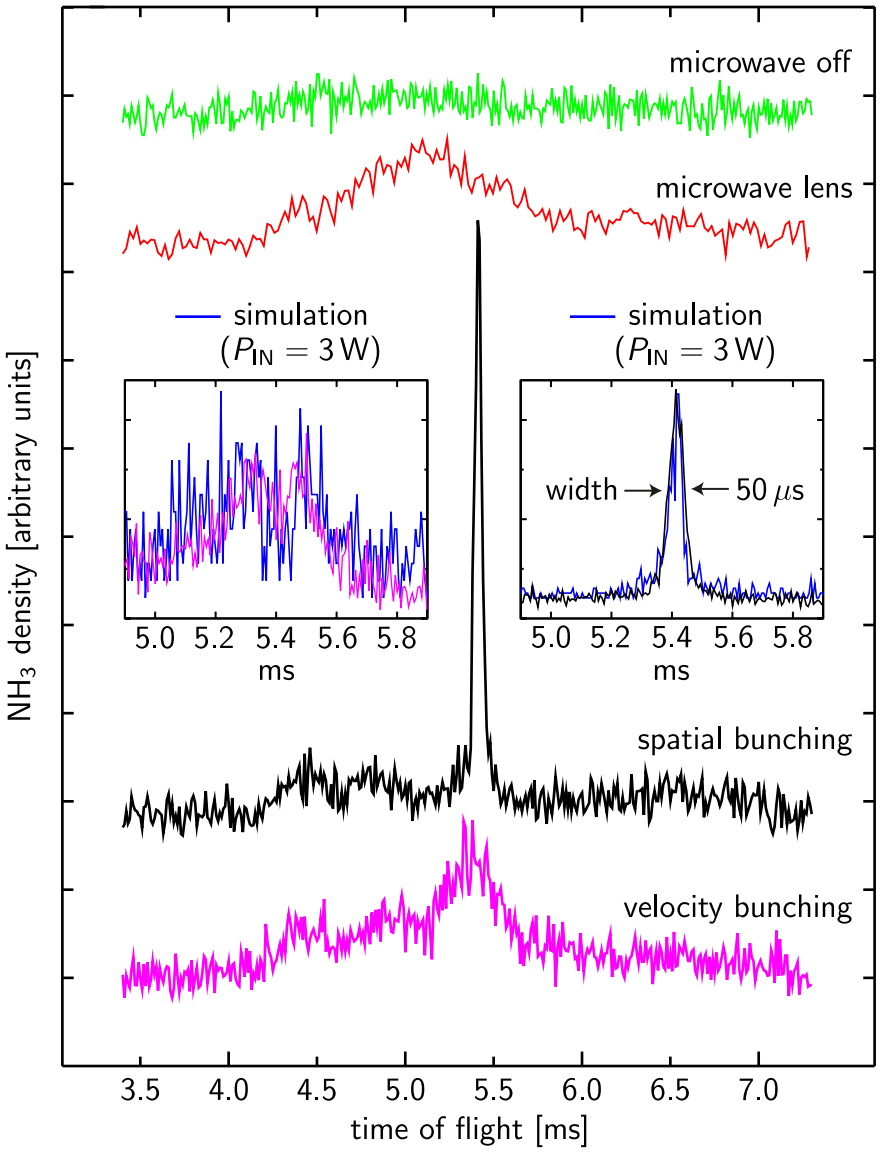

Figure 5.5: Time-of-flight profiles of ammonia packets traveling with a mean velocity of $v_z = 25\,\mathrm{m/s}$. The first trace represents the case without a microwave field present. The second trace is recorded with a constant microwave field applied. The third trace and the left inset show measurements with the regular guiding mode and the bottom and the left inset are obtained with the irregular guiding mode. The insets show a magnification of the time-of-flight traces measured with a higher resolution ($5\,\mu$s vs. $20\,\mu$s) and a comparison with trajectory simulations (blue traces).

The first guiding sequence is displayed in the third trace of Figure 5.5. Here, the microwave field is switched on when the synchronous molecule arrives at the position where the electric field is 50% of the maximum value ($\frac{1}{2}\,E_0$). It is switched off again, when the synchronous molecule arrives at the next position with 50% of the maximum field strength. The potential, as seen by the synchronous molecule, has almost the form

of the negative absolute of a sine function (Fig. 4.17), so that the phase angles of this regular guiding mode are $\varphi = 30°$ with $\Delta\varphi = 120°$. In contrast to the lens mode, this guiding mode produces a very intense and sharp peak in the time-of-flight profile. Two effects are contributing to this shape: transverse focusing in combination with longitudinal focusing which is also referred to as bunching. The longitudinal focusing can be understood by investigating the motion of the packet of ammonia molecules in the longitudinal phase space. The corresponding longitudinal (z, v_z) phase-space data from a trajectory simulation program is shown in the bottom row of Figure 5.6 when the synchronous molecule is at the exit of the Stark decelerator, at the center and at the end of the microwave resonator, and at the detection region. It can be seen nicely that the packet of molecules rotates around the synchronous molecule in its center. The rotation speed depends on the depth/steepness of the almost perfectly harmonic potential. In this spatial bunching experiment, the packet is rotated by almost π and due to the additional free-flight from the last guiding stage to the detection zone, a large fraction of the molecules arrive in the detection region at the same time. In the experimentally observed signal trace, this is reflected by the extremely narrow peak with a temporal width of only 50 μs (Fig. 5.5, third, black, trace and right inset) that corresponds to a temporary reduction of the packet size to circa 1.2 mm. This spatial focus in phase space can also be generated in the velocity or momentum space, the so-called velocity focusing. Experimentally, this can be achieved by rotating the molecule packet in phase space by $(n + 1/2)\pi,\ n \in \mathbb{N}$ (Fig. 5.5, bottom, purple trace).

Velocity focusing is a useful feature for applications such as controlled collision experiments that would benefit from the small kinetic energy spread by an increased collision-energy resolution. Beyond that, continuous loading mechanisms for molecule traps that rely on pumping molecules into a trappable state at the trap center greatly benefit from a small longitudinal velocity distribution. At the maximum microwave input power, the phase-space rotation in a packet with a mean forward longitudinal velocity is close to π. In order to meet the velocity focusing condition the closest options are $½\,\pi$ and $3/2\,\pi$. The latter cannot be realized, since it requires a deeper potential or a longer resonator and the power is already maxed out. The alternative is to perform just a quarter of a full phase-space rotation to comply with the velocity focusing criterion. However, the lower electric field strength as well as using only a few of the available stages results in severe signal loss. As an alternative, the guiding mode was adapted: The switching sequence $\varphi_1 = 0°$, $\varphi_2 = 120°$, $\varphi_3 = 160°$ with $\Delta\varphi_1 = 20°$, $\Delta\varphi_2 = 120°$ and $\Delta\varphi_3 = 20°$ utilizes the potential close to the field nodes in addition to the spatial bunching time sequence. There, the potential is longitudinally defocusing at the cost of phase stability. This guiding sequence effectively accelerates molecules that were initially faster than the synchronous molecule and decelerates those that were initially slower. The central part (in phase space) of the molecular packet stays together. This effect can be seen in the zoom-in on the velocity bunching (bottom, purple) time-of-flight trace (see Fig. 5.5, inset on the left): The time-of-flight profile has a dip in the center, where it is effectively depleted of molecules slightly faster or slower than the synchronous molecule. The smaller velocity distribution goes hand in hand with a broader spatial distribution of the molecule packet. Thus, the temporal width of the peak is significantly increased ($\sim 260\,\mu$s). From the phase-space plot in Figure 5.6, it can be seen that the central part of the molecular packet has a very small velocity spread on the order of 0.5 m/s around

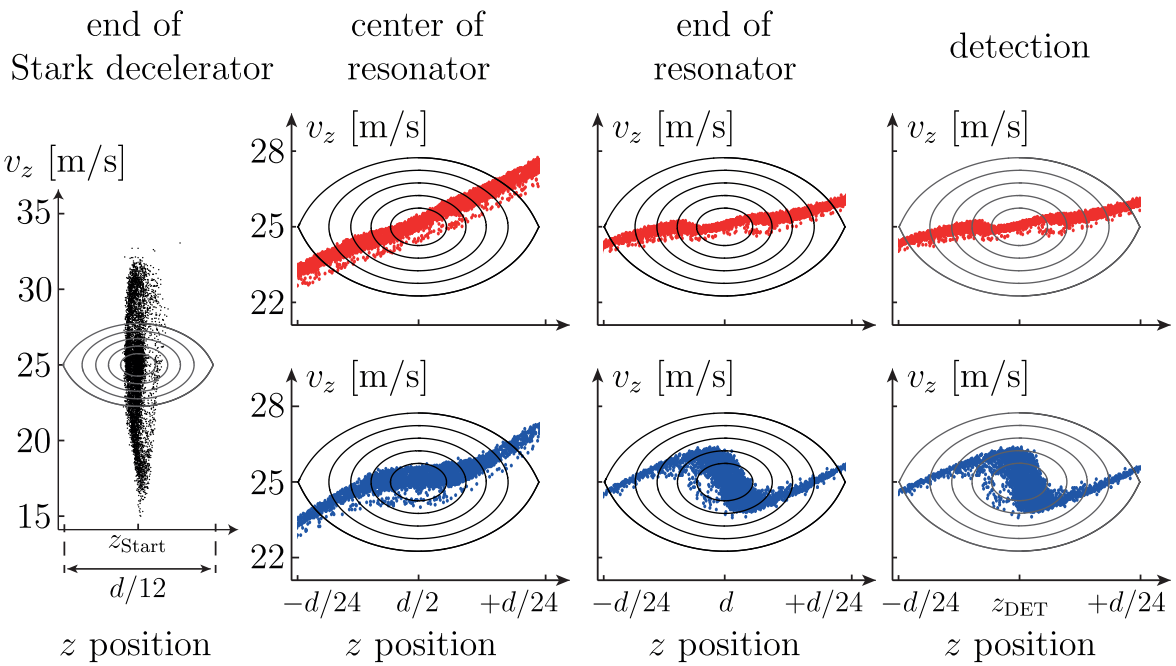

Figure 5.6: Plots of the longitudinal phase space from the trajectory simulations starting from a packet of molecules with a mean velocity of 25 m/s for the velocity bunching or irregular guiding mode (top row) and spatial bunching or regular guiding (bottom row). The longitudinal velocity and the longitudinal position of the molecules in the simulation are shown when the synchronous molecule is at the exit of the Stark decelerator, at the center and the end of the microwave resonator, and at the detection position. The corresponding experimental time-of-flight profiles are shown in Figure 5.5.

the mean longitudinal velocity of 25 m/s. However, it can also be seen that the small velocity spread is only achieved by filtering out the faster and slower molecules. True velocity focusing results in a major fraction of the packet traveling at the same forward velocity as the synchronous molecule. It can only be achieved with a proper phase-space rotation of $(n + 1/2)\pi$. To achieve this, higher field strengths would be required or, as shown later, a lower forward velocity (Fig. 5.8).

Thus, using appropriately switched microwave fields, it is in principle possible to shape a packet of high-field-seeking polar molecules in longitudinal phase space, similar to the phase-space control that can be achieved using a Stark decelerator (shown, for example, in Ref. [177]).

Figure 5.7 shows microwave deceleration, guiding, and acceleration of a packet of ammonia molecules starting from 20 m/s slow ammonia molecules using approximately 3 W of microwave power. The microwave switching sequences all have the same microwave duration of $\Delta\varphi = 120°$ in common, but different starting times. The two top traces (purple, blue) show microwave deceleration measurements with phase angles $\varphi = 60°$ and $\varphi = 45°$. The final mean velocities of the packets of molecules are 16.9 and 18.3 m/s. The middle (black) trace is the $\varphi = 30°$ guiding mode, comparable to the spatial bunching mode shown in Figure 5.5. The bottom traces (red, green) are acceleration measurements with phase angles $\varphi = 0°$ and $\varphi = 15°$. These two modes result in accelerations

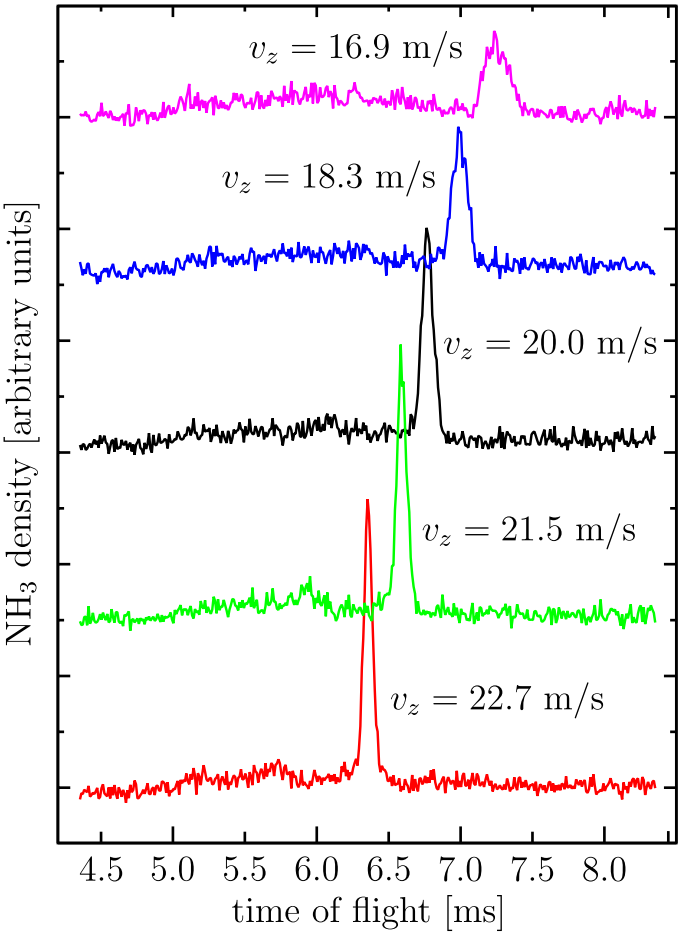

Figure 5.7: Microwave deceleration (upper traces), guiding (middle, black) and acceleration (lower traces) for a packet of ammonia molecules in the $|1,1,a\rangle$-state traveling initially with $v_z = 20\,\mathrm{m/s}$. (The data shown in this figure was published in Ref. [126]).

to 21.6 and 22.7 m/s. The gain or loss in kinetic energy amounts to approximately $h \times 114\,\mathrm{MHz}$ per stage for medium acceleration/deceleration ($\varphi = 15°$ and $\varphi = 45°$) and to approximately $h \times 201\,\mathrm{MHz}$ per stage for strong acceleration/deceleration ($\varphi = 0°$ and $\varphi = 60°$).

Guiding can be extended to lower molecular velocities. Figure 5.8 shows microwave guiding of a 12 m/s slow packet of ammonia molecules for different microwave input powers, P_{IN}. All traces were recorded by applying the same guiding sequence ($\varphi = 30°$, $\Delta\varphi = 120°$). The input power is related to the electric field strength according to $E_{0,\max} \propto \sqrt{P_{\mathrm{IN}}}$ (Eq. 2.55). P_{IN} and $E_{0,\max}$ are indicated on the right side of the traces. The black top trace shows a sharp peak that becomes lower in intensity and temporally wider with decreasing power. Two effects contribute to the power-dependent changes in the time-of-flight profiles. The packet of molecules is transversely less confined when the power and thus the electric field is decreased. That means more molecules collide with the resonator walls, i.e., less molecules arrive in the detection region. This effect is reflected in the integrated traces. Normalized to the integrated signal from the measurement with the highest input power, 3.1 W, we find with decreasing power intensities of $1 : 0.99 : 0.98 : 0.77 : 0.46 : 0.23$ for the different values of P_{IN} (3.1 W, 3.0 W, 2.7 W, 2.4 W, 1.5 W, 1.0 W). Furthermore, the packet changes its shape in the longitudinal direction. This effect is illustrated by the longitudinal phase-space plots to the left and right sides of Figure 5.8. These show the longitudinal coordinates of the molecules that successfully

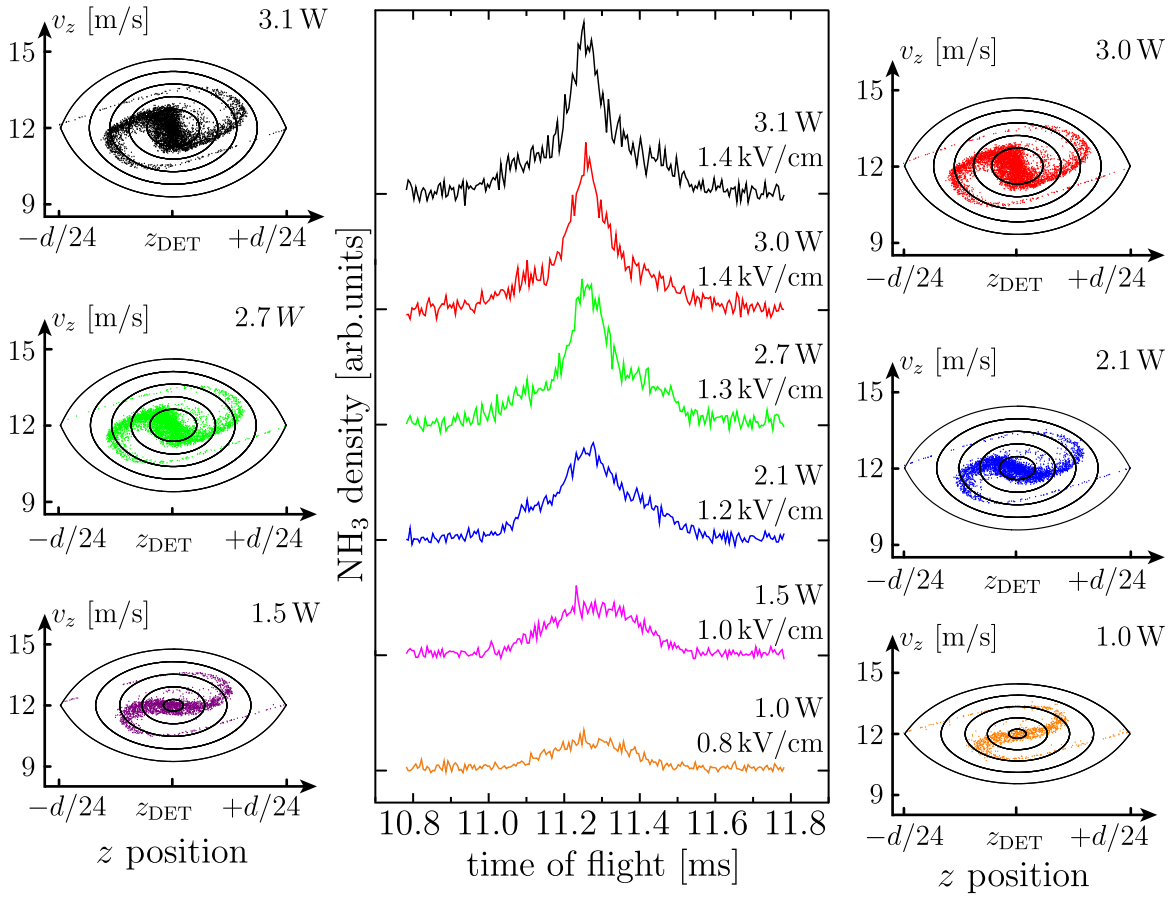

Figure 5.8: Microwave guiding of a 12 m/s slow ammonia packet measured with different microwave input power P_{IN}. The central part shows the time-of-flight data. The traces are offset for clarity. To the left and the right side, the longitudinal phase-space plots from a trajectory simulation are shown. The color code indicates to which time-of-flight trace the simulation output belongs.

exit the microwave resonator when the synchronous molecule is at the position of the detection z_{DET}. The narrowest peak obtained with maximum input power is very close to spatial focusing in the longitudinal direction. With decreasing power the phase-space rotation decreases and the packet becomes spatially wider and thus temporally wider in the time-of-flight trace. A notable case occurs at the input power of 1.5 W, as depicted by the purple trace. There, the phase-space distribution shows a very clear focus in the velocity (momentum) space. The width in velocity-space of the core amounts to less than 1 m/s which is equivalent to a longitudinal temperature of less than 1 mK. This contributes to the fact that the time-of-flight trace recorded with the lowest input power of 1.0 W is narrower again (see also the results for 25 m/s, Fig. 5.5). Another notable feature of the time-of-flight traces from Figure 5.8 are the structures on the sides of the main peaks, in particular the step-like edges that can be seen in the blue and green traces with 2.1 W and 2.7 W input power. These so-called wings are characteristic for complete rotations in the longitudinal phase-space and similarly observed in guiding experiments with Stark decelerators [74]. A factor that contributes to the lower signal

intensities in the wings, if compared to the main peak, is that the molecules in the wing structures experience less transverse confinement than molecules that remain close to the synchronous molecule.

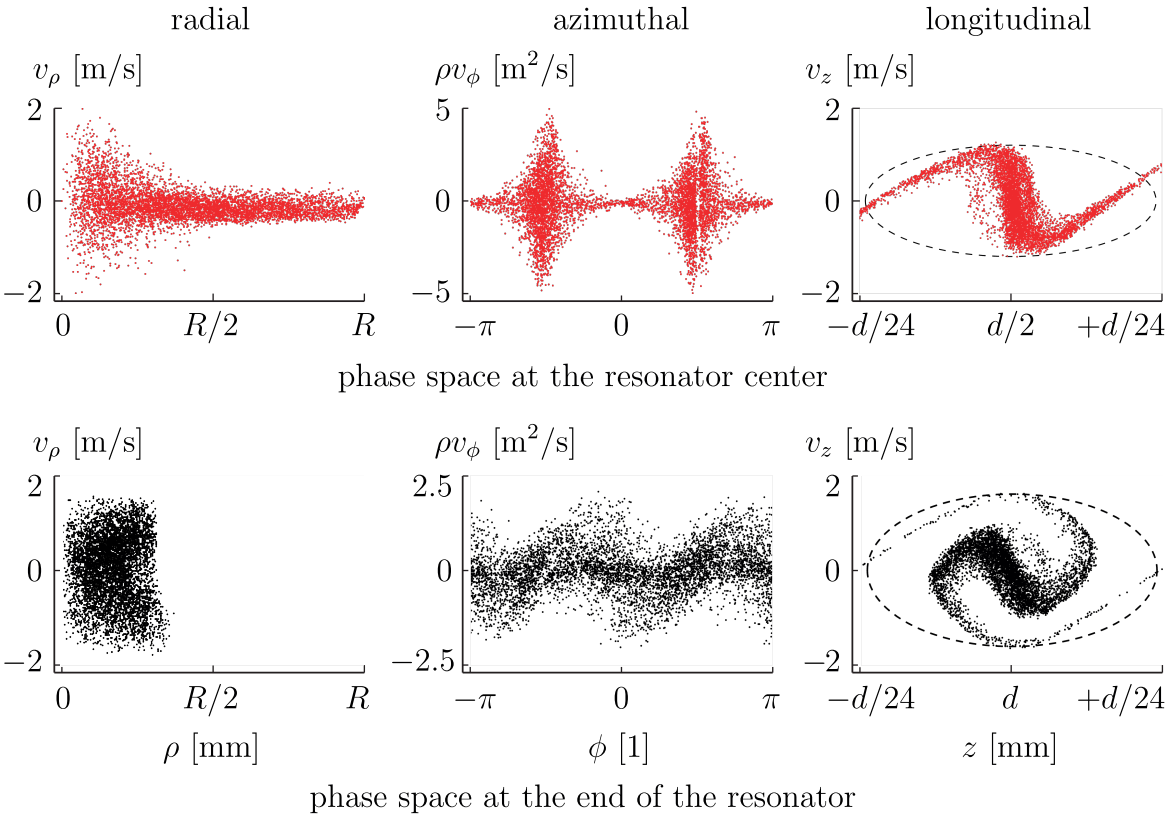

Figure 5.9: Projections of full 6D phase-space from guiding simulations of initially 12 m/s slow ammonia molecules onto the radial, azimuthal and longitudinal phase space. The top row is recorded when the synchronous molecule is at the center of the resonator and the bottom row when it is at the end of the resonator. There, the 3 mm diameter aperture in the exit cap only lets molecules with $\rho < 1.5$ mm pass.

From the 3D trajectory simulations the phase-space acceptance for the guiding mode of the closed microwave decelerator can be estimated. These phase-space plots are shown in Figure 5.9 for maximum input power. The top row illustrates the 6D phase-space distribution of molecules that successfully exit the microwave decelerator when the synchronous molecule is at the resonator center ($z = d/2$) and the bottom row shows this distribution when the synchronous molecule is at the end of the resonator ($z = d$). The three columns are the phase-space projections onto the radial (ρ, v_ρ), the azimuthal $(\phi, \rho^2 v_\phi)$ and the longitudinal (z, v_z) sets of coordinates.

A narrow gap is visible in the azimuthal data at $\phi \approx +\pi/2$ obtained in the center of the resonator . It is the shadow of the antenna. The phase-space projection onto the radial direction at the end of the resonator features a precise cutoff due to the 3 mm diameter aperture in the exit cap.

From these phase-space plots, the full 6D phase-space acceptance volume can be calculated by multiplying the populated areas from each 2D phase-space plot. The spiral

structures of the longitudinal phase-space projections are approximated by ellipses. The elliptical shape is a good approximation to the shape of the actual separatrices obtained from the 1D potential of the synchronous molecule displayed also in Figures 5.6 and 5.8. From Figure 5.9, we find a phase-space acceptance volume of approximately 1500 (mm · m/s)^6. This includes the 3 mm diameter aperture in the end cap of the microwave decelerator. The phase-space acceptance of an AG-decelerator in guiding mode has been estimated in a similar manner for the OH radical in the $^2\Pi$, $v = 0$, $J = 3/2$, $M\Omega = \pm 9/4$ state. OH has the same mass but an about 50% larger permanent dipole moment than ammonia. The AG decelerator described by Wohlfart *et al.* applies a maximum electric field on the order of 140 kV/cm [93]. They estimate a 6D phase-space acceptance volume of 720 (mm · m/s)^6 for the low-field-seeking $M\Omega = -9/4$ state and 620 (mm · m/s)^6 for the high-field-seeking $M\Omega = 9/4$ state [178]. Thus, the microwave decelerator has an approximately two times larger phase-space acceptance for guiding of molecules with similar dipole moment-to-mass ratio but 100 times weaker maximum electric field strength.

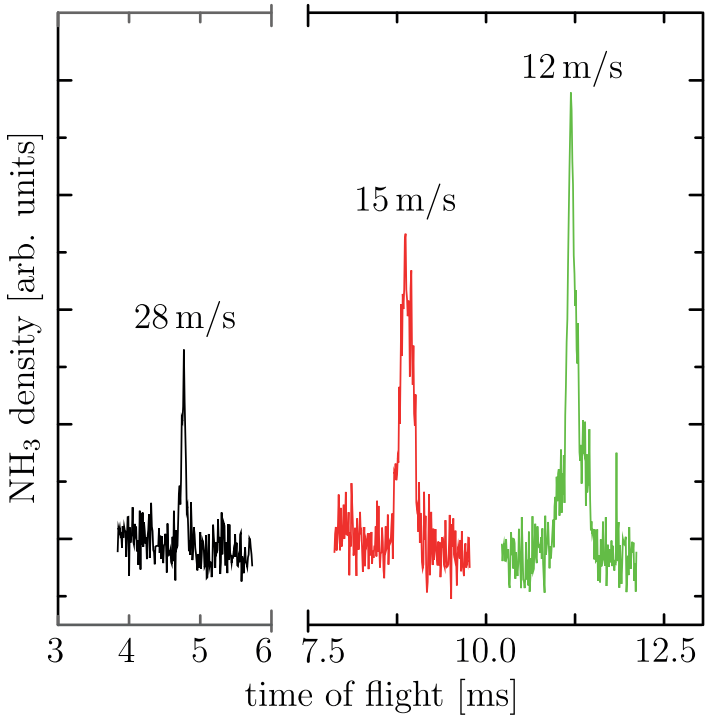

Figure 5.10: Time-of-flight profiles of microwave-guided ammonia packets traveling at longitudinal velocities of 28 m/s, 15 m/s and 12 m/s, respectively.

A comparison of the guiding performance for different longitudinal velocities (12, 15 and 28 m/s) for $P_{\mathrm{IN}} = 3$ W is given in Figure 5.10. The ratio of the numbers of detected molecules using 12, 15 and 28 m/s slow packets, normalized to the most intense peak of the 12 m/s slow molecules, is 1 : 0.93 : 0.42, respectively. The number of detected molecules is lowest for the 28 m/s slow packet (FWHM $\approx 65\,\mu$s). Higher initial velocity reduces the time the molecules spend within the microwave fields, thus reducing the transverse focusing effect. The depth of the microwave trap is $h \times 236$ MHz in z- and x-directions ($\phi = 0$), but only $h \times 96$ MHz in the y-direction ($\phi = \pi/2$) at $P_{\mathrm{IN}} = 3$ W. The

number of molecules per packet traveling at 12 and 15 m/s is comparable. However, under the respective experimental condition we are closer to spatial focusing for the 12 m/s slow packet, resulting in the rather narrow (FWHM $\approx 125\,\mu$s) and intense peak in the time-of-flight distribution. For 15 m/s the obtained peak width is somewhat broader (190 μs).

Figure 5.11 shows microwave deceleration and acceleration measurements starting from a 12 m/s slow beam of ammonia molecules. This way ammonia molecules as slow as 10.0 m/s were produced, which means that more than 20% of the kinetic energy could be removed. All switching sequences (deceleration and both accelerations) share $\Delta\varphi = 120°$. φ is varied from 40° for the deceleration to $\varphi = 10°$ and $\varphi = 20°$ for the two different acceleration sequences. The acceleration experiments result in final velocities of synchronous molecule of 15.1 m/s and 13.7 m/s, which corresponds to a gain in kinetic energy of 58% and 30%, respectively.

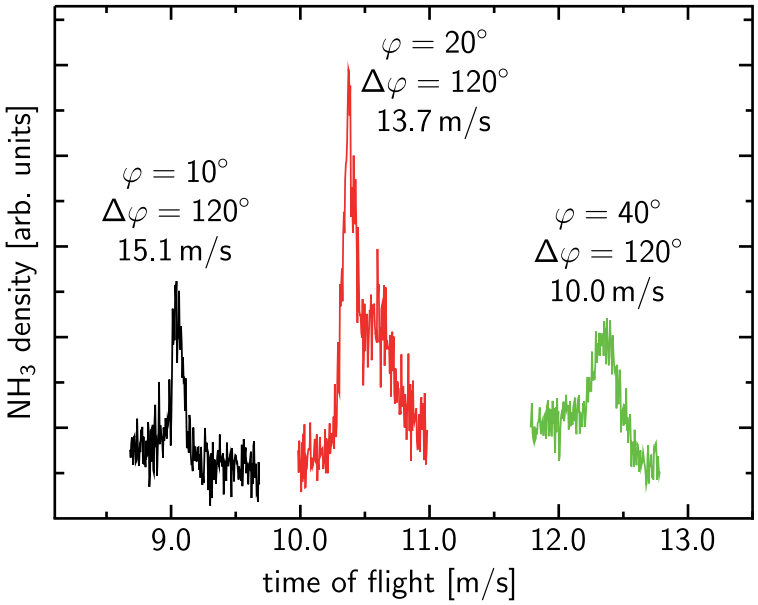

Figure 5.11: Microwave acceleration and deceleration of packets of ammonia molecules traveling with a mean initial velocity of 12 m/s.

For these measurements, the signal intensities for acceleration are much higher than for the corresponding deceleration sequence. From the point of view of kinetic energy, it should be possible to decelerate molecules with an initial velocity of 12 m/s almost to standstill, however, molecules much slower than $v_z = 10$ m/s could not be detected. This almost cut-off like behavior is a consequence of the experimental setup. The detection of the molecules requires their ionization in a focused UV-laser pulse after approximately 10 mm of free-flight behind the last deceleration stage. The emitted packet of molecules has a radial velocity distribution with a full width of 1.5 m/s so that it spreads out significantly. Consequently the number of molecules in the detection volume that is given by the 100 μm diameter of the detection-laser focus is strongly reduced and the very slow molecules cannot be detected. This could be confirmed by trajectory simulations.

5.4 Design study with two resonators

As seen in the previous chapter and especially in Figure 5.11, the setup with a single 119.8 mm long resonator and subsequent external detection zone could be successfully used for prototypical focusing, guiding, acceleration and deceleration experiments, but it also has clear drawbacks. The detection of very slow molecules with $v_z < 10\,\mathrm{m/s}$ cannot be accomplished due to the transverse dilution of the molecular packet. To overcome this limitation at very low longitudinal velocities, it is imperative to move the detection region closer to the resonator. The observation of possible trapping of molecules in one of the potential wells would strongly benefit from detection, i.e., the ionization of the molecule and the extraction of the parent ion, within the closed microwave resonator. Alternatively, the molecules could be re-accelerated as it is often done in moving trap decelerators. The microwave decelerator is based on static traps so that the process of re-acceleration would substantially diminish the detectable molecule numbers. This loss mainly arises from the free-flight distance of at least $d/2p$, which corresponds to approximately 5 mm in the closed microwave decelerator, from the trap center to the next acceleration zone. At the typical velocities on the order of 1–2 m/s, the trajectory-simulations for such an experiment are not particularly promising.

Moreover, the deceleration (acceleration) performance of the single-resonator setup is limited to an extraction (gain) of approximately $h \times 240\,\mathrm{MHz}$ per stage at 3 W input power. In order to remove the Stark decelerator from our setup and achieve pure microwave deceleration of ammonia molecules with an initial velocity of 280 m/s to standstill circa 580 subsequent closed microwave decelerators ($\mathrm{TE}_{1,1,12}$ mode and $Q_L \approx 9100$) would be required. For this, a phase angle of $\varphi = 90°$ and $\Delta\varphi = 90°$ is assumed, which provides the strongest deceleration, however, it also reduces the transverse focusing with respect to the deceleration sequences used in previous measurement (see Fig. 5.7 and 5.11).

The main advantage of the Stark decelerator over the microwave decelerator in terms of deceleration performance is the much higher field strength that can be achieved with static electric fields. In the Stark decelerator a voltage difference of 20 kV on adjacent electrodes corresponds to a maximum electric field strength of 100 kV/cm over the 2 mm gap between the electrodes. In more recent Stark decelerators, the electric field strength can be even higher. The microwave decelerator in its present realization on the other hand has a maximum electric field of approximately 1.4 kV/cm, see also Table 4.2.

The parameters that influence the electric field strength in a closed resonator are shown in Equation 2.55, i.e., the microwave power, the detuning, the quality factor and the resonator volume. An increase of the input power to 15 kW, for instance, would result in a maximum electric field of 100 kV/cm. The microwave frequency used throughout the experiments discussed in this thesis is close to the inversion transition of the rovibronic para-ammonia ground state of 23.695 GHz. However, at this frequency high-power amplifiers are scarce, because the K-band from 18 to 26.5 GHz is not commonly used by radar technology nor telecommunication, mainly because these frequencies are easily absorbed by the water vapor in the atmosphere. In this thesis, a solid-state amplifier with a maximum output power of 10 W was used. Alternative amplifiers like magnetrons, klystrons and traveling-wave tube amplifiers can in principle offer higher output powers of up to tens of kilowatts, however, in the K-band, amplifiers based on

these technologies are very expensive and hardly available. At other frequency ranges, for instance below 18 GHz, such amplifiers generally are significantly cheaper and more common, which is useful for extending the microwave-deceleration technique to larger molecules, as described in Chapter 6.

Another option is an increase of the resonator's quality factor, which requires a higher conductivity of the resonator material as can be seen for example in Equation 2.50. Cooling the resonator can increase the conductivity significantly, as explained in Section 2.11. The closed microwave decelerator already makes use of this effect with an increase of the conductivity by a factor of almost 4 by cooling the resonator from room temperature to 77 K using liquid nitrogen. A larger increase in conductivity can be achieved by using highly-pure oxygen-free copper to manufacture the resonator.

A conductivity increase by orders of magnitude is expected for superconducting materials. In principle, there are materials that show superconductivity at higher temperatures; however these usually ceramic-like substances require a great effort in machining, which makes manufacturing of an actual resonator challenging. So far, it has not been possible to apply high-temperature superconductors to microwave resonators. It is more common to cool them below 10 K using pulse-tube cryostats or liquid helium. In this temperature regime, many materials become superconducting, for instance the metal niobium at temperatures below its critical temperature of $T_c = 9\,K$. Experiments with superconducting resonators were proposed with an open resonator design [123] and a superconducting cylindrical closed resonator plated with a lead-tin alloy for the $TM_{0,1,0}$ and the $TE_{1,1,13}$ modes was realized with a loaded quality factor Q_L of $5 \cdot 10^5$, however, so far no molecular beam manipulation is reported with this particular setup.

The high-Q and the high-power approach are mutually exclusive because state-of-the-art pulse-tube cryostats have strong limitations regarding thermal power loads.

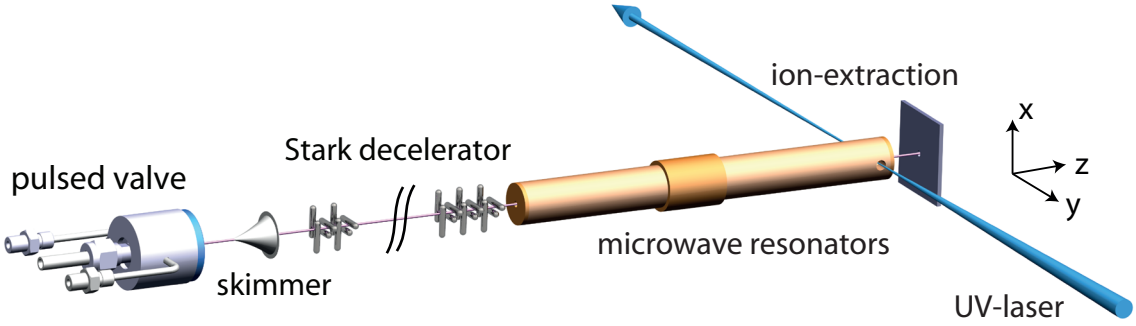

Figure 5.12: Schematic of the experimental setup for a dual-resonator microwave decelerator. In this setup, the second cavity has two small apertures in the wall to allow the ionization of ammonia molecules inside the resonator.

Another feasible approach to increase the electric field strength in the resonator is to reduce the resonator volume, for example by using shorter resonators. A modular resonator design would then provide direct scalability for the required longitudinal and transverse motion control. As a next step we propose a setup with two coaxial resonators with independent 10 W power amplifiers. The setup is shown in Figure 5.12 and is currently tested for feasibility with the prospect of further upscaling. This setup features two resonators made from oxygen-free copper (OFE, 99.99% pure). At room

temperature, the first resonator for the $TE_{1,1,8}$ mode is 79.9 mm long and the second resonator for the $TE_{1,1,10}$ mode is 99.8 mm long. The inner diameter is identical to the closed microwave decelerator: 9.57 mm. The new resonators are connected by a central cap with a 3 mm aperture that is 10 mm long to avoid cross coupling between the cavities. The resonators will be cooled to approximately 77 K with liquid nitrogen flowing through copper tubes that are tightly connected to the resonator. This should improve the cool-down time and make the resonators more stable against thermal drifts. In the former setup, a simple cold finger filled with liquid nitrogen was connected to the microwave decelerator via braided copper wires and hose clamps. The modification with copper tubes makes it possible to change the cooling rate by adjusting the liquid nitrogen flow.

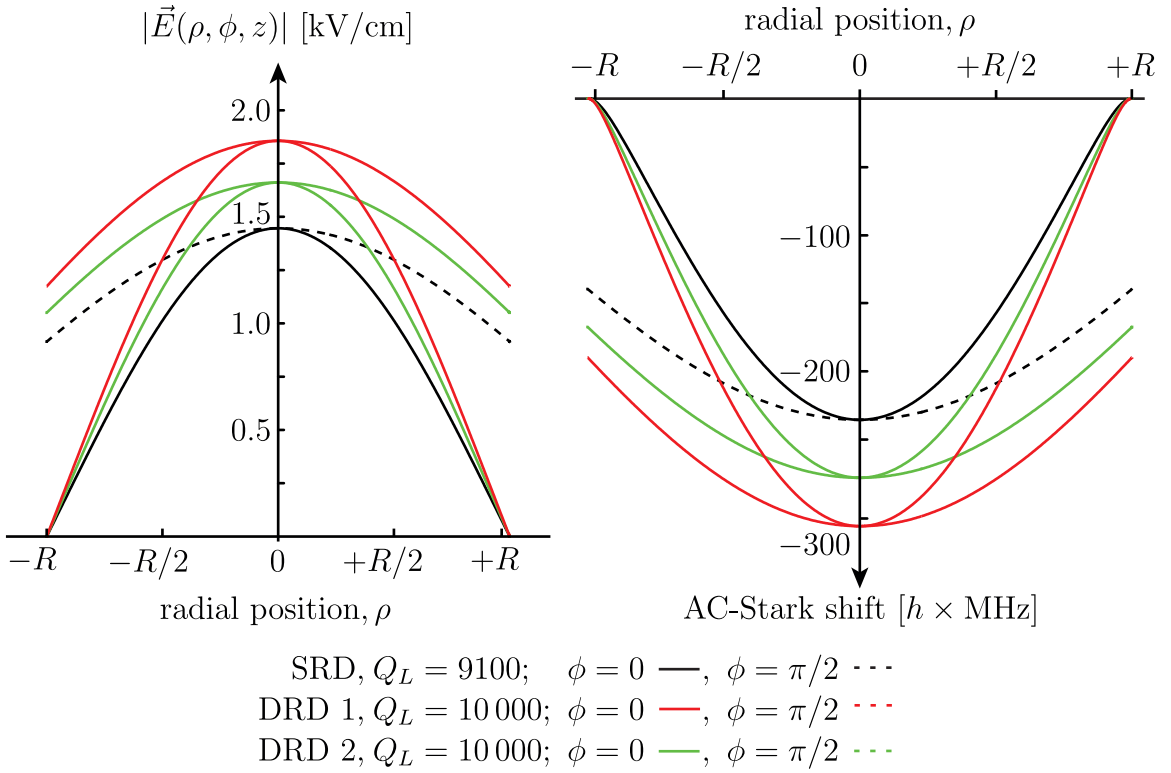

Figure 5.13: Plots of the electric field and the AC-Stark shifts in the SRD ($TE_{1,1,12}$ mode, $d = 119.8$ mm) and in both new resonators DRD 1 ($TE_{1,1,8}$ mode, $d = 79.9$ mm) and DRD 2 ($TE_{1,1,10}$ mode, $d = 99.8$ mm). The dashed lines correspond to $\phi = \pi/2$ and the straight lines to $\phi = 0$. The input power for all traces is $P_{IN} = 3$ W and the detuning for the new resonators is set to $\Delta = 50$ MHz.

The new resonators are referred to as DRD 1 and DRD 2 for dual-resonator decelerator and they are smaller in volume by 33.3% and 16.7% than the previously used closed microwave decelerator (SRD, single-resonator decelerator) . From the full width at half maximum measurement of the resonance, the loaded quality factor of the respective TE mode was determined to be approximately 10 000 when the resonators are immersed and thermalized in liquid nitrogen (~ 77 K). The maximum electric field strength with 3 W of input power can be calculated to be 1.8 kV/cm for the $TE_{1,1,8}$ mode in the 79.9 mm

long DRD 1 and 1.6 kV/cm for the $TE_{1,1,10}$ mode in the 99.8 mm long DRD 2. The electric fields $|\vec{E}(\rho, \phi, z_{an})|$ depending on the radial position in the new resonators (DRD 1 and DRD 2) and the *old* closed microwave decelerator (resonator 3 or SRD) at the longitudinal positions of the antinodes, $z_{an} = d/p \times (n + 1/2)$ with $n = 0, 1, 2, \cdots, p-1$, are compared on the left side of Figure 5.13. The right side shows the expected AC-Stark shifts of para-ammonia molecules in the upper inversion doublet component at the corresponding positions. All curves correspond to $P_{\mathrm{IN}} = 3$ W microwave power, and the straight lines show the $\phi = 0$ direction and the dashed lines the $\phi = \pi/2$ direction. The stronger electric fields in DRD 1 and 2 result in deeper potentials $h \times 278$ MHz and $h \times 313$ MHz compared to $h \times 235$ MHz in the SRD, which is an increase by 18% and 33%, respectively. Thus, the maximum deceleration that could be achieved with the dual-resonator decelerator amount to approximately $h \times 5280$ MHz which is a performance increase by approximately 85% over the single-resonator decelerator.

The main advantage of this setup is the new detection zone. Two 3 mm diameter apertures in the cavity wall at the longitudinal position of the last electric field maximum in the second cavity will provide in situ detection capabilities. Here, the difficulty lies in the extraction of the ions generated by photo-resonant ionization. This can be accomplished by covering the exit aperture in the rear cap with a metal mesh that serves as high-voltage electrode to pull out the positively charged ions. The mesh has to be isolated from the copper resonator by a layer of vacuum compatible electric insulator, such as polyaryletherketone (PEEK). Once outside of the resonator, the ions will be detected using a similar TOF-MS setup as used throughout the experiments described in this chapter.

In Figure 5.14(A), simulated time-of-flight measurements of the single-resonator decelerator (SRD, red trace) and the complete proposed dual-resonator decelerator (DRD, black trace) that consists of DRD 1 and DRD 2 are compared using the regular guiding mode ($\varphi = 30°, \Delta\varphi = 120°$) starting with a Stark-decelerated packet with a velocity of 12 m/s and applying 3 W of input powers. The bottom traces show the number of molecules that *successful*ly arrive at the longitudinal position of the detection zone z_{DET}. They are scaled by 1/10 for clarity. The top traces correspond to the molecules that arrive in the actual detection zone given by the width of the detection laser and would thus be *detected* in the actual experiment. Due to the by 57.5 mm longer distance to the detection zone in the dual-resonator setup, the guided packet arrives at later times. The number of detected molecules in the synchronous packet using the DRD (detected at circa 16 ms) is smaller by approximately 25% if compared to the SRD, which is a consequence of the 10 mm long central cap with a 4 mm diameter aperture. Nonetheless, the ratio of detected to successful molecules in the synchronous packet is favorable in the dual-resonator decelerator. The time-of-flight data obtained from trajectory simulations for the SRD show small additional peaks at 12.5 and 13.6 ms (Fig. 5.14(A)). These originate from trailing molecules that populate the guided packets that follow the synchronous packet, as shown in Figure 5.14(B). These molecules experience less guiding stages than the synchronous packet and consequently the phase-space rotation is smaller. The longer free-flight distance to the detection zone compensates the difference in phase-space rotation, so that also the trailing packets are spatially bunched.

Another advantage of the dual-resonator decelerator over the single-resonator decel-

erator is the overall deceleration performance. Deceleration simulations using the DRD are shown in Figure 5.15. The top three traces represent the actually *detected* molecules and the bottom three (negative) traces depict the *successful* molecules. The bottom traces are scaled down for better visibility and the respective factor is indicated next to the individual trace. The black traces indicate that the $\varphi = 40°$, $\Delta\varphi = 120°$ deceleration mode is applied which decelerated the synchronous molecule down to $v_z = 8.6\,\mathrm{m/s}$. The red traces correspond to the $\varphi = 48°$, $\Delta\varphi = 120°$ switching mode that yields a final velocity of $v_z = 3.8\,\mathrm{m/s}$. In the simulations that correspond to the pair of green traces, the synchronous packet is decelerated even further ($\varphi = 49°$, $\Delta\varphi = 120°$), such that the synchronous molecule is brought to standstill in the last deceleration stage. At this moment, the microwave field will remain switched on and the deceleration stage turns into a trap. Since the synchronous molecule cannot be brought to standstill in the trap center, the packet will oscillate back and forth in the longitudinal direction. The trap center coincides with the detection position so that the motion of the packet can be observed. Consequently two revivals can be seen in the time-of-flight trace. The first detection occurs at the arrival time of circa 27.4 ms at a forward velocity of $v_z = 2.7\,\mathrm{m/s}$. The first revival with negative forward velocity occurs at circa 31.4 ms and the second revival when the trap is finally switched off occurs at 35.6 ms.

These simulations suggest that the observation of microwave trapped ammonia molecules should be possible in the near future utilizing the proposed dual-resonator decelerator.

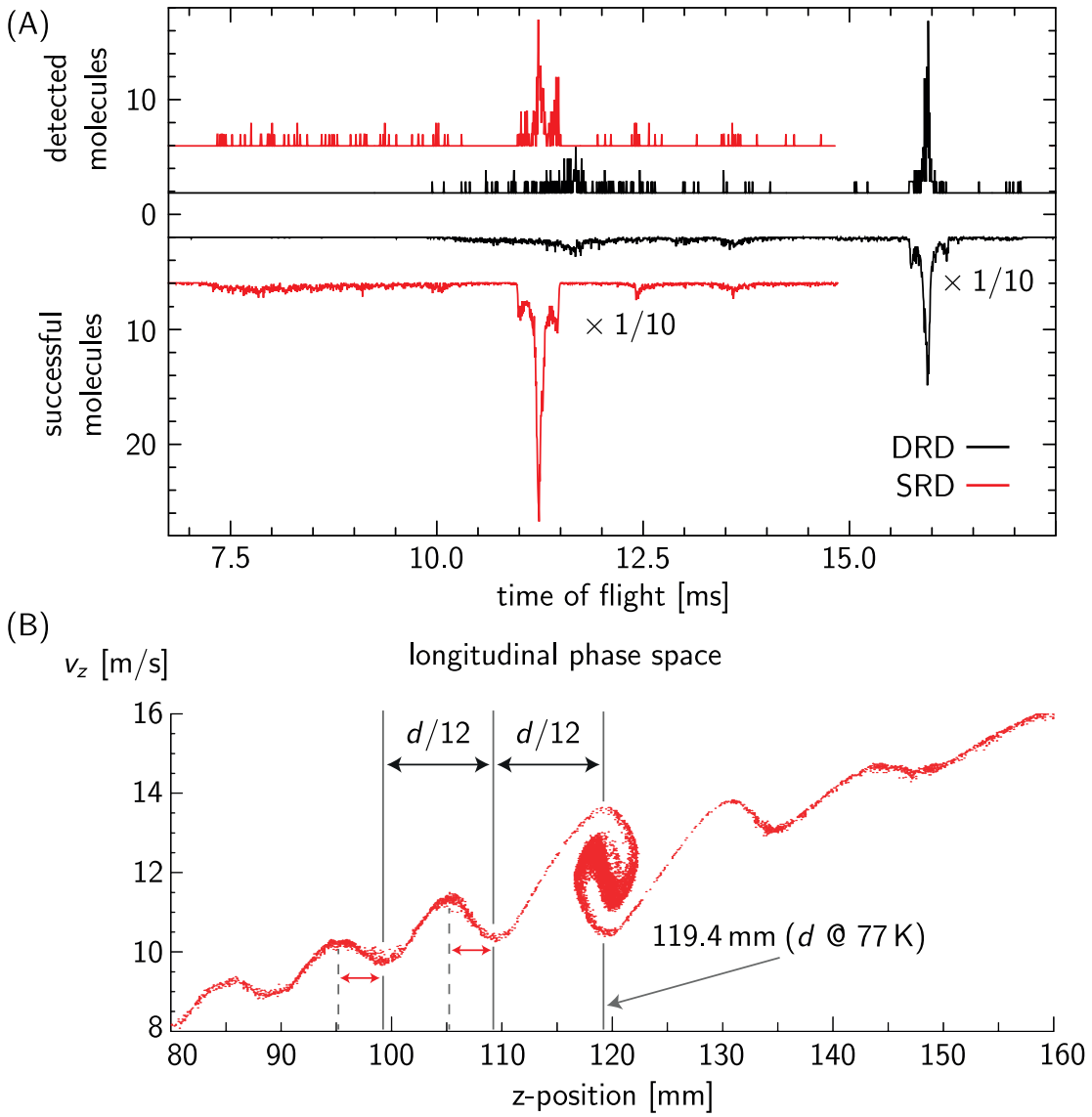

Figure 5.14: (A) Comparison of simulated time-of-flight data using the regular guiding mode ($\varphi = 30°$, $\Delta\varphi = 120°$) of the closed single-resonator decelerator (SRD) with the proposed dual-resonator decelerator (DRD). The top traces indicate the number of molecules that arrive in the focus of the detection laser and the down-scaled bottom traces show the number of molecules that arrive at the z-position of the detection laser. (B) shows the longitudinal phase space for the SRD when the synchronous molecule is at the end of the microwave resonator.

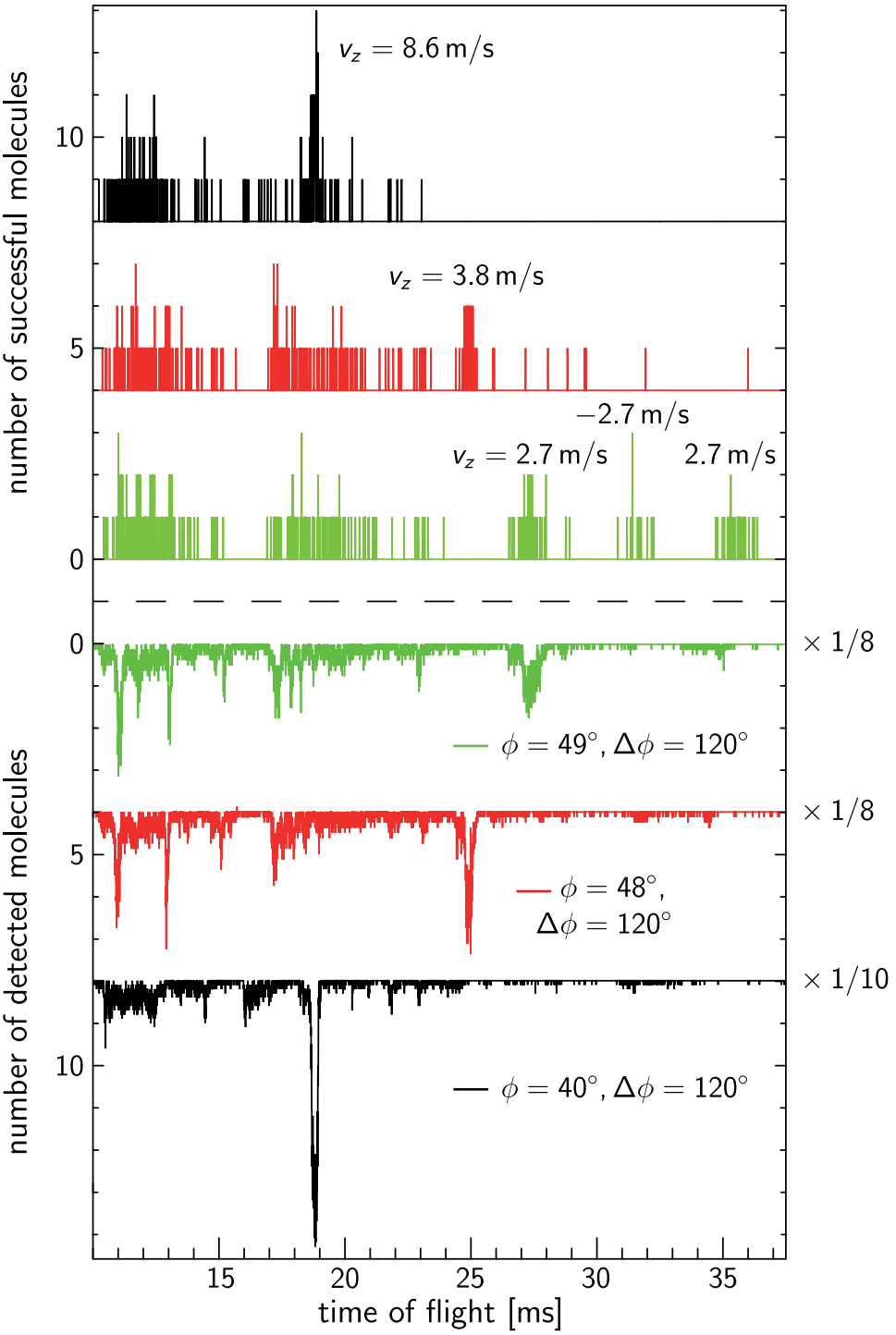

Figure 5.15: Simulated time-of-flight profiles for microwave deceleration using the dual-resonator decelerator. The top three traces represent ammonia molecules that arrive in the detection-laser volume and the bottom three, down-scaled traces represent molecules that arrive at the z-position of the detection. The color code indicates the deceleration mode ($\varphi = 40°$ (black), $\varphi = 48°$ (red) or $\varphi = 49°$ (green), all with $\Delta\varphi = 120°$) that is also labeled next to the bottom traces.

6 Motion manipulation of large(r) molecules

Microwave deceleration is a method particularly interesting for motion control of molecules in high-field-seeking states, where effective techniques are not available to date. The majority of quantum states of medium-sized and larger polyatomic molecules are high-field seeking and already the benzonitrile (BN) C_6H_5CN (13 atoms, mass 108 u) can no longer be Stark decelerated efficiently. The microwave manipulation is a promising tool to provide, for example, slow samples of medium-sized and even large molecules for high-resolution spectroscopy experiments. As a next step towards motion control of medium-sized and large polar molecules, a microwave lens for 4-aminobenzonitrile (4ABN, $H_2NC_6H_4CN$, mass 118.14 u) is currently set up and described in detail in the following section

6.1 A microwave lens for 4-aminobenzonitrile

The 4ABN molecule consists of a benzene ring with an amino, and in para-position, a nitrile group attached. The nitrile group is electronegative and pulls electron density away from the benzene ring, the amino group on the opposite side is donating electron density, which results in a large permanent dipole moment of $\mu_{\mathrm{perm}} = 6.41\,\mathrm{D}$ (see Ref. [179]), which makes this molecule ideal for motion manipulation experiments with AC-electric fields.

4ABN is a solid at room temperature, with a melting point of about $T_M = 83$–$85°C$. Consequently the valve has to be heated to prevent 4ABN from recrystallizing. Thus, the starting velocity of the seeded 4ABN beam will be significantly higher than with NH_3, for which the valve was cooled. Additionally, 4ABN cannot be Stark-decelerated.

To account for the higher initial velocities and thus higher kinetic energy, for effective deceleration and transverse focusing, a deeper AC-Stark potential or a longer microwave resonator is required. This makes the motion manipulation of larger molecules more challenging than with, for example, light ammonia molecules (17 u). As an example: the kinetic energy of an ammonia molecule with a velocity of 20 m/s, a typical final velocity of the Stark-decelerated ammonia packet, is $5.7 \cdot 10^{-24}$ J while a 4ABN molecule at the typical output velocity of a room temperature, supersonically expanded xenon beam of 320 m/s is $1.0 \cdot 10^{-20}$ J. This increase by more than a factor of 1700 in kinetic energy makes significant deceleration of 4ABN molecules ambitious in an experimental setup similar to the one used in previous parts of this thesis (see for instance Chapter 4). As a first step however, transverse focusing should be possible to realize since the transverse velocity components in a supersonically expanded and skimmed molecular beam are much smaller than the longitudinal velocity component (see Sec. 3.2).

A suitable microwave frequency to achieve large AC-Stark shifts for 4ABN molecules is 16.05 GHz. It is blue detuned to the $J_{Ka,Kc} \leftarrow J'_{K'a,K'c}$, $9_{09} \leftarrow 8_{08}$ rotational transition (for the notation see Ref. [162]). Below 18 GHz high-power amplifiers are available and up to 100 W of output power is affordable.

A new, closed cylindrically symmetric microwave resonator that is designed to focus 4ABN molecules is 301 mm long with an inner diameter of 13.23 mm at room temperature. The resonant mode at 16.05 GHz is the $TE_{1,1,18}$ mode, as depicted in Figure 6.1. The 18 longitudinal maxima of the $TE_{1,1,18}$ mode on the resonator axis could, in principle, be extended to the deceleration of 4ABN molecules if a microwave amplifier with several kilowatts of output power would be used (see Chapter 4.7). Deceleration to standstill is, however, not possible with this setup. Even at optimistic field strengths on the order of 20 kV/cm (with $P_{\mathrm{IN}} \approx 730$ W and $Q_L \approx 10\,000$) a maximum total kinetic energy of $2.45 \cdot 10^{-23}$ J can be extracted, which is only a small fraction of the kinetic energy of the 4ABN molecules.

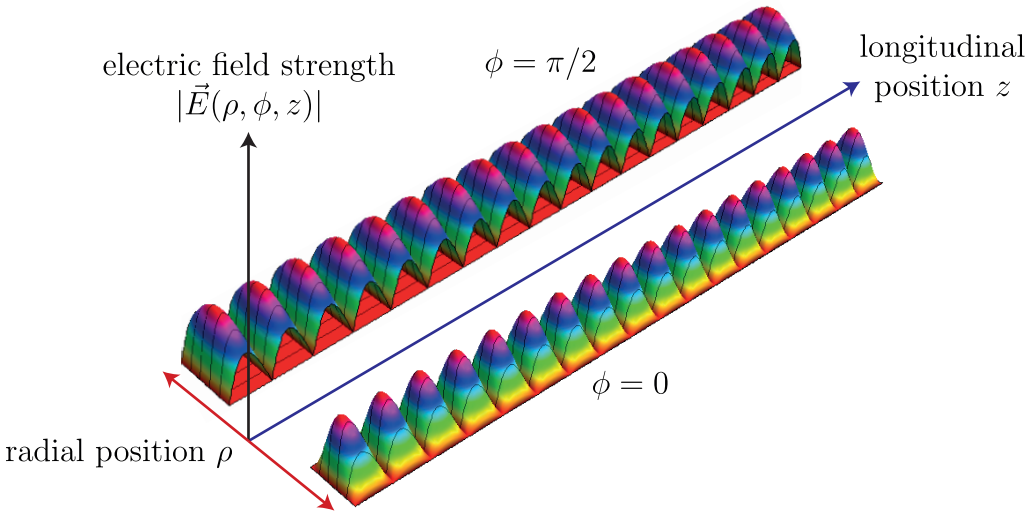

Figure 6.1: Electric field distribution, $|E(\rho, \phi, z)|$, depending on the position in the (ρ, z)-plane with $\phi = 0$ (bottom) and $\phi = \pi/2$ (top) for the $TE_{1,1,18}$ mode in the microwave lens for 4ABN. The 301 mm long resonator has an inner diameter of 13.23 mm at room temperature. The 3D plot are scaled with a diameter to length ratio of 2:1.

For the deceleration to very low velocities or even trapping of larger molecular species, a change of the molecular beam source that generates molecules with lower initial kinetic energy would be required. For this, the prospects of buffer-gas cooling as an alternative molecular beam source were investigated (see also Chapter 1 and Ref. [42]). These experiments were carried out in the group of Prof. John Doyle at Harvard University under the supervision of Dr. David Patterson during an extended research stay and are summarized in the following section.

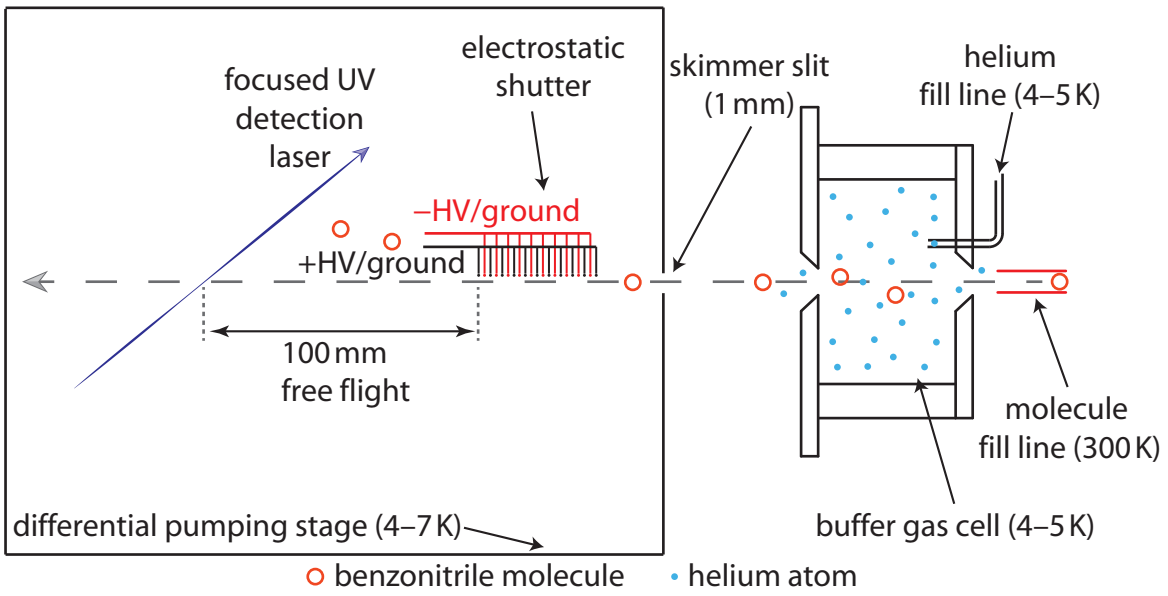

Figure 6.2: Schematic (side view) of the buffer gas cell (right) with the electrostatic shutter and the LIF detection zone in the differential pumping stage (left). The skimmer slit is scaled up for clarity.

6.2 A buffer-gas beam of benzonitrile

Figure 6.2 shows a schematic drawing and Figure 6.3 a photograph of the experimental setup used for these buffer-gas beam experiments. A 77 K shield, i.e., a large aluminum box, which can be seen in the background of Figure 6.3 surrounds the molecular beam apparatus. It minimizes black body radiation from the vacuum chamber as well as heat loads to the cryogenic buffer-gas cell. This cell is shown on the right side of Figures 6.3 and 6.2. It is a 50.8 mm long copper cylinder with an inner diameter of 63.5 mm cooled down to 4–5 K by a pulse-tube cryostat (Cryomech). Helium continuously flows into the cell from a cold fill line and thermalizes due to collisions with the cold cell walls. Two 10 mm apertures, in the front and the back walls, allow hot ($\sim$ 300 K) benzonitrile molecules to enter, and the cold molecular beam to exit the buffer-gas cell. A special feature of this particular setup is the molecule feed line [49, 180] that is not connected to the cryogenic cell, in contrast to previous setups with large molecule species [181]. This makes it possible to use a large diameter feed line at room temperature, ideal for medium-sized molecules such as benzonitrile, while minimizing heat loads to the cryostat. Within the cell, the hot molecules thermalize via collisions with the cold helium atoms. The number of collisions that occur on the timescale that the molecules spend in the cell can be tuned by the helium density: the density has to be low enough so that the hot molecules can enter the cell against the outgoing helium stream but high enough to ensure enough collisions (10s to 100s) to cool the rotational and translational degrees of freedom. Cooling of the vibrational degrees of freedom is the least efficient process. In this setup, the ideal density is on the order of $n_{\mathrm{He}} \approx 4 \cdot 10^{14}\,\mathrm{cm}^{-3}$, corresponding to a helium flow of about six standard cubic centimeters per minute (sccm) into the cryogenic cell.

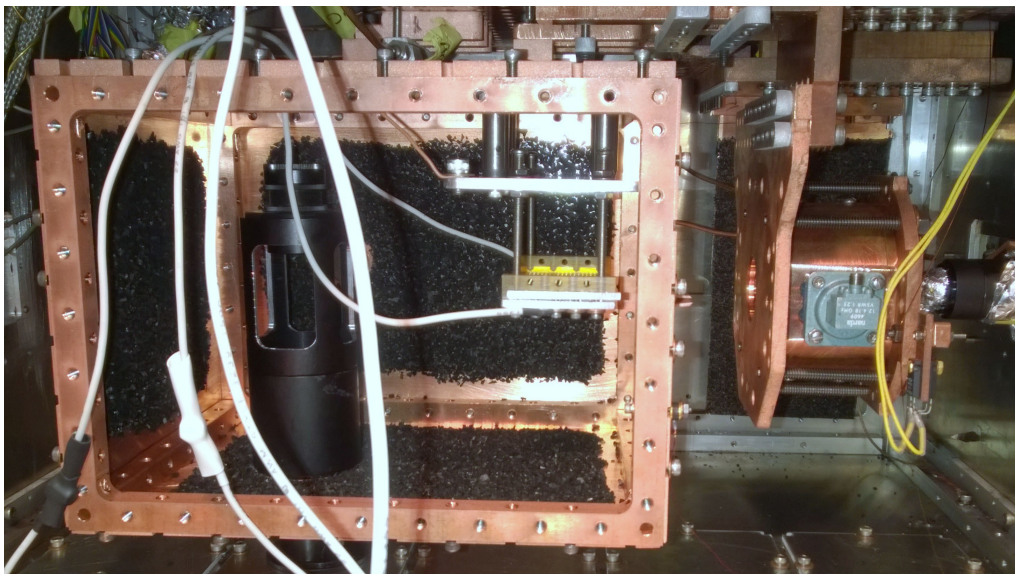

Figure 6.3: Picture (lateral view) of the buffer gas cell (right) with the electrostatic shutter (center) surrounded by the copper box that is coated by charcoal to increase the vacuum in the molecular beam region. The molecules enter this differential pumping stage through a 1 mm skimmer slit (visible on the right side of the copper box). The optics tower to the left reduces stray light to assure low noise on the photon-multiplier tube.

The beam of atoms and molecules is emitted from the exit aperture into a cryogenically pumped vacuum chamber. The particle densities decrease rapidly and at the subsequent skimmer slit, 50.8 mm downstream from the cold cell, the helium density is reduced to less than 10^{12} atoms per cm^3. The density of cold molecules at this point is on the order of 10^10 per cm^3. That means the mean free path of the molecules is far larger than the length scale of the experiment and no collisions with particles from the beam are expected.

During operation, all copper parts shown in Figure 6.3 are cooled to about 4 to 5 K. Cryogenic pumping is achieved by layers of activated charcoal on copper sheets that are cooled to 5–7 K. Below 8 K the activated charcoal acts as a powerful sorption pump even for the very volatile helium atoms. Above this temperature, the helium starts to desorb, which initiates a chain reaction since the pressure build up increases the heat load causing even more helium to boil off.

The benzonitrile molecules are detected by laser-induced fluorescence (LIF) using 278 nm UV photons from a Nd:YAG-pumped optical parametric oscillator (Quanta Ray Indi, Versa Scan and UV Scan, all Spectra Physics) that delivers 1 mJ per pulse at a repetition rate of 10 Hz. The fluorescence photons are subsequently detected using simple collection optics (two subsequent collection lenses) and a photomultiplier tube (PMT, Hamamatsu Photonics).

Regarding the feasibility of generating a buffer-gas beam for subsequent microwave manipulation, the velocity distribution of the beam is studied. In a previous experiment with the same buffer-gas cell, the forward velocity distribution was obtained by

Fourier-transform microwave spectroscopy of benzonitrile molecules and the analysis of the Doppler splitting of the $F = 5 \leftarrow F = 4$ hyperfine transition. The peak of the distribution was determined to be $v_z = 67 \pm 5\,\mathrm{m/s}$ [49]. Here, we developed an alternative approach to measure the velocity via changes in the beam intensity depending on the molecule's arrival time. Such a time-of-flight measurement requires rapid switching (on and off) of the continuous molecular beam. This is achieved by an electrostatic shutter, a linear electrode array that consists of 21 parallel 115 mm long and 1.1 mm diameter steel electrodes, perpendicular to the molecular beam. The electrode to electrode spacing amounts to 1.1 mm, and the shutter is positioned 76.2 mm downstream from the buffer-gas cell. The electrostatic shutter is shown in the Photograph 6.3 and schematically in Figure 6.2. The even electrodes are set to −6 kV and the uneven ones to +6 kV (see Fig. 6.2 and 6.3) provided by Bertan Mod205B-10R power supplies. The high voltages can be switched to ground and vice versa within a few nanoseconds by Behlke push-pull high-voltage switches. A delay generator, DG535 by Stanford Research, controlled by the data-acquisition software provides the relevant relative timings between the detection laser and the trigger for the high-voltage switches.

Most quantum states in benzonitrile are DC-high-field seeking (see also Sec. 3.3) at electric fields of more than a few kV/cm which leads to a deflection of the molecules from the molecular beam axis when the shutter is switched on.

Preliminary experiments using two skimming slits, the first 51.4 mm downstream from the buffer-gas cell and the second right in front of the detection position, were unsuccessful with almost no benzonitrile intensity in the detection region. This circumstance could be ascribed to a large helium background pressure in the vacuum chamber. To achieve a true collision-free flight of the benzonitrile molecules, the differential pumping stage was installed. It is an additional copper box, with the walls covered in activated charcoal. The box has only small openings for the detection laser and the collection optics and the molecules to enter through a 10 cm wide skimmer slit with a height of 1 mm. This way, only molecules with a small transverse velocity component in the vertical direction partake in the actual time-of-flight experiment. Consequently the relevant molecules pass the electrostatic shutter very closely to ensure a strong deflection when the shutter is switched on.

The electrostatic shutter is set to high voltage at the origin of time of Figure 6.4A. Molecules that pass the electrostatic shutter after this time are deflected due to the interaction of the molecule's dipole moment with the electric field (DC-Stark effect) and the molecule intensity in the detection region drops by about 45% after 2.5 ms, see Figure 6.4A. Longer detection delays showed no significant further signal decrease. The distance from the shutter to the detection zone is circa 100 mm so that the detection delay can be translated into molecule velocities, as shown in Figure 6.4B. Since the overall length of the shutter amounts to circa 45% of the free-flight distance, the accuracy of this calculated velocity is limited and could be substantially larger.

In Figure 6.4C, the relative intensities of the longitudinal velocity components in the beam are illustrated. These can be obtained by the differential quotient of the discrete values from the previous panel. The peak of the velocity distribution is at circa 80 m/s.

The peak value of the velocity distribution obtained by the previous study using Fourier-transform microwave spectroscopy [49] is 67 ± 5 ms. The value obtained via time-of-flight measurement is larger, however, the uncertainty of the determined peak

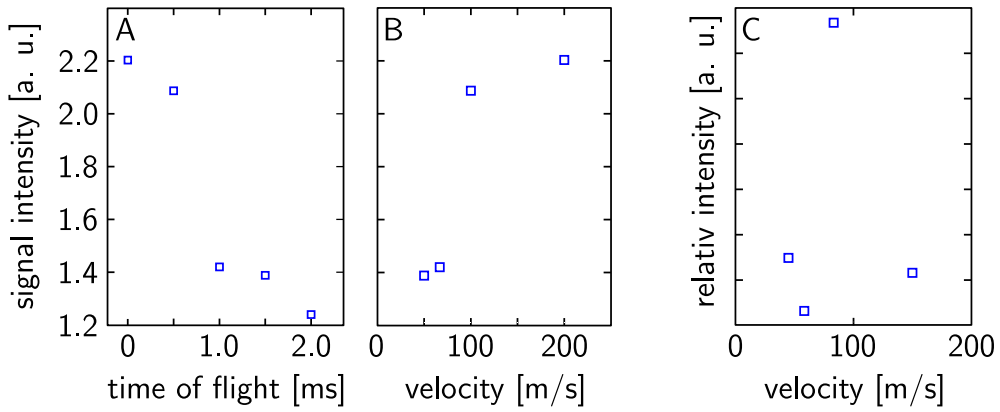

Figure 6.4: Time-of-flight measurement of the molecular beam from a buffer-gas cell using a 21-electrode electrostatic shutter. Panel A shows the LIF signal intensity depending on the time delay after the shutter is switched on from 500 μs to 2.5 ms. The signal drops by about 45% after 2.5 ms with respect to the undisturbed beam. The distance from the shutter is 100 mm; hence, the time delay can be expressed as a molecule velocity as depicted in Panel B. Panel C shows the relative intensities of the different velocity components in the beam with a maximum at circa 80 m/s.

position of the velocity distribution is rather large (± 20 m/s, Fig. 6.4C) due to the low number of measured time delays (Fig. 6.4A and B). At this point, these two results are in good agreement, but if the additional uncertainty ($+36$ m/s) due to the possibly inaccurate velocity determination is considered, the difference in the obtained peak values from microwave spectroscopy and time-of-flight measurement would be even larger. This could mean that the effective length of the shutter extends just over a few of the last electrodes, so that this uncertainty is actually significantly smaller than 45%. An experiment with a shorter shutter (2–3 electrodes) could resolve this issue.

In any case, the peak value obtained for the forward molecular velocity distribution is much lower than in a supersonic expansion, even if the heavy seed gas xenon is used (~ 300 m/s). The molecule densities just outside of the buffer-gas cell are approximately 10^{11} cm^{-3}. The aperture diameter is circa 1 cm^2 and the density drops as L^{-2} with the distance from the source L. For further microwave motion manipulation experiments just a few centimeters downstream from the source, a total molecule density on the order of 10^{10} cm^{-3} is to be expected. In benzonitrile at the typical temperature of a buffer-gas beam of approximately 6 K many (~ 500) rotational states are populated, see also Figure 1.3. Consequently about 10^7 molecules per cm^3 can be expected in a single quantum state. This value is on the same order of magnitude than the density of ammonia molecules in $|J, K\rangle = |1, 1\rangle$ upper inversion doublet component behind the Stark-decelerator used in the microwave manipulation experiments described this thesis.

The molecule densities and the relatively low initial molecule velocities make the buffer-gas cell a sustainable alternative beam source for microwave manipulation experiments.

In the next section, a simple generalization of the two-level dressed-state picture used in Section 3.4 in the case of ammonia to the many-level case is presented. This is an important tool that allows for fast zeroth-order AC-Stark shift calculations for large(r)

molecules where usually no isolated two-level system can be found in the microwave region.

6.3 AC-Stark effect

Shifting the focus of the sample species from highly symmetric small molecules such as OH and NH_3 to medium-sized and larger polyatomic molecules requires a feasible approach to calculate the AC-Stark shifts of these molecules in a microwave field.

The energy differences between rotational levels of these molecules are typically in the microwave domain, which is beneficial for finding microwave frequencies that exert a strong force on the polar molecules. However, due to the large density of states which comes along with the large moments of inertia and thus small rotational constants and due to the loss of symmetry, calculating the AC-Stark shifts becomes increasingly complex.

We propose a zeroth-order calculation method based on the dressed-state approach (see also Sec. 3.4). Then the total Hamiltonian $\mathcal{H}$ of the system is in analogy to Equation 3.9:

$$\mathcal{H} = H_{\text{rot.}} + H_{\text{AC-Stark}} + H_{\text{EM}}, \tag{6.1}$$

with the pure rotational Hamiltonian $H_{\text{rot.}}$, the Hamiltonian of the quantized electromagnetic field $\mathrm{H_{EM}}$ and the interaction between the field and the molecule $H_{\text{AC-Stark}}$.

In the simplest approximation, the same formulas apply as presented in Section 3.4 for ammonia molecules, i.e., in a two-level system. The energy eigenvalues are the so-called quasi-energies ϵ that in zeroth-order approximation are the unperturbed field-free states of the molecule dressed with m photons of the microwave field ($\hbar\omega$): $\epsilon = E_n + m\hbar\omega$.

In contrast to ammonia, the interaction of a larger asymmetric top molecule, such as 4ABN, with a microwave field can no longer be understood as a two-level system, but rather a multi-level system due to the higher density of states. Consequently, more levels are mixed in a strong microwave field.

The Hamiltonian for the zeroth-order AC-Stark effect can be displayed as a $2N \times 2N$ matrix, if only coupling between next neighboring ladders, i.e., ladders that differ in photon number by $\Delta m = \pm 1$, is considered. N is the number of rotational states.

$$\mathcal{H} = \left(\begin{array}{ccc|ccc} E_N + m\hbar\omega & 0 & \cdots & 0 & \cdots & 0 \\ 0 & \ddots & 0 & \Omega_{n,n'} & 0 & \vdots \\ \vdots & 0 & E_0 + m\hbar\omega & \Omega_{n,n'} & \Omega_{n,n'} & 0 \\ \hline 0 & \Omega_{n,n'} & \Omega_{n,n'} & E_N + (m+1)\hbar\omega & 0 & 0 \\ \vdots & 0 & \Omega_{n,n'} & 0 & \ddots & \vdots \\ 0 & \vdots & 0 & \vdots & 0 & E_0 + (m+1)\hbar\omega \end{array}\right)$$

Similarly to calculating the AC-Stark shift of ammonia, the coupling $\Omega_{n,n'}$ between the quasi-energy levels with $\Delta m = \pm 1$ in a linearly polarized microwave field can be calculated from the transition dipole moments $\mu_{n,n'}$ according to

$$\Omega_{n,n'} = \frac{\mu_{n,n'}}{2}|\vec{E}|. \tag{6.2}$$

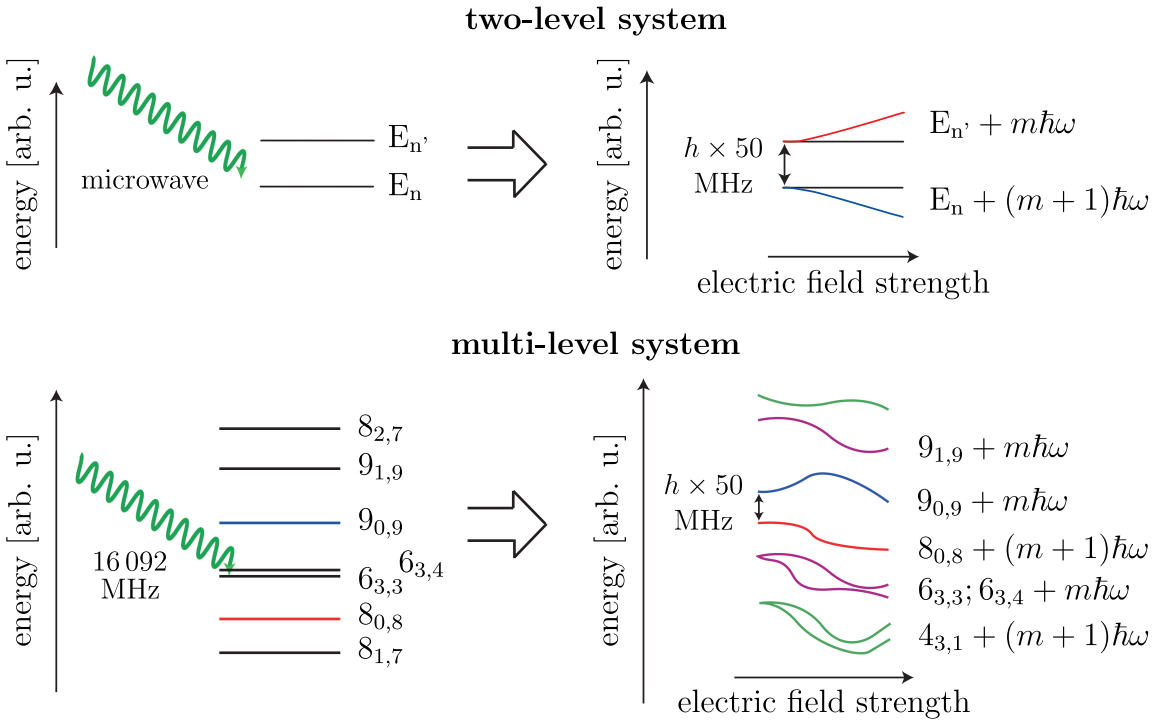

Figure 6.5: Illustration of the AC-Stark shift exhibited by a two-level system, such as ammonia in the rovibronic ground state, in contrast to a multi-level system, for example 4-aminobenzonitrile (4ABN). The left side shows the unperturbed level structure at zero electric field and the right side represents the level structure of the states dressed with microwave photons of $\hbar\omega = 16.042\,\mathrm{GHz}$ as a function of the electric field strength within the zeroth-order dressed-state approach. The 4ABN states are labeled according to $J_{Ka,Kc}$.

This dressed-state matrix approach is particularly useful for AC-Stark shift calculations because the required information, i.e., the transition dipole moments and the unperturbed energy levels E_n, for 4ABN or benzonitrile, for example, can easily be extracted from widely available rotational spectroscopy prediction and fitting programs such as PGOPHER [11] or SPCAT [182]. They can also be calculated directly using the direction cosine matrix elements of modified symmetric top rotor wave functions as described in References [162, 163].

Finally, the Hamiltonian has to be diagonalized to obtain the quasi-energy levels of the mixed states in the microwave field. This can be accomplished numerically for very large systems with moderate computation power. A converging result for the AC-Stark shift calculation of the $J'_{K'a,K'c} \leftarrow J_{Ka,Kc} = 9_{09} \leftarrow 8_{08}$ rotational states in aminobenzonitrile, for example, requires a total number of included states up to $J = 15$. This corresponds to a $11\,000 \times 11\,000$ matrix that can be diagonalized with a normal desktop PC in a few hours.

7 Conclusion and outlook

In the framework of this thesis, motion manipulation of neutral ammonia molecules was demonstrated using resonator-enhanced microwave radiation. This method allows the manipulation of polar molecules in high-field-seeking states, for which no reliable technique was available so far. As such, it is thus particularly useful for applications with molecular ground states and larger polyatomic molecules.

As a first set of devices, two microwave lenses were constructed. These are 120 mm long cylindrical copper resonators with slightly different inner diameters close to 7.4 mm that support the $TE_{1,1,1}$ mode and the $TE_{1,1,2}$ mode, respectively. In both resonators, the mode of interest is blue detuned from the inversion transition in the para-ammonia rovibronic ground state by approximately 50 MHz. With these microwave lenses, clear focusing of a molecular packet generated by a Stark decelerator at forward velocities of 20 m/s up to 50 m/s could be demonstrated and an analytical expression for the focal length in such a microwave lens is presented.

The extension of this technique to three dimensions, i.e., longitudinal guiding, acceleration and deceleration, requires rapidly switched fields and resonator modes with several subsequent electric field maxima on the molecular beam axis that coincides with the resonator axis. This was achieved by employing the $TEM_{0,0,6}$ mode in an open Fabry–Pérot resonator and the $TE_{1,1,12}$ mode in a modified closed cylindrical resonator, analogous to the microwave lenses. Due to the smaller diameter of the closed $TE_{1,1,12}$ microwave decelerator with respect to the Fabry–Pérot resonator the transverse field gradients are larger and consequently the transverse confinement is significantly better and thus well-suited for deceleration experiments.

Additionally, the closed microwave decelerator is cooled with liquid nitrogen which strongly increases the quality factor so that a maximum electric field strength of approximately 1.4 kV/cm is generated at the typical input power of 3 W. With this setup, guiding of packets of ammonia molecules with initial velocities of 25 m/s down to 12 m/s was demonstrated as well as full control over the longitudinal phase space with different switching schemes for spatial and velocity bunching.

In a next step, microwave deceleration and acceleration starting with ammonia molecules with a forward velocity of 20 m/s and 12 m/s was demonstrated using the same microwave decelerator. A maximum acceleration up to 22.7 and 15.7 m/s could be realized, respectively. A maximum deceleration of the initially 20 m/s slow molecular packets down to 17 m/s was obtained and a final velocity of 10 m/s was achieved in the case of the initially 12 m/s slow ammonia molecules. This corresponds to changes in kinetic energy by up to 30% in deceleration and up to 60% in acceleration. Further deceleration was not possible with the present setup. From three-dimensional trajectory simulations using the 4th-order Runge–Kutta numerical integration procedure, it could be demonstrated, that the vanishing number of detected molecules below 10 m/s is a consequence of the significant dilution of the ammonia packet that has to travel almost

10 mm in free-flight from the last microwave deceleration stage to the detection zone.

A next-generation setup is presented that should avoid this issue by moving the detection zone into the microwave resonator. The new design is modular and consists of two subsequent smaller resonators, which allow for stronger electric fields and provides, in total, more electric field maxima in the direction of the molecular beam to effectively decelerate an initially 12 m/s slow beam of ammonia molecules to standstill. Since the electric field maxima of the microwave mode are true three-dimensional traps for molecules in AC-high-field-seeking states, molecules can be efficiently trapped in one of the decelerator stages. A detection zone within the resonator provides the useful feature of detecting the molecules directly in this trap, which allows for a detailed examination of the particle motions.

Resonator-enhanced microwave fields have proven to be a successful tool to manipulate the motion of polar molecules. In contrast to the alternating-gradient technique that was previously applied to manipulate molecules in high-field-seeking states, standing microwaves feature stable three-dimensional electric field maxima in free space. This offers larger phase-space acceptances for motion manipulation experiments. Furthermore, the AC-Stark effect is versatile in the sense that the sign of the AC-Stark shift of a particular quantum state can be shaped by choosing the appropriate sign of the detuning Δ. The extension of this technique to larger and heavier molecules than ammonia is currently under way. A promising design for a microwave lens for aminobenzonitrile has been presented, as well as a simple approach to calculate the zeroth-order AC-Stark shifts for molecules with complex rotational level structures.

During an extended research stay in the group of Prof. John Doyle at Harvard University with Dr. David Patterson, benzonitrile beams from a cryogenic buffer-gas source were investigated. The forward beam velocity distribution was measured using an electrostatic shutter that is in principle a deflector for molecules in high-field-seeking states. The mean value of the velocity distribution could be determined to be on the order of about 80 m/s which is considerably lower than what could be achieved with supersonic jets. The densities of buffer-gas beams are typically very large, so that the phase-space density of a buffer-gas beam of benzonitrile should be on a similar order of magnitude than the phase-space density of the ammonia packets used for the microwave manipulation experiments described in this thesis. Consequently, a buffer-gas beam source would be desirable for future microwave deceleration experiments with medium-sized and larger molecules.

With the method described in this thesis, it should be possible to construct microwave decelerators that provide slow samples of molecules for high-resolutions spectroscopy experiments. This is particularly useful in domains where motion manipulation with static electric fields is not feasible, i.e., for molecules in high-field-seeking states. Possible applications are, for example, experiments in search for the magnitude of the electron's electric dipole moment, or the search for parity-violation effects in small chiral molecules. Another interesting route could become available with the future evolutions of microwave traps that should allow stable trapping of ground-state molecules, an ideal starting point for sympathetic cooling with ultra-cold atoms. Such experiments could provide access to the domain of ultra-cold molecules other than alkali dimers and related species.

Bibliography

[1] Ian W.M. Smith, ed., *Low Temperatures and Cold Molecules* (Imperial College Press, London, 2008) (cit. on p. 1).

[2] Martin T. Bell and Timothy P. Softley, "Ultracold molecules and ultracold chemistry", Molecular Physics **107**, 99–132 (2009) (cit. on pp. 1, 20).

[3] Lincoln D. Carr, David DeMille, Roman V. Krems, and Jun Ye, "Cold and ultracold molecules: science, technology and applications", New Journal of Physics **11**, 055049 (2009) (cit. on pp. 1, 20).

[4] Bretislav Friedrich and John M. Doyle, "Why are Cold Molecules so Hot?", ChemPhysChem **10**, 604–623 (2009) (cit. on p. 1).

[5] Melanie Schnell and Gerard Meijer, "Cold Molecules: Preparation, Applications, and Challenges", Angewandte Chemie International Edition **48**, 6010–6031 (2009) (cit. on pp. 1, 9).

[6] Kang-Kuen Ni, Silke Ospelkaus, David J. Nesbitt, Jun Ye, and Deborah S. Jin, "A dipolar gas of ultracold molecules", Physical Chemistry Chemical Physics **11**, 9626–9639 (2009) (cit. on p. 1).

[7] Goulven Quéméner and Paul S. Julienne, "Ultracold Molecules under Control!", Chemical Reviews **112**, 4949–5011 (2012) (cit. on pp. 1, 6).

[8] Mikhail G. Kozlov and Leonti N. Labzowsky, "Parity violation effects in diatomics", Journal of Physics B: Atomic, Molecular and Optical Physics **28**, 1933 (1995) (cit. on p. 1).

[9] David DeMille, Sidney B. Cahn, Dennis Murphree, David A. Rahmlow, and Mikhail G. Kozlov, "Using Molecules to Measure Nuclear Spin-Dependent Parity Violation", Physical Review Letters **100**, 023003 (2008) (cit. on p. 1).

[10] David DeMille, "Quantum Computation with Trapped Polar Molecules", Physical Review Letters **88**, 067901 (2002) (cit. on p. 1).

[11] Colin M. Western, *PGOPHER, a Program for Simulating Rotational Structure*, Software, `http://pgopher.chm.bris.ac.uk/index.html` (cit. on pp. 4, 106).

[12] Harold J. Metcalf and Peter van der Straten, *Laser Cooling and Trapping* (Springer, Berlin, 2002) (cit. on pp. 4, 50).

[13] Edward S. Shuman, John F. Barry, and David DeMille, "Laser cooling of a diatomic molecule", Nature **467**, 820–823 (2010) (cit. on p. 4).

[14] Valentina Zhelyazkova, Anne Cournol, Thomas E. Wall, Aki Matsushima, Jonathan J. Hudson, Ed A. Hinds, Michael R. Tarbutt, and Ben E. Sauer, "Laser cooling and slowing of CaF molecules", Physical Review A **89**, 053416 (2014) (cit. on p. 4).

[15] Matthew T. Hummon, Mark Yeo, Benjamin K. Stuhl, Alejandra L. Collopy, Yong Xia, and Jun Ye, "2D Magneto-Optical Trapping of Diatomic Molecules", Phys. Rev. Lett. **110**, 143001 (2013) (cit. on p. 4).

[16] William D. Phillips and Harold Metcalf, "Laser deceleration of an atomic beam", Physical Review Letters **48**, 596–599 (1982) (cit. on p. 5).
[17] David J. Wineland, Robert E. Drullinger, and Fred L. Walls, "Radiation-Pressure Cooling of Bound Resonant Absorbers", **40**, 1639–1642 (1978) (cit. on p. 5).
[18] Satyendranath Bose, "Plancks gesetz und lichtquantenhypothese", Zeitschrift für Physik **26**, 178–181 (1924) (cit. on p. 5).
[19] M. H. Anderson, J. R. Ensher, M. R. Matthews, Carl E. Wieman, and Eric A. Cornell, "Observation of Bose–Einstein Condensation in a Dilute Atomic Vapor", Science **269**, 198–201 (1995) (cit. on p. 5).
[20] Eric A. Cornell and Carl E. Wiemann, "Nobel Lecture: Bose–Einstein condensation in a dilute gas, the first 70 years and some recent experiments", Reviews of Modern Physics **74**, 875–893 (2002) (cit. on p. 5).
[21] Wolfgang Ketterle, "Nobel lecture: When atoms behave as waves: Bose–Einstein condensation and the atom laser", Reviews of Modern Physics **74**, 1131–1151 (2002) (cit. on p. 5).
[22] Daniel Kleppner, "Professor Feshbach and his resonance", Physics Today **57**, 12–13 (2004) (cit. on p. 5).
[23] H. R. Thorsheim, J. Weiner, and Paul S. Julienne, "Laser-induced photoassociation of ultracold sodium atoms", Physical Review Letters **58**, 2420–2423 (1987) (cit. on p. 6).
[24] Paul D. Lett, Kristian Helmerson, W. D. Phillips, L. P. Ratliff, Steven L. Rolston, and M. E. Wagshul, "Spectroscopy of Na_2 by photoassociation of laser-cooled Na", Physical Review Letters **71**, 2200–2203 (1993) (cit. on p. 6).
[25] J. D. Miller, R. A. Cline, and D. J. Heinzen, "Photoassociation spectrum of ultracold Rb atoms", Phys. Rev. Lett. **71**, 2204–2207 (1993) (cit. on p. 6).
[26] Cheng Chin, Rudolf Grimm, Paul Julienne, and Eite Tiesinga, "Feshbach resonances in ultracold gases", Reviews of Modern Physics **82**, 1225–1286 (2010) (cit. on p. 6).
[27] Kevin M. Jones, Eite Tiesinga, Paul D. Lett, and Paul S. Julienne, "Ultracold photoassociation spectroscopy: long-range molecules and atomic scattering", Reviews of Modern Physics **78**, 483–535 (2006) (cit. on p. 6).
[28] Thorsten Köhler, Krzysztof Góral, and Paul S. Julienne, "Production of cold molecules via magnetically tunable feshbach resonances", Reviews of Modern Physics **78**, 1311–1361 (2006) (cit. on p. 6).
[29] N. V. Vitanov, T. Halfmann, B. W. Shore, and K. Bergmann, "Laser-induced population transfer by adiabatic passage techniques", Annu. Rev. Phys. Chem. **52**, 763–809 (2001) (cit. on p. 6).
[30] Kang-Kuen. Ni, Silke Ospelkaus, Marcio H. G. de Miranda, Avi Pe'er, Brian Neyenhuis, Joshua J. Zirbel, Svetlana Kotochigova, Paul S. Julienne, Deborah S. Jin, and Jun Ye, "A High Phase-Space-Density Gas of Polar Molecules", Science **322**, 231–235 (2008) (cit. on p. 6).
[31] F. Lang, K. Winkler, C. Strauss, R. Grimm, and Johannes Hecker Denschlag, "Ultracold triplet molecules in the rovibrational ground state", Physical Review Letters **101**, 133005 (2008) (cit. on p. 6).
[32] Johann G. Danzl, Manfred J. Mark, Elmar Haller, Mattias Gustavsson, Russell Hart, Jesus Aldegunde, Jeremy M. Hutson, and Hanns-Christoph Nägerl, "An

ultracold high-density sample of rovibronic ground-state molecules in an optical lattice", Nature Physics **6**, 265–270 (2010) (cit. on p. 6).

[33] Markus Greiner, Cindy A. Regal, and Deborah S. Jin, "Emergence of a molecular Bose–Einstein condensate from a Fermi gas", Nature **426**, 537–540 (2003) (cit. on p. 6).

[34] Selim Jochim, Markus Bartenstein, Alexander Altmeyer, Gerhard Hendl, Stefan Riedl, Cheng Chin, Johannes Hecker Denschlag, and Rudolf Grimm, "Bose–Einstein Condensation of Molecules", Science **302**, 2101–2103 (2003) (cit. on p. 6).

[35] Martin W. Zwierlein, Claudiu A. Stan, Christian H. Schunck, Sebastian M. F. Raupach, Subhadeep Gupta, Zoran Hadzibabic, and Wolfgang Ketterle, "Observation of Bose–Einstein Condensation of Molecules", Physical Review Letters **91**, 250401 (2003) (cit. on p. 6).

[36] Immanuel Bloch, Jean Dalibard, and Wilhelm Zwerger, "Many-body physics with ultracold gases", Reviews of Modern Physics **80**, 885–964 (2008) (cit. on p. 6).

[37] Donald H. Levy, "The Spectroscopy of Very Cold Gases", Science **214**, 263–269 (1981) (cit. on p. 7).

[38] Manish Gupta and Dudley R. Herschbach, "A Mechanical Means to Produce Intense Beams of Slow Molecules", The Journal of Physical Chemistry A **103**, 10670–10673 (1999) (cit. on p. 8).

[39] Manish Gupta and Dudley R. Herschbach, "Slowing and Speeding Molecular Beams by Means of a Rapidly Rotating Source", The Journal of Physical Chemistry A **105**, 1626–1637 (2001) (cit. on p. 8).

[40] Steffen Spieler, Wei Zhong, Pavle Djuricanin, Omid Nourbakhsh, Ilja Gerhardt, Katsunari Enomoto, Frank Stienkemeier, and Takamasa Momose, "Microwave lens effect for the $J = 0$ rotational state of CH_3CN", Molecular Physics **111**, 1823–1834 (2013) (cit. on pp. 8, 17).

[41] Daniel R. Willey, D. N. Bittner, and Frank C. De Lucia, "Collisional cooling of the NO-He - system The pressure broadening cross sections between 4.3 and 1.8 K", Molecular Physics **67**, 455–463 (1989) (cit. on p. 8).

[42] John M. Doyle, Bretislav Friedrich, Jinha Kim, and David Patterson, "Buffer-gas loading of atoms and molecules into a magnetic trap", Physical Review A **52**, R2515–R2518 (1995) (cit. on pp. 8, 100).

[43] Julia Piskorski, David Patterson, Sandra Eibenberger, and John M. Doyle, "Cooling, Spectroscopy and Non-Sticking of trans-Stilbene and Nile Red", ChemPhysChem **15**, 3800–3804 (2014) (cit. on p. 8).

[44] Jonathan D. Weinstein, Robert deCarvalho, Thierry Guillet, Bretislav Friedrich, and John M. Doyle, "Magnetic trapping of calcium monohydride molecules at millikelvin temperatures", Nature **395**, 148–150 (1998) (cit. on p. 9).

[45] Steve E. Maxwell, Nathan Brahms, Robert deCarvalho, David R. Glenn, J. S. Helton, Scott V. Nguyen, David Patterson, Jessie Petricka, David DeMille, and John M. Doyle, "High-Flux Beam Source for Cold, Slow Atoms or Molecules", Physical Review Letters **95**, 173201 (2005) (cit. on p. 9).

[46] Michael Stoll, Joost M. Bakker, Timothy C. Steimle, Gerard Meijer, and Achim Peters, "Cryogenic buffer-gas loading and magnetic trapping of CrH and MnH molecules", Phys. Rev. A **78**, 032707 (2008) (cit. on p. 9).

[47] Wesley C. Campbell, Gerrit C. Groenenboom, Hsin-I Lu, Edem Tsikata, and John M. Doyle, "Time-Domain Measurement of Spontaneous Vibrational Decay of Magnetically Trapped NH", Physical Review Letters **100**, 083003 (2008) (cit. on pp. 9, 13).

[48] David Patterson and John M. Doyle, "Bright, guided molecular beam with hydrodynamic enhancement", The Journal of Chemical Physics **126**, 154307 (2007) (cit. on p. 9).

[49] David Patterson and John M. Doyle, "A Slow, Continuous Beam of Cold Benzonitrile", Physical Chemistry Chemical Physics **17** (2015) 10.1039/C4CP03818E (cit. on pp. 9, 101, 103).

[50] Hsin-I Lu, Julia Rasmussen, Matthew J. Wright, David Patterson, and John M. Doyle, "A cold and slow molecular beam", Physical Chemistry Chemical Physics **13**, 18986–18990 (2011) (cit. on p. 9).

[51] Sebastiaan Y.T. van de Meerakker, Hendrick L. Bethlem, Nicolas Vanhaecke, and Gerard Meijer, "Manipulation and Control of Molecular Beams", Chemical Reviews **112**, 4828–4878 (2012) (cit. on p. 9).

[52] Mikhail Lemeshko, Roman V. Krems, John M. Doyle, and Sabre Kais, "Manipulation of molecules with electromagnetic fields", Molecular Physics **111**, 1648–1682 (2013) (cit. on p. 9).

[53] Hartmut Kallmann and Fritz Reiche, "Über den durchgang bewegter moleküle durch inhomogene kraftfelder", Zeitschrift fúr Physik **6**, 352–375 (1921) (cit. on p. 9).

[54] Walther Gerlach and Otto Stern, "Der experimentelle Nachweis der Richtungsquantelung im Magnetfeld", Zeitschrift für Physik **9**, 349–352 (1922) (cit. on p. 9).

[55] Walther Gerlach and Otto Stern, "Das magnetische moment des silberatoms", Zeitschrift für Physik **9**, 353–355 (1922) (cit. on p. 9).

[56] Pieter Zeeman, "Plancks gesetz und lichtquantenhypothese", Nature **55**, 347–347 (1897) (cit. on p. 9).

[57] Nicolas Vanhaecke, Urban Meier, Markus Andrist, Beat H. Meier, and Frédéric Merkt, "Multistage zeeman deceleration of hydrogen atoms", Physical Review A **75**, 031402 (2007) (cit. on p. 10).

[58] Stephen D. Hogan, Alex W. Wiederkehr, Markus Andrist, Hansjürg Schmutz, and Frédéric Merkt, "Slow beams of atomic hydrogen by multistage Zeeman deceleration", Journal of Physics B: Atomic, Molecular and Optical Physics **41**, 081005 (2008) (cit. on p. 10).

[59] Stephen D. Hogan, Daniel Sprecher, Markus Andrist, Nicolas Vanhaecke, and Frédéric Merkt, "Zeeman deceleration of H and D", Physical Review A **76**, 023412 (2007) (cit. on p. 10).

[60] Edvardas Narevicius, Adam Libson, Christian G. Parthey, Isaac Chavez, Julia Narevicius, Uzi Even, and Mark G. Raizen, "Stopping supersonic oxygen with a series of pulsed electromagnetic coils: a molecular coilgun", Physical Review A **77**, 051401 (2008) (cit. on p. 10).

[61] Alex W. Wiederkehr, Hansjürg Schmutz, Michael Motsch, and Frédéric Merkt, "Velocity-tunable slow beams of cold O2 in a single spin-rovibronic state with full angular-momentum orientation by multistage Zeeman deceleration", Molecular Physics **110**, 1807–1814 (2012) (cit. on p. 10).

[62] Takamasa Momose, Yang Liu, Sida Zhou, Pavle Djuricanin, and David Carty, "Manipulation of translational motion of methyl radicals by pulsed magnetic fields", Physical Chemistry Chemical Physics **15**, 1772–1777 (2013) (cit. on p. 10).

[63] James P. Gordon, Herbert J. Zeiger, and Charles H. Townes, "Molecular Microwave Oscillator and New Hyperfine Structure in the Microwave Spectrum of NH_3", Physical Review **95**, 282–284 (1954) (cit. on p. 11).

[64] James P. Gordon, Herbert J. Zeiger, and Charles H. Townes, "The Maser–New Type of Microwave Amplifier, Frequency Standard, and Spectrometer", Physical Review **99**, 1264–1274 (1955) (cit. on p. 11).

[65] H. G. Bennewitz, W. Paul, and Ch. Schlier, "Fokussierung polarer moleküle", Z. Phys. **141**, 6–15 (1955) (cit. on p. 11).

[66] Daniel Auerbach, Edward E. A. Bromberg, and Lennard Wharton, "Alternate-Gradient Focusing of Molecular Beams", The Journal of Chemical Physics **45**, 2160–2166 (1966) (cit. on p. 12).

[67] Samuel Earnshaw, *On the Nature of the Molecular Forces which Regulate the Constitution of the Luminiferous Ether*, 1842, `http://books.google.de/books?id=yxxYAAAAYAAJ&pg=PA97` (cit. on pp. 12, 48).

[68] Frank Filsinger, Undine Erlekam, Gert von Helden, Jochen Küpper, and Gerard Meijer, "Selector for Structural Isomers of Neutral Molecules", Physical Review Letters **100**, 133003 (2008) (cit. on p. 12).

[69] Stephan Putzke, Frank Filsinger, Henrik Haak, Jochen Küpper, and Gerard Meijer, "Rotational-state-specific guiding of large molecules", Physical Chemistry Chemical Physics **13**, 18962–18970 (2011) (cit. on p. 12).

[70] Stephan Putzke, Frank Filsinger, Jochen Küpper, and Gerard Meijer, "Alternating-gradient focusing of the benzonitrile-argon van der Waals complex", Journal of Chemical Physics **137**, 104310 (2012) (cit. on p. 12).

[71] Hendrick L. Bethlem, Giel Berden, and Gerard Meijer, "Decelerating neutral dipolar molecules", Physical Review Letters **83**, 1558–1561 (1999) (cit. on pp. 12, 57).

[72] Hendrick L. Bethlem, Giel Berden, Floris M. H. Crompvoets, Rienk T. Jongma, André J. A. van Roij, and Gerard Meijer, "Electrostatic trapping of ammonia molecules", Nature **406**, 491–494 (2000) (cit. on pp. 12, 57).

[73] Jacqeline van Veldhoven, Jochen Küpper, Hendrick L. Bethlem, Boris Sartakov, André J.A. van Roij, and Gerard Meijer, "Decelerated molecular beams for high-resolution spectroscopy - The hyperfine structure of (ND3)-N-15", European Physical Journal D **31**, 337–349 (2004) (cit. on pp. 12, 55, 57).

[74] Hendrick L. Bethlem, Floris M.H. Crompvoets, Rienk T. Jongma, Sebastiaan Y.T. van de Meerakker, and Gerard Meijer, "Deceleration and trapping of ammonia using time-varying electric fields", Physical Review A **65**, 053416 (2002) (cit. on pp. 12, 57, 88).

[75] Jason R. Bochinski, Eric R. Hudson, Heather J. Lewandowski, Gerard Meijer, and Jun Ye, "Phase space manipulation of cold free radical OH molecules", Physical Review Letters **91**, 243001 (2003) (cit. on pp. 12, 57).

[76] Jason R. Bochinski, Eric R. Hudson, Heather J. Lewandowski, and Jun Ye, "Cold free-radical molecules in the laboratory frame", Physical Review A **70**, 043410 (2004) (cit. on pp. 12, 57).

[77] Sebastiaan Y.T. van de Meerakker, Paul H.M. Smeets, Nicolas Vanhaecke, Rienk T. Jongma, and Gerard Meijer, "Deceleration and electrostatic trapping of OH radicals", Physical Review Letters **94**, 023004 (2005) (cit. on pp. 12, 57).

[78] Ludwig Scharfenberg, Henrik Haak, Gerard Meijer, and Sebastiaan Y.T. van de Meerakker, "Operation of a Stark decelerator with optimum acceptance", Physical Review A **79**, 023410 (2009) (cit. on pp. 12, 57).

[79] Moritz Kirste, Xingan Wang, Gerard Meijer, Koos B. Gubbels, Ad van der Avoird, Gerrit C. Groenenboom, and Sebastiaan Y.T. van de Meerakker, "Magnetic dipole transitions in the OH $A\,^2\Sigma^+ \leftarrow X\,^2\Pi$ system", Journal of Chemical Physics **137**, 101102 (2012) (cit. on pp. 12, 20, 57).

[80] Sebastiaan Y.T. van de Meerakker, Irena Labazan, Steven Hoekstra, Jochen Küpper, and Gerard Meijer, "Production and deceleration of a pulsed beam of metastable NH ($a^1\Delta$) radicals", Journal of Physics B: Atomic Molecular and Optical Physics **39**, S1077–S1084 (2006) (cit. on pp. 12, 57).

[81] Jens Riedel, Steven Hoekstra, Wolfgang Jäger, Joop J. Gilijamse, Sebastiaan Y.T. van de Meerakker, and Gerard Meijer, "Accumulation of Stark-decelerated NH molecules in a magnetic trap", European Physical Journal D **65**, 161–166 (2011) (cit. on pp. 12, 57).

[82] Steven Hoekstra, Joop J. Gilijamse, Boris Sartakov, Nicolas Vanhaecke, Ludwig Scharfenberg, Sebastiaan Y.T. van de Meerakker, and Gerard Meijer, "Optical pumping of trapped neutral molecules by blackbody radiation", Physical Review Letters **98**, 133001 (2007) (cit. on pp. 12, 16, 57).

[83] Eric R. Hudson, Christopher Ticknor, Brian C. Sawyer, Craig A. Taatjes, Heather J. Lewandowski, Jason R. Bochinski, J. L. Bohn, and Jun Ye, "Production of cold formaldehyde molecules for study and control of chemical reaction dynamics with hydroxyl radicals", Physical Review A **73**, 063404 (2006) (cit. on pp. 12, 57).

[84] Sebastian Jung, Eberhard Tiemann, and Christian Lisdat, "Cold atoms and molecules from fragmentation of decelerated SO_2", Physical Review A **74**, 040701 (2006) (cit. on pp. 12, 57).

[85] Sean K. Tokunaga, Jon M. Dyne, Ed A. Hinds, and Michael R. Tarbutt, "Stark deceleration of lithium hydride molecules", New Journal of Physics **11**, 055038 (2009) (cit. on pp. 12, 57).

[86] Thomas E. Wall, Sean K. Tokunaga, Ed A. Hinds, and Michael R. Tarbutt, "Nonadiabatic transitions in a Stark decelerator", Physical Review A **81**, 033414 (2010) (cit. on pp. 12, 57).

[87] Nick E. Bulleid, Richard J. Hendricks, Ed A. Hinds, Samuel A. Meek, Gerard Meijer, Andreas Osterwalder, and Michael R. Tarbutt, "Traveling-wave deceleration of heavy polar molecules in low-field-seeking states", Physical Review A **86**, 021404 (2012) (cit. on pp. 12, 57).

[88] Joost E. van den Berg, Samuel H. Turkesteen, Eric B. Prinsen, and Steven Hoekstra, "Deceleration and trapping of heavy diatomic molecules using a ring decelerator", European Physical Journal D **66**, 235 (2012) (cit. on pp. 12, 57).

[89] Xingan Wang, Moritz Kirste, Gerard Meijer, and Sebastiaan Y.T. van de Meerakker, "Stark Deceleration of NO Radicals", Zeitschrift für Physikalische Chemie – International Journal of Research in Physical Chemistry & Chemical Physics **227**, 1595–1604 (2013) (cit. on pp. 12, 57).

[90] Hendrick L. Bethlem, André J.A. van Roij, Rienk T. Jongma, and Gerard Meijer, "Alternate gradient focusing and deceleration of a molecular beam", Physical Review Letters **88**, 133003 (2002) (cit. on p. 12).

[91] Michael R. Tarbutt, Hendrick L. Bethlem, Jonathan J. Hudson, V. L. Ryabov, V. A. Ryzhov, Ben E. Sauer, Gerard Meijer, and Ed A. Hinds, "Slowing heavy, ground-state molecules using an alternating gradient decelerator", Physical Review Letters **92**, 173002 (2004) (cit. on p. 12).

[92] Kirstin Wohlfart, Fabian Grätz, Frank Filsinger, Henrik Haak, Gerard Meijer, and Jochen Küpper, "Alternating-gradient focusing and deceleration of large molecules", Physical Review A **77**, 031404 (2008) (cit. on p. 12).

[93] Kirstin Wohlfart, Frank Filsinger, Fabian Grätz, Jochen Küpper, and Gerard Meijer, "Stark deceleration of OH radicals in low-field-seeking and high-field-seeking quantum states", Physical Review A **78**, 033421 (2008) (cit. on pp. 12, 90).

[94] William H. Wing, "Electrostatic Trapping of Neutral Atomic Particles", Physical Review Letters **45**, 631–634 (1980) (cit. on p. 13).

[95] Jacqueline van Veldhoven, Hendrick L. Bethlem, Melanie Schnell, and Gerard Meijer, "Versatile electrostatic trap", Phys. Rev. A **73**, 063408 (2006) (cit. on pp. 13, 16).

[96] David E. Pritchard, "Cooling Neutral Atoms in a Magnetic Trap for Precision Spectroscopy", Physical Review Letters **51**, 1336–1339 (1983) (cit. on p. 13).

[97] Moritz Kirste, Boris Sartakov, Melanie Schnell, and Gerard Meijer, "Nonadiabatic transitions in electrostatically trapped ammonia molecules", Physical Review A **79**, 051401 (2009) (cit. on pp. 13, 47, 48).

[98] Sebastiaan Y. T. van de Meerakker, Nicolas Vanhaecke, Mark P. J. van der Loo, Gerrit C. Groenenboom, and Gerard Meijer, "Direct Measurement of the Radiative Lifetime of Vibrationally Excited OH Radicals", Physical Review Letters **95**, 013003 (2005) (cit. on pp. 13, 16).

[99] Sean K. Tokunaga, Wojciech Skomorowski, Piotr S. Żuchowski, Robert Moszynski, Jeremy M. Hutson, Ed A. Hinds, and Michael R. Tarbutt, "Prospects for sympathetic cooling of molecules in electrostatic, ac and microwave traps", The European Physical Journal D **65**, 141–149 (2011) (cit. on p. 13).

[100] D. J. Larson, James C. Bergquist, John J. Bollinger, Wayne M. Itano, and David J. Wineland, "Sympathetic cooling of trapped ions: A laser-cooled two-species nonneutral ion plasma", Physical Review Letters **57**, 70–73 (1986) (cit. on p. 13).

[101] Michael Drewsen, A. Mortensen, R. Martinussen, Peter F. Staanum, and Jens L. Sørensen, "Nondestructive Identification of Cold and Extremely Localized Single Molecular Ions", Physical Review Letters **93**, 243201 (2004) (cit. on p. 13).

[102] Alexander Ostendorf, Chaobo B. Zhang, M. A. Wilson, David Offenberg, Bernhard Roth, and Stephan Schiller, "Sympathetic Cooling of Complex Molecular Ions to Millikelvin Temperatures", Physical Review Letters **97**, 243005 (2006) (cit. on p. 13).

[103] Martin Zeppenfeld, Michael Motsch, P. W. H. Pinkse, and Gerhard Rempe, "Optoelectrical cooling of polar molecules", Physical Review A **80**, 041401 (2009) (cit. on p. 13).

[104] Martin Zeppenfeld, Barbara G. U. Englert, Rosa Glockner, Alexander Prehn, Manuel Mielenz, Christian Sommer, Laurens D. van Buuren, Michael Motsch, and Gerhard Rempe, "Sisyphus cooling of electrically trapped polyatomic molecules", Nature **491**, 570–573 (2012) (cit. on p. 13).

[105] Jacqueline van Veldhoven, Hendrick L. Bethlem, and Gerard Meijer, "ac Electric Trap for Ground-State Molecules", Physical Review Letters **94**, 083001 (2005) (cit. on pp. 14, 16).

[106] Melanie Schnell, Peter Lützow, Jacqueline van Veldhoven, Hendrick L. Bethlem, Jochen Küpper, Bretislav Friedrich, Monika Schleier-Smith, Henrik Haak, and Gerard Meijer, "A linear AC trap for polar molecules in their ground state", Journal of Physical Chemistry A **111**, 7411–7419 (2007) (cit. on pp. 14, 16).

[107] Peter Lützow, Melanie Schnell, and Gerard Meijer, "Instabilities of molecule motion in a linear ac trap", Physical Review A **77**, 063402 (2008) (cit. on p. 14).

[108] R. Fulton, Alexis I. Bishop, Mikhail N. Shneider, and Peter F. Barker, "Controlling the motion of cold molecules with deep periodic optical potentials", Nature Physics **2**, 465–468 (2006) (cit. on pp. 14, 15).

[109] Henrik Stapelfeldt, Hirofumi Sakai, E. Constant, and Paul B. Corkum, "Deflection of Neutral Molecules using the Nonresonant Dipole Force", Physical Review Letters **79**, 2787–2790 (1997) (cit. on p. 14).

[110] R. Fulton, Alexis I. Bishop, and Peter F. Barker, "Optical stark decelerator for molecules", Phys. Rev. Lett. **93**, 243004 (2004) (cit. on p. 15).

[111] Peter F. Barker and Mikhail N. Shneider, "Slowing molecules by optical microlinear deceleration", Physical Review A **66**, 065402 (2002) (cit. on p. 15).

[112] R. Fulton, Alexis I. Bishop, Mikhail N. Shneider, and Peter F. Barker, "Optical Stark deceleration of nitric oxide and benzene molecules using optical lattices", Journal of Physics B: Atomic Molecular and Optical Physics **39**, S1097–S1109 (2006) (cit. on p. 15).

[113] Samuel A. Meek, Hendrick L. Bethlem, Horst Conrad, and Gerard Meijer, "Trapping molecules on a chip in traveling potential wells", Physical Review Letters **100**, 153003 (2008) (cit. on p. 15).

[114] Samuel A. Meek, Horst Conrad, and Gerard Meijer, "Trapping Molecules on a Chip", Science **324**, 1699–1702 (2009) (cit. on p. 15).

[115] Andreas Osterwalder, Samuel A. Meek, Georg Hammer, Henrik Haak, and Gerard Meijer, "Deceleration of neutral molecules in macroscopic traveling traps", Phys. Rev. A **81**, 051401 (2010) (cit. on p. 15).

[116] Samuel A. Meek, Maxwell F. Parsons, Georg Heyne, Viktor Platschkowski, Henrik Haak, Gerard Meijer, and Andreas Osterwalder, "A traveling wave decelerator for neutral polar molecules", Review of Scientific Instruments **82**, 093108 (2011) (cit. on p. 15).

[117] Azar Trimeche, Manabendra Nath Bera, Jean-Paul Cromières, Jacques Robert, and Nicolas Vanhaecke, "Trapping of a supersonic beam in a traveling magnetic wave", European Physics Journal D **65**, 263–271 (2011) (cit. on p. 15).

[118] Zhong-Kun Hu, Yi Ke, Jin-Bo Zhao, Xiao-Bing Deng, and Jun Luo, "Decelerating polar molecules using traveling microwave lattices", Physical Review A **89**, 053428 (2014) (cit. on pp. 15, 17).

[119] Robert M. Hill and Thomas F. Gallagher, "Deflection of CsF molecules by resonant inhomogeneous electric fields", Phys. Rev. A **12**, 451–459 (1975) (cit. on pp. 15, 16).

[120] Charles C. Agosta, Isaac F. Silvera, Hendricus T. C. Stoof, and Boudewijn J. Verhaar, "Trapping of neutral atoms with resonant microwave radiation", Physical Review Letters **62**, 2361–2364 (1989) (cit. on p. 15).

[121] Robert J.C. Spreeuw, C. Gerz, Lori S. Goldner, W. Phillips, S. Rolston, C. Westbrook, M. W. Reynolds, and Isaac Silvera, "Demonstration of neutral atom trapping with microwaves", Physical Review Letters **72**, 3162–3165 (1994) (cit. on p. 15).

[122] David DeMille, David R. Glenn, and Jessie Petricka, "Microwave traps for cold polar molecules", The European Physical Journal D: Atomic, Molecular, Optical and Plasma Physics **31**, 375–384 (2004) (cit. on pp. 16, 35).

[123] Katsunari Enomoto and Takamasa Momose, "Microwave Stark decelerator for polar molecules", Physical Review A **72**, 061403 (2005) (cit. on pp. 16, 35, 36, 93).

[124] Hitoshi Odashima, Simon Merz, Katsunari Enomoto, Melanie Schnell, and Gerard Meijer, "Microwave Lens for Polar Molecules", Physical Review Letters **104**, 253001 (2010) (cit. on pp. 16, 17, 34).

[125] Simon Merz, Claudia Brieger, Nicolas Vanhaecke, Gerard Meijer, and Melanie Schnell, "Manipulating the motion of polar molecules with microwave radiation", Molecular Physics **111**, 1855–1864 (2013) (cit. on pp. 17, 34).

[126] Simon Merz, Nicolas Vanhaecke, Wolfgang Jäger, Melanie Schnell, and Gerard Meijer, "Decelerating molecules with microwave fields", Physical Review A **85**, 063411 (2012) (cit. on pp. 17, 34, 87).

[127] Katsunari Enomoto, Pavle Djuricanin, Ilja Gerhardt, Omid Nourbakhsh, Yoshiki Moriwaki, Walter Hardy, and Takamasa Momose, "Superconducting microwave cavity towards controlling the motion of polar molecules", Applied Physics B **109**, 149–157 (2012) (cit. on p. 17).

[128] Devin P. Dunseith, Stefan Truppe, Richard J. Hendricks, Ben E. Sauer, Ed A. Hinds, and Michael R. Tarbutt, "A high quality, efficiently coupled microwave cavity for trapping cold molecules", Journal of Physics B: Atomic, Molecular and Optical Physics **48**, 045001 (2015) (cit. on pp. 17, 35).

[129] Jacqueline van Veldhoven, "AC trapping and high-resolution spectroscopy of ammonia molecules", PhD thesis (Radboud Universiteit Nijmegen, Dec. 2006) (cit. on p. 18).

[130] The ACME Collaboration, Jacob Baron, Wes C. Campbell, David DeMille, John M. Doyle, G. Gabrielse, Yulia V. Gurevich, Paul W. Hess, Nick R. Hutzler, Emil Kirilov, Ivan Kozyryev, Brandon R. O'Leary, Cris D. Panda, Maxwell F. Parsons, Elizabeth S. Petrik, Ben Spaun, Amar C. Vutha, and Adam D. West, "Order of Magnitude Smaller Limit on the Electric Dipole Moment of the Electron", Science **343**, 269–272 (2014) (cit. on p. 19).

[131] B. C. Regan, Eugene D. Commins, Christian J. Schmidt, and David DeMille, "New Limit on the Electron Electric Dipole Moment", Physical Review Letters **88**, 071805 (2002) (cit. on p. 19).

[132] Jonathan J. Hudson, Dhiren M. Kara, I. J. Smallman, Ben E. Sauer, Michael R. Tarbutt, and Ed A. Hinds, "Improved measurement of the shape of the electron", Nature **473**, 493–496 (2011-05-26) (cit. on p. 19).

[133] Dhiren M. Kara, I. J. Smallman, Jonathan J. Hudson, Ben E. Sauer, Michael R. Tarbutt, and Ed A. Hinds, "Measurement of the electron's electric dipole moment using YbF molecules: methods and data analysis", New Journal of Physics **14**, 103051 (2012) (cit. on p. 19).

[134] Michael T. Murphy, Victor V. Flambaum, Sébastien Muller, and Christian Henkel, "Strong Limit on a Variable Proton-to-Electron Mass Ratio from Molecules in the Distant Universe", Science **320**, 1611–1613 (2008) (cit. on p. 19).

[135] Julian A. King, John K. Webb, Michael T. Murphy, and Robert F. Carswell, "Stringent Null Constraint on Cosmological Evolution of the Proton-to-Electron Mass Ratio", Physical Review Letters **101**, 251304 (2008) (cit. on p. 19).

[136] Julija Bagdonaite, Paul Jansen, Christian Henkel, Hendrick L. Bethlem, Karl M. Menten, and Wim Ubachs, "A Stringent Limit on a Drifting Proton-to-Electron Mass Ratio from Alcohol in the Early Universe", Science **339**, 46–48 (2013) (cit. on p. 19).

[137] Masatoshi Kajita, "Variance measurement of mp/me using cold molecules", Canadian Journal of Physics **87**, 743–748 (2009) (cit. on p. 20).

[138] Marina Quintero-Pérez, Thomas E. Wall, Steven Hoekstra, and Hendrick L. Bethlem, "Preparation of an ultra-cold sample of ammonia molecules for precision measurements", Journal of Molecular Spectroscopy **300**, 112–115 (2014) (cit. on p. 20).

[139] Mark Brouard, David H. Parker, and Sebastiaan Y. T. van de Meerakker, "Taming molecular collisions using electric and magnetic fields", Chemical Society Reviews **43**, 7279–7294 (2014) (cit. on p. 20).

[140] David W. Chandler and Paul L. Houston, "Two-dimensional imaging of state-selected photodissociation products detected by multiphoton ionization", The Journal of Chemical Physics **87**, 1445–1447 (1987) (cit. on p. 20).

[141] André T. J. B. Eppink and David H. Parker, "Velocity map imaging of ions and electrons using electrostatic lenses: application in photoelectron and photofragment ion imaging of molecular oxygen", Review of Scientific Instruments **68**, 3477–3484 (1997) (cit. on p. 20).

[142] Matthew T. Hummon, Timur V. Tscherbul, Jacek Kłos, Hsin-I Lu, Edem Tsikata, Wesley C. Campbell, Alexander Dalgarno, and John M. Doyle, "Cold **N**+NH Collisions in a Magnetic Trap", Physical Review Letters **106**, 053201 (2011) (cit. on p. 20).

[143] Brian C. Sawyer, Benjamin K. Stuhl, Mark Yeo, Timur V. Tscherbul, Matthew T. Hummon, Yong Xia, Jacek Kłos, David Patterson, John M. Doyle, and Jun Ye, "Cold heteromolecular dipolar collisions", Physical Chemistry Chemical Physics **13**, 19059–19066 (2011) (cit. on p. 20).

[144] Yuan-Pin Chang, Karol Dlugolecki, Jochen Küpper, Daniel Rösch, Dieter Wild, and Stefan Willitsch, "Specific Chemical Reactivities of Spatially Separated 3-Aminophenol Conformers with Cold Ca^+ Ions", Science **342**, 98–101 (2013) (cit. on p. 20).

[145] Alon B. Henson, Sasha Gersten, Yuval Shagam, Julia Narevicius, and Edvardas Narevicius, "Observation of Resonances in Penning Ionization Reactions at Sub-Kelvin Temperatures in Merged Beams", Science **338**, 234–238 (2012) (cit. on p. 20).

[146] Simon Chefdeville, Yulia Kalugina, Sebastiaan Y. T. van de Meerakker, Christian Naulin, François Lique, and Michel Costes, "Observation of partial wave resonances in low-energy o2–h2 inelastic collisions", Science **341**, 1094–1096 (2013) (cit. on p. 20).

[147] Benjamin Bertsche, Justin Jankunas, and Andreas Osterwalder, "Low-temperature collisions between neutral molecules in merged molecular beams", CHIMIA International Journal for Chemistry **68**, 256–259 (2014-04-30) (cit. on p. 20).

[148] Joop J. Gilijamse, Steven Hoekstra, Sebastiaan Y. T. van de Meerakker, Gerrit C. Groenenboom, and Gerard Meijer, "Near-Threshold Inelastic Collisions Using Molecular Beams with a Tunable Velocity", Science **313**, 1617–1620 (2006) (cit. on p. 20).

[149] L. Paul Parazzoli, Noah J. Fitch, Piotr S. Żuchowski, Jeremy M. Hutson, and Heather J. Lewandowski, "Large Effects of Electric Fields on Atom-Molecule Collisions at Millikelvin Temperatures", Phys. Rev. Lett. **106**, 193201 (2011) (cit. on p. 20).

[150] John David Jackson, *Classical Electrodynamics*, 3rd ed. (John Wiley & Sons, New York, 1962) (cit. on p. 23).

[151] Walter Greiner, *Classical Electrodynamics* (Springer, New York, 1998) (cit. on p. 23).

[152] David M. Pozar, *Microwave Engineering*, 4th ed. (John Wiley & Sons, New York, 1998) (cit. on p. 23).

[153] Hugh Russell Latham Lamont, *Wave Guides*, 3rd ed. (John Wiley & Sons, New York, 1946) (cit. on p. 27).

[154] Gary D. Boyd and Herwig Kogelnik, "Generalized confocal resonator theory", Bell Systems Technical Journal **41**, 1347 (1962) (cit. on p. 35).

[155] Herwig Kogelnik and Tingye Li, "Laser beams and resonators", Proceedings of the IEEE **54**, 1312–1329 (1966) (cit. on p. 35).

[156] Jens-Uwe Grabow, Wolfgang Stahl, and Helmut Dreizler, "A multioctave coaxially oriented beam-resonator arrangement Fourier-transform microwave spectrometer", Review of Scientific Instruments **67**, 4072–4084 (1996) (cit. on p. 35).

[157] Jens-Uwe Grabow, E. Samuel Palmer, Michael C. McCarthy, and Patrick Thaddeus, "Supersonic-jet cryogenic-resonator coaxially oriented beam-resonator arrangement fourier transform microwave spectrometer", Review of Scientific Instruments **76**, 093106 (2005) (cit. on pp. 35, 36).

[158] Omair Ghafur, Arnaud Rouzee, Arjan Gijsbertsen, Wing Kiu Siu, Steven Stolte, and Marc J. J. Vrakking, "Impulsive orientation and alignment of quantum-state-selected NO molecules", Nature Physics **5**, 289–293 (2009) (cit. on p. 37).

[159] Richard A. Matula, "Electrical resistivity of copper, gold, palladium, and silver", Journal of Physical and Chemical Reference Data **8**, 1147–1298 (1979) (cit. on p. 39).

[160] J. E. Jensen, W. A. Tuttle, R. B. Stewart, H. Brechna, and A. G. Prodell, *Selected Cryogenic Data Notebook*, 1980, `http://www.bnl.gov/magnets/Staff/Gupta/cryogenic-data-handbook/` (visited on 05/21/2014) (cit. on p. 40).

[161] Vladimir Gubarev and Sibel Yasar, *XFEL Cavity Database*, `http://xfel.desy.de/cavity_database/` (visited on 12/01/2014) (cit. on p. 41).

[162] Walter Gordy and Robert Lee Cook, *Microwave Molecular Spectra*, 3rd ed. (John Wiley & Sons, New York, 1984) (cit. on pp. 44, 100, 106).

[163] Charles H. Townes and Arthur L. Schawlow, *Microwave Spectroscopy* (Dover Publications, New York, 1975) (cit. on pp. 46, 106).

[164] Gerhard Herzberg, *Electronic Spectra and Electronic Structure of Polyatomic Molecules* (D. van Nosterand, New York, 1966) (cit. on p. 46).

[165] Suketu R. Gandhi and Richard B. Bernstein, "Focusing and state selection of NH_3 and OCS by the electrostatic hexapole via 1st-order and 2nd-order stark effects", Journal of Chemical Physics **87**, 6457–6467 (1987) (cit. on p. 46).

[166] Stephen Kukolich, "Measurement of Ammonia Hyperfine Structure with a Two-Cavity Maser", Physical Review **156**, 83–92 (1967) (cit. on p. 48).

[167] Jacqueline van Veldhoven, Rienk Jongma, Boris Sartakov, Waldo Bongers, and Gerard Meijer, "Hyperfine structure of ND_3", Physical Review A **66**, 032501 (2002) (cit. on p. 48).

[168] Boris Sartakov, Private communication (cit. on pp. 49, 50).

[169] Stanley H. Autler and Charles H. Townes, "Stark Effect in Rapidly Varying Fields", Physical Review **100**, 703–722 (1955) (cit. on p. 50).

[170] Claude Cohen-Tannoudji, Bernard Diu, and Frank Laloe, *Quantum Mechanics*, Vol. 2 (Wiley-VCH, 1977) (cit. on p. 50).

[171] Edwin T. Jaynes and Fred W. Cummings, "Comparison of quantum and semi-classical radiation theories with application to the beam maser", Proceedings of the IEEE **51**, 89–109 (1963) (cit. on p. 50).

[172] Claude Cohen-Tannoudji, Jacques Dupont-Roc, and Gilbert Grynberg, *Atom-Photon Interactions* (Wiley-VCH, 2004) (cit. on p. 50).

[173] W. C. Wiley and I. H. McLaren, "Time-of-Flight Mass Spectrometer with Improved Resolution", Review of Scientific Instruments **26**, 1150–1157 (1955) (cit. on pp. 56, 69).

[174] Sebastiaan Y.T. van de Meerakker, Nicolas Vanhaecke, and Gerard Meijer, "Stark deceleration and trapping of OH radicals", Annual Review of Physical Chemistry, Annual Review of Physical Chemistry **57**, 159–190 (2006) (cit. on p. 57).

[175] Hendrick L. Bethlem, "Deceleration and Trapping of Polar Molecules usgin Time-varying Electric Fields", PhD thesis (Radboud Universiteit Nijmegen, Sept. 2002) (cit. on p. 60).

[176] Mike N. R. Ashfold, Richard N. Dixon, N. Little, R. J. Stickland, and Colin M. Western, "The $\tilde{B}^1E'$ state of ammonia: Sub-Doppler spectroscopy at vacuum ultraviolet energies", The Journal of Chemical Physics **89**, 1754–1761 (1988) (cit. on p. 68).

[177] Floris M.H. Crompvoets, Rienk T. Jongma, Hendrick L. Bethlem, André J.A. van Roij, and Gerard Meijer, "Longitudinal focusing and cooling of a molecular beam", Physical Review Letters **89**, 093004 (2002) (cit. on p. 86).

[178] Kirstin Wohlfart, "Alternating-gradient focusing and deceleration of large molecules", PhD thesis (Freie Universität Berlin, May 2008) (cit. on p. 90).

[179] David R. Borst, Timothy M. Korter, and David W. Pratt, "On the additivity of bond dipole moments. stark effect studies of the rotationally resolved electronic spectra of aniline, benzonitrile, and aminobenzonitrile", Chem. Phys. Lett. **350**, 485–490 (2001) (cit. on p. 99).

[180] David Patterson and John M. Doyle, "Cooling molecules in a cell for FTMW spectroscopy", Molecular Physics **110**, 1757–1766 (2012) (cit. on p. 101).

[181] Laurens D. van Buuren, Christian Sommer, Michael Motsch, Sebastian Pohle, Markus Schenk, Josef Bayerl, Pepijn W. H. Pinkse, and Gerhard Rempe, "Electrostatic Extraction of Cold Molecules from a Cryogenic Reservoir", Physical Review Letters **102**, 033001 (2009) (cit. on p. 101).

[182] H. M. Pickett, *SPFIT/SPCAT*, Software, 1991, `http://spec.jpl.nasa.gov/` (cit. on p. 106).

Publikationsliste

Hitoshi Odashima, Simon Merz, Katsunari Enomoto, Melanie Schnell, and Gerard Meijer, "Microwave Lens for Polar Molecules", Physical Review Letters **104**, 253001 (2010).

Simon Merz, Nicolas Vanhaecke, Wolfgang Jäger, Melanie Schnell, and Gerard Meijer, "Decelerating molecules with microwave fields", Physical Review A **85**, 063411 (2012).

Simon Merz, Claudia Brieger, Nicolas Vanhaecke, Gerard Meijer, and Melanie Schnell, "Manipulating the motion of polar molecules with microwave radiation", Molecular Physics **111**, 1855-1864 (2013).

Lebenslauf

Der Lebenslauf ist in der Online-Version aus Gründen des Datenschutzes nicht enthalten.

Selbstständigkeitserklärung

gemäß §7, Ziffer (4)
der Promotionsordnung vom 05.02.2010 des Fachbereichs Physik
an der Freien Universität Berlin

Die Dissertation habe ich selbstständig angefertigt. Alle Hilfsmittel und Hilfen habe ich angegeben, insbesondere habe ich wörtlich oder dem Sinne nach anderen Veröffentlichungen entnommene Stellen kenntlich gemacht.

Die Dissertation habe ich bisher weder in der gegenwärtigen noch in einer anderen Fassung weder dem Fachbereich Physik der Freien Universität noch einer anderen Fakultät oder Universität vorgelegt.

Berlin, den 20.03.2015 _____
(Simon Merz)

Danksagung

The last almost 5 years have been an extraordinary and eventful time. I started with a freshly moved experiment, away from the main Hall at the Fritz Haber Institute into its own Laboratory just across the floor. Little did I know that I would move it again, this time a few 100 kilometers further away to the Center for Free-Electron Laser Science on the DESY site in Hamburg and another few months later to its final destination in the beautiful University Hamburg Building 67. With this, I want to emphasize how many different places the molecular beam machine has seen and so did I. Naturally, this means that I had the pleasure of working for, with and alongside a large number of people that have a considerable share in making this research possible. I want to thank you all for your support, encouragement and all the memorable moments that put the extra fun into science.

Zuallererst möchte ich meiner Langzeitbetreuerin Melanie Schnell danken, der ich einen großen Teil meiner wissenschaftlichen Fertigkeiten zu verdanken habe. Melanie, vielen Dank für zahllose Ratschläge von nah und fern, das unermüdliche Aufpolieren meines chaotischen Schreibstils und auch für das Ermöglichen des Harvard-Aufenthalts. Außerdem vielen Dank für das gründliche Korrekturlesen dieser Arbeit.

Besonderer Dank gilt Prof. Gerard Meijer für den anhaltenden Enthusiasmus für Mikrowellenabbremser und die einzigartige Atmosphäre, die ich am Fritz-Haber-Institut erleben durfte. Vielen Dank auch für das Ermöglichen des sanften Übergangs nach Hamburg und für die vielen hilfreichen Kommentare zu dieser Arbeit.

Ein großes Dankeschön auch an Nicolas Vanhaecke für die gute Betreuung in Berlin, die auch nach meinem Umzug kein Ende gefunden hat. Unvergessen sind die Treffen um 2 Uhr morgens, um noch letzte Rechnungen für eine Veröffentlichung zu Ende zu bringen, oder für einen Ratschlag zur Fehlerbehebung am Experiment.

Thanks also to David Patterson whom I had the pleasure of working with at Harvard University. He introduced me to so many interesting research projects, from buffer-gas cells via NV centers to microwave spectroscopy and also to the very important culinary delights of Café Rustica and BBQ.

Thanks to Jack Graneek, my post-decessor, who contributed substantially to the designs and ideas to extend microwave manipulation to larger molecules and helped a lot during the re-commissioning phase after the move to Hamburg.

Vielen Dank an Claudia Brieger, die mich am Fritz-Haber-Institut bei den Experimenten mit der zweiten Mikrowellenlinse hilfreich unterstützt hat und an Wolfgang Jäger für die Unterstützung bei den ersten Kühlversuchen am Mikrowellenabbremser und selbstverständlich auch für das Instandhalten des wichtigsten Ausrüstungsgegenstandes der MP-Abteilung.

Ein weiteres großes Dankeschön an Inga von Dölln für die Organisation der kleinen und

großen Dinge hinter den Kulissen und ganz besonders für die unvergessenen Weihnachtsfeiern und die legendären Wandertage.

Unersetzlich für die Experimente, die in dieser Arbeit beschrieben sind waren auch Henrik Haak, der mit zahlreichen Konstruktionskniffen den Aufbau der Experimente beschleunigt oder vereinfacht hat, Sandy Gewinner, der eine große Hilfe bei der Farbstofflaserjustierung war, Petrik Bischoff, der kurzfristig präzise Kleinteile beigesteuert hat, Georg Hammer, der immer mit Rat und Tat zur Seite stand, wenn wieder ein exotischer Gasflaschenadapter benötigt wurde und Heinz Junkes und Uwe Hoppe, die KouDA gezähmt haben und maßgeblich bei der Migration des Messrechnersystems ins DESY-Netzwerk geholfen haben. Vielen Dank dafür.

An dieser Stelle möchte ich mich auch bei der Feinwerktechnik und dem Elektroniklabor des Fritz-Haber-Instituts und der Werkstatt der Universität Hamburg bedanken, die die Mikrowellenresonatoren und zahlreiche Zubehörteile von der Antenne bis hin zur Stromversorgungseinheit gefertigt haben.

Vielen Dank allen meinen Büronachbarn: David Schmitz, Isabelle Gonzàles Flòrez, Janneke Blokland, Marko Härtelt, Sabrina Zinn und Stephan Warnke fürs Mitfiebern in guten Zeiten und die notwendige Ablenkung in Zeiten in denen alles schief ging. Außerdem Danke für kiloweise Schokolade, die Weihnachtsmarkttasse, Deutsch–Niederländische Übersetzungen der Korrespondenz mit holländischen Segelmachern und vieles mehr.

Humongous thanks to the CoCoMol crowd, Alvin Shubert, Amanda Steber, Anna Krin, Christobal Perez and Sérgio Domingos, for everything from coffee breaks to lending a hand in the lab or supplying microwave spectroscopy figures.

Furthermore, I want to thank everybody from the Molecular Physics department, where unlimited amounts of nitrogen just flow from a socket in the wall and a large bottle of xenon waits in the gas cabinet, for the truly great time I had, for the regular "coffee, cake and sometimes even ice cream"-afternoon breaks and the Sommerfests.

Thanks to Prof. John Doyle for making my excursion across the Atlantic Ocean possible and to the entire John Doyle group, in particular to Nick Hutzler for the great hospitality.

For all the valuable discussions about experimental and physical issues I want to thank Thomas Betz, Christian Schewe, David Schmitz, Stephan Putzke, Marko Härtelt, Peter Zieger and Chris Medcraft.

Distraction is highly welcomed during long office and lab hours, for this I want to thank the Fritz' Kicker Group, everyone who joins for the Friday afternoon MPSD break, Timur Rvachov for the AR-15, Glock and ice hockey lessons, thanks to the molecular party department: Nadja Heine, Christan Kerpal and Mathias Fagiani, to Alex Woodham for burpees, push-ups and awesome wine tastings, to Misha Lemeshko, the model example that no matter where you are in the world, you will meet someone from the Fritz.

Vielen Dank auch an Malte und Thilo für die Segelwochenenden auf dem Wasser, die einen großen Teil zur geistigen Gesundheit beitragen, auch wenn fast immer *nur* ein 2. Platz dabei herauskommt.

Abschließend möchte ich noch Tine danken, die es mir in der Schreibzeit ermöglicht hat, die weltlichen Dinge in den Hintergrund schieben zu können. Schön, dass Du da bist.